



Université
de Toulouse

THÈSE

En vue de l'obtention du

DOCTORAT DE L'UNIVERSITÉ DE TOULOUSE

Délivré par : *l'Institut National Polytechnique de Toulouse (INP Toulouse)*

Présentée et soutenue le JJ/MM/2018 par :

NICOLA LUMINARI

Le titre de la thèse

JURY

PREMIER MEMBRE

Professeur d'Université

Président du Jury

SECOND MEMBRE

Astronome Adjoint

Membre du Jury

TROISIÈME MEMBRE

Chargé de Recherche

Membre du Jury

École doctorale et spécialité :

MEGEP : Dynamique des fluides

Unité de Recherche :

Institut de Mécanique des Fluides de Toulouse (I.M.F.T.)

Directeur(s) de Thèse :

M. Alessandro BOTTARO et M. Christophe AIRIAU

Rapporteurs :

Premier RAPPORTEUR et Second RAPPORTEUR

Contents

1 Poroelastic natural coatings	9
1.1 Biomimetics of poroelastic coatings	9
1.1.1 Riblets and shark-skin surfaces	12
1.1.2 Permeable surfaces	17
1.1.3 Bluff bodies	17
1.1.4 Canopy flow	21
1.2 Models for flows through porous surfaces	24
1.2.1 Isotropic drag models	26
1.2.2 Homogenization models	27
1.3 Stability of flows over permeable surfaces	30
1.3.1 Stability theory generalities	31
2 Volume Average Method	34
2.1 Introduction	34
2.2 Derivation of VANS equations for 3D incompressible fluids	34
2.2.1 Definition of the averaging filter	34
2.2.2 Theorems involving derivatives of spatial averaging	35
2.2.3 Averaged continuity equations	36
2.2.4 Averaged momentum equations	37
2.2.5 Length scale decomposition	38
2.3 Closure problems	40
2.4 Interface condition	40
3 Drag-model sensitivity of Kelvin-Helmholtz waves in canopy flows	41
3.1 Introduction	41
3.2 Model of the canopy flow	43
3.2.1 The mean flow	43
3.2.2 Stability and sensitivity equations	46
3.3 SENSITIVITY RESULTS FOR THE ISOTROPIC DRAG MODEL	48

3.4	AN ALTERNATIVE SENSITIVITY MODEL: ACCOUNTING FOR THE CANOPY ANISOTROPICITY	51
3.4.1	The sensitivity equations	52
3.5	CONCLUDING REMARKS	54
4	Effect of geometrical parameters and inertia on the apparent permeability tensor in fibrous porous media	61
4.1	Introduction	61
4.2	The Volume-Averaged Navier-Stokes (VANS) method	64
4.3	Validation and setup	64
4.3.1	Computational domain	64
4.3.2	Numerical setup	65
4.3.3	Mesh convergence analysis	65
4.3.4	Validation on two different configurations	67
4.3.5	Tests with larger REV's	67
4.4	Microscopic solutions	69
4.5	The apparent permeability tensor	76
4.6	A metamodel for \mathbf{H}	80
4.6.1	DACE sampling	81
4.6.2	Kriging interpolation method	84
4.7	Concluding remarks	87

List of Figures

1.1	Microscope enlarged picture of the shark skin.	10
1.2	Feathers on owl's wing. Left: trailing edge. Right: leading edge. The differences in shape and mechanical properties, as rigidity, between the leading and trailing edge, is a consequence of the different flow regimes in the wing.	10
1.3	Particular of a Peacock butterfly wing, taken with a Scanning Electron Microscope. Images from wikimedia.org	11
1.4	(a) Scanning electron microscopy (SEM) image showing the structure of lotus leaf, (b) higher order of magnification on the single protuberance forming the surface and (c) a water drop with high contact angle, attaining an almost spherical shape. Images from Stratatakis et al. [115].	12
1.5	Schematics of the <i>protrusion height</i> concept. The mean velocity profiles for the stream-wise and cross-flow velocities are shown. In presence of a ridge it is possible to extrapolate the point of zero velocity from the velocity gradient outside the riblet; finding respectively, the <i>stream-wise protrusion height</i> h_{ps} and the <i>cross-flow protrusion height</i> h_{pc} . Image from Bechert et al. [15].	13
1.6	Example of drag reduction relation to the ridge spacing. The maximum performance is normally around $s^+ = 15$, the picture shows also that when the riblet are really tight one another the laminar case is retrieved. On the contrary when the riblets are far away one another their performance is comparable to rough plate case. Image from Jimenez et al. [71].	14
1.7	Two different sizes of riblets are shown when interacting with a sublayer vortex. In gray it is represented the area where friction is important. Clearly when both sizes are comparable the surface experience a larger friction and the performance is lowered. Image from Choi et al. [34].	15
1.8	Performance comparison between a riblet surface against a seal fur. The drag reduction has been computed as: $DR\% = \frac{\Delta\tau}{\tau_0}\%$ Image from Itoh et al. [69].	17

1.9	Diagram showing an example of angular pressure distribution around a cylinder for viscous flow. The black line is the case of a solid body, the green one is the modified pressure in presence of a porous layer at the rear part. Image from Klausmann and Ruck [73].	18
1.10	Square cylinder vorticity contour for $Re = 30000$. Top: solid case. Bottom: porous case with layer extension $h = 10\%D$	19
1.11	Figure a and b show respectively the schematics of the mean flow over a rough wall and a canopy flow; the difference in the eddy size is clear, also the inflection point in the canopy flow velocity profile is transparent. The figure c and d instead show the turbulent spectra for the two different flows above, in case of rough wall a Kolmogorov type of spectra can be retrieved; in case of canopy flow it is possible to see a larger peak in the frequency of the mixing layer instability, a steeper slope in the energy cascade part and high frequency peaks at high frequencies. Image from De Langre [38]	22
1.12	The effects of the Cauchy number C_Y on the drag reduction are presented in the figure. The drag reduction has been represented as the ratio between the frontal area A and the drag coefficient C_D at static condition (subscript 0) and the dynamic condition (no subscript). Image from De Langre [38]	23
1.13	Sketch of a fully developed flow over a poroelastic surface made of multiple filaments.	24
1.14	Schematics of a porous medium system of size L , with a zoom on the microscopic structure and its scale ℓ . Image from Whitaker [124].	28
1.15	Left: when the drag of the canopy is high enough it generates canopy-scale vortices by Kelvin-Helmholtz instability. These vortices may interact with the flexible vegetation and generate a waving motion called monami. Right: when this interaction is too weak, the canopy bend only. Image from Nepf [94].	30
1.16	Classification of modal linear stability theories. Table reported from Juniper et al. [72].	32
1.17	Left: first emergence of the Kelvin-Helmholtz instability. The growth-rate is proportional to the shear magnitude at the inflection point. Center: the instability evolves in rollers consisting of high vorticity that are spaced with a similar wave-length Λ_x as the previous stage. Right: secondary instabilities in the rollers lead to their kinking and pairing, coherent structures show up in the transverse and stream-wise dimensions. Image from Finnigan [46].	33
2.1	Illustration of the REV concept.	35
3.1	Configuration studied with main notations	44

3.2	Left frame: mean flow U , together with experimental data points [51], its first derivative, and drag coefficient distribution (case G). Center: viscous and inviscid growth rates, ω_i , as a function of the streamwise wavenumber α . Right: corresponding frequencies, ω_r	45
3.3	Moduli of direct (left frame) and adjoint (right frame) eigenfunctions for the viscous (continuous lines, $Re = 3450$) and the inviscid (symbols) case, in correspondence to the wavenumber of largest amplification.	47
3.4	Real and imaginary parts of the sensitivities to mean flow variations (top) and to variations in the drag distribution function (bottom), for the parameters of 3.3	49
3.5	Infinite norms of the sensitivity functions for varying α	50
3.6	Amplification factor (left) and frequency of the most unstable mode as a function of α , for the anisotropic drag model	52
3.7	Left and center frames: moduli of direct and adjoint eigenfunctions; pressure and “adjoint pressure” are drawn with dashed lines. Right: real and imaginary parts of the sensitivity function G_U ($\alpha = 0.4790$)	53
3.8	Case G. Left: infinite norm of G_U for varying α . Center and right frames: real and imaginary parts of the sensitivity coefficients to variations in the permeability components	54
3.9	Case G. Left: mean velocity profile, U , versus the drag coefficient, C_d . Right: first derivative, dU/dC_d . The triangles denote the region $y \in [0.76, 1]$, the filled circles denote the region $y \in [0.3, 0.76]$	56
4.1	REV for the fiber geometry investigated.	64
4.2	Mesh used for the computation; top view (left) and zoom in the boundary layer region (right). $\varepsilon = 0.6$	66
4.3	Permeability versus porosity for a square arrangement of cylinders. The scaling of the permeability is ℓ^2 and is explicitly indicated in the vertical axis.	68
4.4	Permeability versus porosity for a staggered arrangement of cylinders. The permeability component is here scaled with d^2 (and not ℓ^2), with d the diameter of the inclusions.	69
4.5	Relative error between the microscopically computed forces along the x_1 direction and those arising from the Darcy-Forcheimber model; $\varepsilon = 0.8$ for the REV in the staggered arrangement of Yazdchi et al. [125].	70
4.6	REV configurations. Left: $2 \times 2 \times 1$ arrangement; centre: $1 \times 1 \times 1$ arrangement (reference); right $1 \times 1 \times 3$ arrangement.	70

4.7	Top row: plane view of the dimensionless x_1 component of the local velocity field \mathbf{v}_β for the case $\theta = 0, \phi = 0, \varepsilon = 0.6$ and for three Reynolds numbers $Re_d = 0, 10, 50$, from left to right. Mid row: microscopic M_{11} fields corresponding to the images in the top row. Bottom row: M_{11} fields for the same Euler angles and Reynolds number as in the top two rows, and smaller porosity ($\varepsilon = 0.4$).	72
4.8	right: Non-dimensional M_{21} field for $\theta = 0, \phi = 0, Re_d = 10, \varepsilon = 0.8$, left: Non-dimensional M_{12} field for $\theta = 22.5^\circ, \phi = 45^\circ, Re_d = 50, \varepsilon = 0.4$	73
4.9	Non-dimensional \mathbf{M} components fields for the case $\theta = 22.5^\circ, \phi = 45^\circ, Re_d = 50, \varepsilon = 0.6$	75
4.10	Diagonal elements of the apparent permeability \mathbf{H} as function of the Reynolds number for porosity $\varepsilon = 0.8$. The forcing direction is represented through the couple of Euler angles (θ, ϕ) (cf. table 4.2 for the case index). Left column: low- Re_d regime; right column: inertial regime.	77
4.11	Same as figure 4.10 with porosity $\varepsilon = 0.6$	78
4.12	Same as figure 4.10 with porosity $\varepsilon = 0.4$	79
4.13	Scatter matrix plot for the collected numerical data of the apparent permeability tensor.	82
4.14	Explanatory sketch for the relation between mean pressure gradient and mean velocity field.	83
4.15	Response surfaces of H_{11} with $\phi = 0^\circ$ for porosity $\varepsilon = 0.4, 0.6, 0.8$, from left to right.	86
4.16	Response surfaces of H_{11} with $\theta = 0^\circ$ for porosity $\varepsilon = 0.4, 0.6, 0.8$, from left to right.	87
4.17	Response surfaces of H_{11} with $Re = 40$ for porosity $\varepsilon = 0.4, 0.6, 0.8$, from left to right.	88
4.18	Response surface of H_{11} ; in the left frame $\phi = \theta = 0$, in the centre frame $\phi = 90^\circ, \theta = 0$ and on the right $\phi = 45^\circ, \theta = 22.5^\circ$	89

List of Tables

3.1	Temporal versus spatial stability, Case G. The model employed here is based on a modified Orr-Sommerfeld equation—rather than a system based on primitive variables as done in the bulk of the paper—which is why the temporal results have slightly larger growth rates ω_i than those displayed in Fig. 3.2; this is related to the need of computing numerically d^2U/dy^2 and dC_d/dy in the Orr-Sommerfeld-like equation. In italics, the growth rates obtained from Gaster’s transformation are reported; the parameters imposed in each simulation are indicated with bold characters. The solutions for $Re = 10^9$ coincide with those found using the inviscid equations.	58
4.1	Convergence analysis. Left: average velocity within the REV, normalized with $\frac{K_{11}}{\nu_\beta} \ \mathbf{f}\ $. Right: grid convergence metrics. The REV has $\varepsilon = 0.6$, the motion is along x_1 , i.e. $\theta = \phi = 0$ and $Re_d \rightarrow 0$	67
4.2	Directions of the forcing tested and property of the solutions.	76
4.3	Sampling parameters.	81
4.4	Permeability components ratio for three values of the porosity. The permeability ratios here are given by the angular coefficients of the linear correlations displayed in figure 4.13.	84

Chapter 1

Poroelastic natural coatings

Nature is the source of all true knowledge. She has her own logic, her own laws, she has no effect without cause nor invention without necessity

- , Leonardo Da Vinci

1.1 Biomimetics of poroelastic coatings

Usually when someone is asked to imagine some "rapid" object as an airplane, a boat or a car, the common sense leads us to think about it as the smoothest as possible. However if we look around, nature seems not to agree with the previous statement. In fact most of the surfaces in Nature are not at all smooth, they almost always present some kind more or less regular arrangement of discontinuities at various length scales. Since Nature have had a very large time-span to optimize this kind of surfaces we can be very certain that they are the best possible option. One should pinpoint that the non smoothness of these surfaces can be connected to some other biological functions rather than pure fluid dynamic performance, and of course it can be the case.

With that in mind we want to show the reader some of the most notable examples of "natural" aerodynamic surfaces.

Probably the most notable example is the shark skin, in figure 1.1 a segment of the skin is depicted, as if appears to be, under the microscope.

The enlargement show that the surface is made up by a series of overlapped denticles, and experiment shows that they can move and interact with the flow.

The shark "technology" has somehow been applied by Speedo®; they have fabricated their famous swimming suits with a surface that mimic the roughness of sharks; and they happen to break multiples world records. This controversial swimmers performance was due to the fact that they compress the body giving the swimmer a more and streamlined shape. Even though the company has been publicized their product as it was a synthetic shark skin, Oeffner and Lauder [96] have shown that the texture of their swimming suits

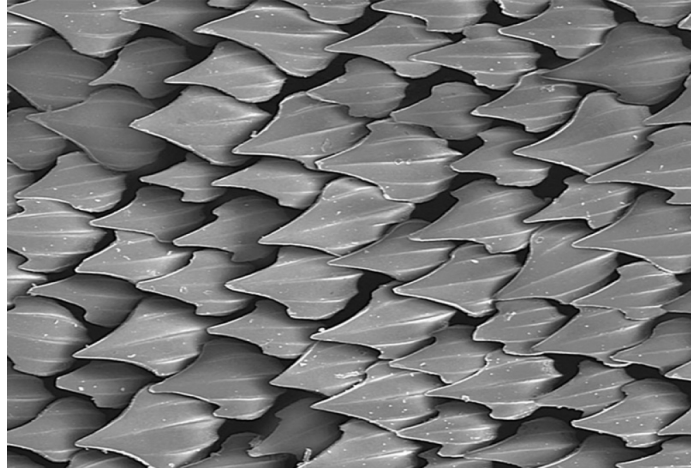


Figure 1.1: Microscope enlarged picture of the shark skin.

is somehow different from the shark dermal structure. In their work the authors have performed swimming experiment with a flat plate with different coatings and they did not find significant speed enhancement with a swimsuit like surface, but the measurements with real shark skin on the contrary give an appreciable improvement in the performance.

Poroelastic surfaces find also applications in aeroacoustics, as a matter of fact owls are well known for their particularly silent flight, especially in the high frequency spectrum. This characteristic is crucial for the owl in order to be able to capture its preys. Obviously it has inspired the scientific community to study their feathers, configuration and shape.



Figure 1.2: Feathers on owl's wing. Left: trailing edge. Right: leading edge. The differences in shape and mechanical properties, as rigidity, between the leading and trailing edge, is a consequence of the different flow regimes in the wing.

Several authors show promising results in characterizing the acoustic properties of the owl's skin and their physical mechanisms. In particular Lilley [80] presents three main characteristics of the owl, which can suppress its airborne noise: the feathers leading edge is shaped like a comb; the trailing edge forms a fringe and also multiple "filaments" in

the bottom surface of wing and legs. In the same work the authors also present some experimental and empirical evidence on the aeroacoustics mechanism behind the three elements above.

Another example on the same topic is represented by Jaworski and Peake [70] which study the acoustic scattering problem of a poroelastic half-plane encountering an incident plane wave. This configuration, a simplified owl's wing, explains how the properties of this surface can suppress the noise. They conclude that the combined effects of elasticity and porosity can produce a weaker noise amplification.

Recent computational simulations performed by Chen et al. [33] confirm that the leading edge shape of the feathers truly suppress noise and enhance the lift generation.

Bioinspired aerodynamic surfaces include another peculiar example in the butterflies wings. In figure 1.3 the surface of a "Peacock butterfly" is enlarged in order to show the multiple scales involved; the wing structure present firstly a series of overlapped scales similar to the shark, but looking closely we can observe that each scale has a complicate permeable structure.

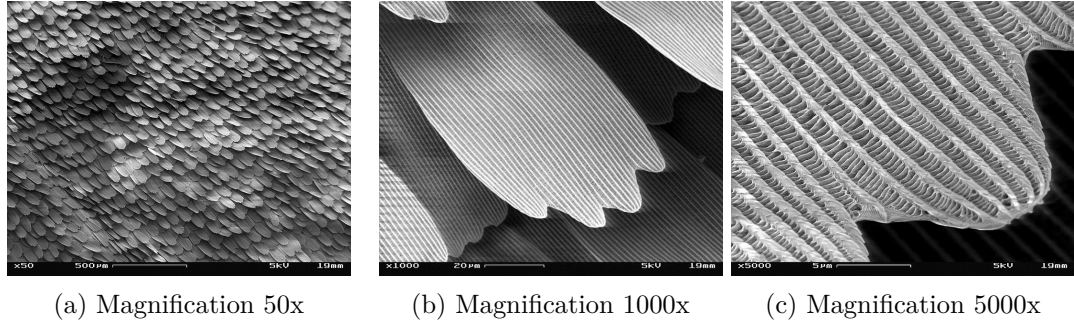


Figure 1.3: Particular of a Peacock butterfly wing, taken with a Scanning Electron Microscope. Images from [wikimedia.org](https://commons.wikimedia.org).

The work of Slegers et al. [112] studies the effect of such porous structure on the performance in the flight of butterflies. Using cameras to measure the kinematics of their flight, they can compute their efficiency to "climb" (i.e. generate lift) and the stroke amplitude and frequency. The authors conclude that the porous structure of their wing gives a boost in climbing efficiency about 30%; this result clearly stresses out the importance of the poroelastic coating of the wings. Even though the butterfly flight aerodynamic is extremely complex, it is clear that the peculiar structure of the wing's surface is critical for their aerodynamic performances, as also Srygley and Thomas [114] confirm.

The last example consist of super-hydrophobic surfaces; these surfaces are water repellent, i.e. the water can slide over them with much less resistance, resulting in very small values of wettability. This behavior is caused by the microscopic structure which forms the surface (see figure 1.4), in reality the rugosities are arranged in a quasi-regular way, in

order to be able to capture air pockets that rest within the "valleys". These air inclusions provoke an effective slip at the air-liquid interface that cause the drag reduction; they also change the contact angle of droplets. The work of Bottaro et al. [20] summarize the above aspect and their applications.

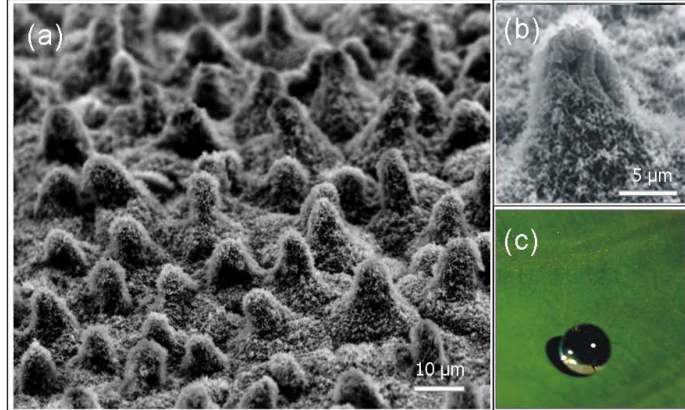


Figure 1.4: (a) Scanning electron microscopy (SEM) image showing the structure of lotus leaf, (b) higher order of magnification on the single protuberance forming the surface and (c) a water drop with high contact angle, attaining an almost spherical shape. Images from Stratakis et al. [115].

Interested readers can find more examples and broaden the above key aspect in Bhushan [18] and Tropea and Bleckmann [117].

1.1.1 Riblets and shark-skin surfaces

We have shown that natural surfaces can be an inspiration to find strategies in solving many problems in aerodynamics; in the following we focus especially on drag reduction.

Is known that the total drag contribution can be separated into different components and the classical decomposition is between viscous drag (sometimes referred to skin friction) and pressure drag.

$$\int_{A_\sigma} \left[\underbrace{\left(\frac{p}{\rho} \mathbf{I} \right) \cdot \mathbf{n}_\sigma}_{\text{pressure drag}} + \underbrace{(\nu \nabla \mathbf{v}) \cdot \mathbf{n}_\sigma}_{\text{viscous drag}} \right] dA, \quad (1.1)$$

In (1.1) A_σ is the solid interface of some body where a no-slip condition is applied, and \mathbf{n}_σ is its outward normal. This section talks about the existing ways to reduce the viscous part of the drag since, historically, it has attracted more interest and/or it has made more progress.

In the following, we refer as the wall shear stress in the turbulent case as:

$$\tau = ((\mu + \mu_t) \nabla \bar{v}) \cdot \mathbf{n}_\sigma = (\mu + \mu_t) \frac{\partial \bar{u}}{\partial y}, \quad (1.2)$$

where μ_t is the turbulent viscosity and \bar{u} is the average velocity stream-wise component; in the laminar case the definition rest the same with the appropriate corrections (there is no turbulent viscosity and no notion of average velocity).

Most of the industrial applications involves turbulent flow; there is a lot of research that aims to reduce the skin-friction in this regime. Table 6.3.1 in the book of McLean [87] includes a wide list of technique already been proposed on the problem.

As the same author pinpoints, the most effective and, probably the most practicable concept is that of riblets. Riblets are alternating ridges aligned in the stream-wise flow direction and regularly arranged, as figure 1.5 shows.

These surfaces are capable of align the turbulent flow along the mean flow direction, smoothing the fluctuation of the cross-flow in the viscous sublayer. Reducing these fluctuations close to the surface, the turbulent momentum transfer is also reduced and so the shear stress, causing the reduction in skin-friction.

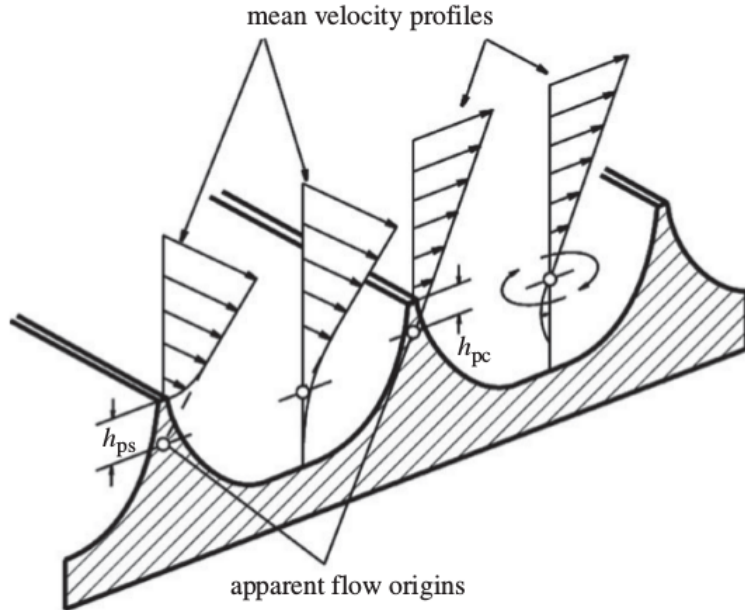


Figure 1.5: Schematics of the *protrusion height* concept. The mean velocity profiles for the stream-wise and cross-flow velocities are shown. In presence of a ridge it is possible to extrapolate the point of zero velocity from the velocity gradient outside the riblet; finding respectively, the *stream-wise protrusion height* h_{ps} and the *cross-flow protrusion height* h_{pc} . Image from Bechert et al. [15].

The viscous drag reduction correlates well with the spacing between the ridges expressed in wall units s^+ ; the typical shape of the latter relation is depicted in figure 1.6, where the vertical axis shows the drag reduction against the s^+ . This general shape of the curve, in which the skin friction decreases in certain range of spacing and then increase as the ridge spacing increases, is caused by a competition between the capacity of riblets to obstruct lateral fluid flow and an increase in the penetration of high speed vortices inside this manufactured roughness.

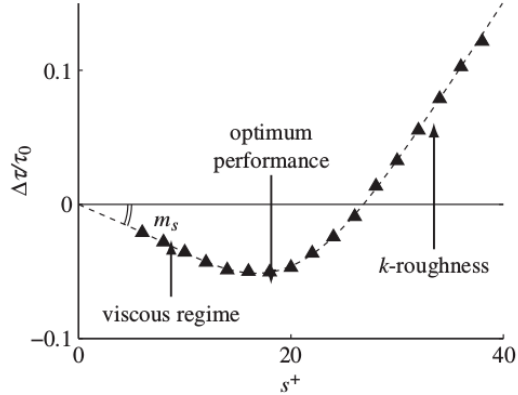


Figure 1.6: Example of drag reduction relation to the ridge spacing. The maximum performance is normally around $s^+ = 15$, the picture shows also that when the riblet are really tight one another the laminar case is retrieved. On the contrary when the riblets are far away one another their performance is comparable to rough plate case. Image from Jimenez et al. [71].

This last physical explanation of the riblets performances is presented in the schematics 1.7, where the gray areas show high skin-friction regions caused by the down-wash motion generated by the near-wall vortices. Is it clear that, when the riblets are too big, the vortices can penetrate inside the groove and, actually, increase the skin-friction, due to larger area exposed to the local velocity. On the contrary, when the riblets are smaller, the high speed vortex "touches" only the tip of the ridges, so only a small local area of the surface experiences high-shear stresses.

The slope m_s of the curve in figure 1.6 can be predicted by linear stability theory or by means of empirical correlations García-Mayoral and Jiménez [50].

Computing the performance of such surfaces can be expensive, since the most reliable quantitative theory for such problems consist of direct numerical simulations (DNS) or experiments. There is only one more theory, besides the already cited expensive ones, that uses the concept of *protrusion height*, shown in figure 1.5, to correlates the shape of these protrusions to the drag reduction (cf. Luchini et al. [81]). The *protrusion height* is defined as the vertical distance between the riblet top ridge and the point of zero velocity,

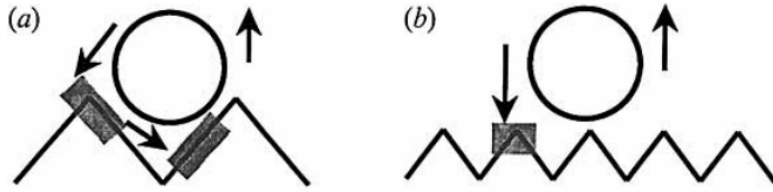


Figure 1.7: Two different sizes of riblets are shown when interacting with a sublayer vortex. In gray it is represented the area where friction is important. Clearly when both sizes are comparable the surface experience a larger friction and the performance is lowered. Image from Choi et al. [34].

extrapolated from the constant velocity gradient outside above the protrusions. It appears that especially the difference of protrusion heights, computed from the stream-wise h_{ps} and cross-flow h_{pc} profile, correlates very well with the drag reduction, and the two quantities can be computed with a simple Stokes problem over the local geometry of the grooves. The last result has been analyzed by Gomez-de Segura et al. [57] and come out with an empirical law for the drag reduction, relating the previous protrusion heights with the permeability expressed in wall units:

$$DR \approx 0.04 \left(\sqrt{K^+_s} - \sqrt{K^+_c} \right), \quad (1.3)$$

where K^+_s and K^+_c are the stream-wise and cross-flow permeability tensor components. This law establishes an instrument to estimate the drag reduction from a given geometry of the wall (the permeability tensor can be computed within the porous media homogenization approach as chapter 2 explain).

Another important characteristic of riblets performance is that they are robust in off-design conditions, such as in presence of yaw (misalignment between flow and riblets ridges) and tip ridges erosion (García-Mayoral and Jiménez [49]).

Besides some very specific application such as sailing competitions (the hulls of the USA challengers in the America's Cup 1987 and 2010), the massive utilization of this technology is still in question. Producing such surfaces in a larger area, like the roof of a car or the wing of an airplane, can be an issue for a routine use; because riblets size need to be very little to be effective.

Riblets like surface has been observed in nature for many years, for example Martin and Bhushan [84] found out that skimmer birds (*Rynchops*) have riblets like grooves in their beak, since they fly with it under the water surface to catch fishes. However, as already introduced, the most clear example of such natural surfaces are shark skin. In his review, Dean and Bhushan [39] present the status of the shape optimization that has been done on the riblets trying to mimic the typical sawtooth shape seen in shark skin, showing that improvements of such geometries over the classical ones has yet to be proven. Shape

optimization on riblets geometry has been studied, the findings show that just a few % can be improved on the base line geometry Bechert et al. [15].

There is, actually, some controversial result in literature stating that surfaces, with actual shark skin replica, can indeed increase drag. Boomsma and Sotiropoulos [19] perform some simulations on actual shark skin denticles using the immersed boundary method; the authors find that in some configuration the actual drag increase up to 40%, but even though their numbers are probably too large (it is known that the immersed boundary method can generate some errors especially in computing forces at high Reynolds number), this can be a clue that the shark skin does not work with the same mechanism as riblets.

Experiments on such geometries are available in literature (Bechert et al. [14]). The authors have built a synthetic surface, made by artificial shark denticles posed on top of springs, and measure that, even with the introduction of surface elasticity, the actual drag was increased. However, they pinpoint that the actual shark flow regime is not steady as the experiments that he performed, and they speculate that the excellent swimming performance of the shark come from the separation control that flexible denticles can increase in the periodic oscillating flow that the swimming generates.

An experiment using DPIV on a NACA profile covered with actual skin samples of "*Isurus oxyrinchus*" mako shark, has been performed by Lang et al. [77], confirming that the flexibility of sharks denticles acts as a passive flow control in order to avoid early separation. In fact, the experiment proves that for angles of attack larger than 15° the flow reversal is almost completely avoided. The same author introduce the importance of the different geometries in various part of the body that obviously experience disparate flow conditions. Motta et al. [92] perform a detailed collection of flexibility and scale measurement of different shark species that can be valuable for future studies.

Swimming experiments from Oeffner and Lauder [96], who used a flat plate covered with real shark skin, also confirm the previous flow control mechanism and also make some conjectures about possible thrust enhancing controlled by the same movable scales that can move away the leading edge vortex.

Also Itoh et al. [69] show that movable rugosities can outperform riblets, the authors measure the drag reduction of a seal fur (that present fibrous movable surface) against a riblet surface in an experimental channel; their results are shown in figure 1.8.

Compliant surfaces can, in reality, move accordingly to the surface pressure gradients along the boundary layer and so respond to the pressure fluctuation over the surface itself. This mechanism is already known to be beneficial in delaying the transition to turbulence and many authors have presented theoretical and experimental evidence on the effectiveness of this solution Carpenter [32], Bushnell et al. [27].

In conclusion we have seen that, in order to reduce turbulent skin-friction drag, riblets and natural surfaces use various mechanism such as: sublayer vortices interaction, compliance and separation control. Such solutions have proven to be effective in some cases, but they are related mostly in reducing the viscous component of the total drag. In the next section we introduce another class of solutions that try to act instead mostly on the

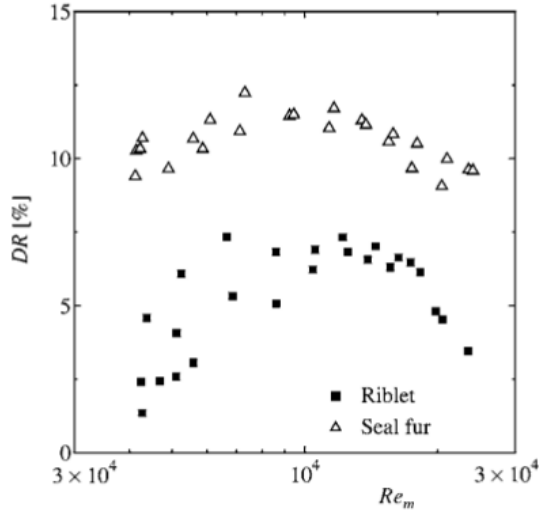


Figure 1.8: Performance comparison between a riblet surface against a seal fur. The drag reduction has been computed as: $DR\% = \frac{\Delta\tau}{\tau_0}\%$ Image from Itoh et al. [69].

pressure component.

1.1.2 Permeable surfaces

1.1.3 Bluff bodies

There is some experimental evidence that in laminar cases the generation of some *slip velocity*, at the interface between the permeable surface with a fluid, can decrease the friction drag (Beavers and Joseph [13]). However, in the turbulent case it seems that the instabilities developing at the interface can cause an increase in drag up to 40% (Jimenez et al. [71] and Breugem et al. [21]); these instabilities mechanism is further explained in the section 1.3. It is important to pinpoint that the permeable surfaces cited in the above references are all rigid.

The pressure contribution to the resistance is usually the most significant one in bluff bodies applications, and even in highly streamlined body it is around 10% of the total drag. Researchers have tried to find a way to modify the pressure distribution around a bluff body to reduce the associated resistance, and also damp the force oscillation on the body (drag and/or lift).

The pressure drag on a bluff body depends mostly on the difference between the low pressure on the rear part of the body, where there is usually a separated flow region, and the high pressure in the forward part. This idea is sketched in figure 1.9 where two different

pressure distributions are shown; the black one represents the classical solid body, and the green one is with a porous layer at the back of the body.

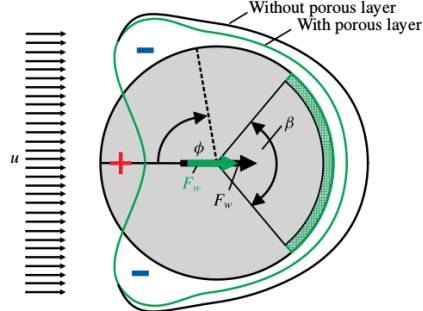


Figure 1.9: Diagram showing an example of angular pressure distribution around a cylinder for viscous flow. The black line is the case of a solid body, the green one is the modified pressure in presence of a porous layer at the rear part. Image from Klausmann and Ruck [73].

The favorable increase in the back pressure is due to the low speed laminar flow in the porous media that is ejected in the back region where the separation take place. Even in very high speed turbulent flow the fluid inside permeable surface exhibits a very high energy loss due to the strong dissipation that the medium provides, resulting in a low speed flow ejected downstream of the body.

The permeable interface, producing a slip velocity, can modify the boundary layer that develops above it and with which produces less shear and vorticity; it can also modify the stability characteristics of the flow. The instability around a cylinder is due to the shear layer that forms in the top part of the body, when the flow starts to decelerate. This shear layer exhibits a Kelvin–Helmholtz type instability that develops in the classical Von-Karman wake.

This two hypothetical mechanisms has been tested using numerical simulation by multiple authors: Bruneau and Mortazavi [24], Bruneau and Mortazavi [25], Bhattacharyya and Singh [17], Naito and Fukagata [93] and Mimeau et al. [91]. These works study the flow around some classical two dimensional bluff bodies (cylinder, square cylinder, Ahmed body section, 3D hemisphere) with the add of a porous layer.

These works show some very promising result on multiple quantities, like: decrease of enstrophy, lower oscillations in lift signal, drag reduction, regularization of the wake and lower pressure gradients, even if the porous medium is rigid in their case. An example is shown in figure 1.10 where the turbulent flow field downstream to a square cylinder is shown; the picture show how the porous layer strongly regularize the wake.

The previous works show that porous medium parameters, like the medium resistance or its vertical extension, have important effects on the results. The variety of results seems

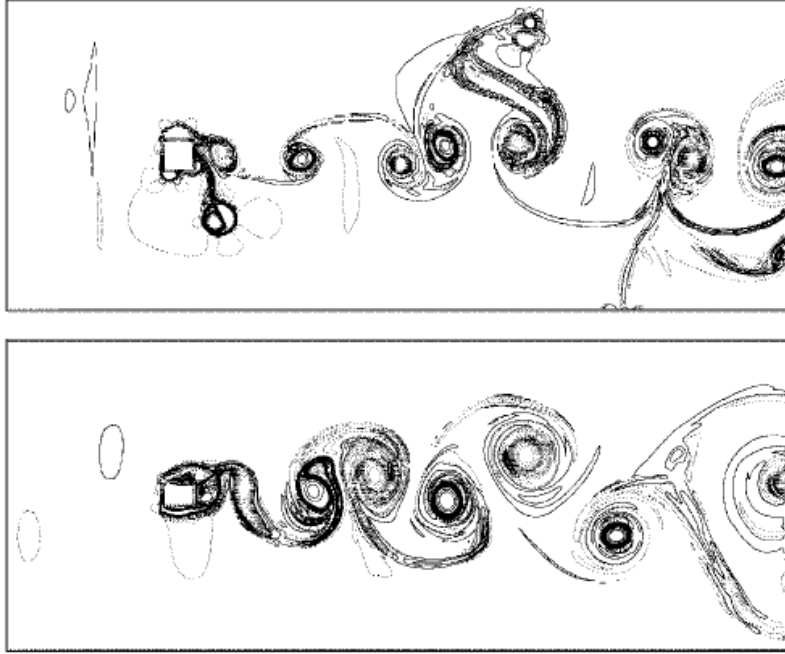


Figure 1.10: Square cylinder vorticity contour for $Re = 30000$. Top: solid case. Bottom: porous case with layer extension $h = 10\%D$.

to agree (at least qualitatively) that increasing the porous medium extension over a certain limit is not beneficial, and they also show that the resistance of the medium should not be excessive in order to be effective (high/medium porosity are the best).

In all these works we also observe a reduced pressure drop between the front and the rear of the body, a reduced drag, a delays in the vortex shedding and regularization on both the frequency and amplitude of shredded vorticities oscillations.

These works show very optimistic results, but they should be taken with some care; only few cases are three-dimensional, they all use a modeling approach for the porous medium based on a simplified version of the VANS (Volume Average Navier-Stokes equations, see section 1.2.2), without performing any validation of the method. Sometimes they also use the equations outside their field of validity (there is some discussion in the scientific community in using the previous version of VANS equations for highly turbulent flows).

The lack of validation reflects the fact that reliable experiments of such porous coatings are almost non existent in literature. There is also some confusion in literature on how to compute the forces on such bodies surrounded by a porous coating, these differences have taken by some authors as Naito and Fukagata [93] to over-estimate the forces and their predictions are not inline with the literature. With some theoretical bases Caltagirone [28] establishes that the approach used by Bruneau and Mortazavi [24] is the correct one

for that specific version of the VANS used by all the previous authors, REFERENCE TO SECTION IN THE VANS CHAPTER WHERE THERE IS THE FORMULA TO COMPUTE FORCES.

The approach of Favier et al. [44] differentiates itself from the previous works; the authors use a numerical method that includes the dynamic of a moving porous medium made of fibers at the back of a cylinder. Their results in a laminar flow case agree with the prediction of a stabilization of the wake and show some more realistic values of drag reduction, about 15%. The difficulties in this approach is that the medium dynamic introduces many mechanical parameters that are not easily identifiable for natural surfaces.

A similar model has been used by Venkataraman and Bottaro [118]; they applied a movable porous coating in the top part of NACA airfoil. In this case the synchronization between the oscillations of the structures and the natural frequency of the fluid is responsible for the pressure distribution modification. They have shown the robustness of this solution in a wide range of angle of attack, in the best case they have found some lift enchantment and a drag reduction around 10%.

Later on Rosti et al. [106] worked on a similar configuration with only one movable flap on the low pressure side of the airfoil; the results both numerical and experimental qualitatively agree (on the flow mechanism) with the results in the complete porous case.

WHEN IT WILL BE PUBLISHED SHOW SOME RESULTS ON THE 3D SPHERE USING HOMOGENIZATION giuseppe ... [56]

The very few experiments in literature on this porous coatings show less promising results associated to drag reduction.

For example, Heenan and Morrison [64] perform an experiment in which they take a backward facing step with a porous insert in the re-circulation region. His measurement show a 13% decrease of the peak of pressure at the wall and a relocation of the detachment point further downstream. A maximum of 9% of drag reduction was observed. The effect of adding a porous surface in this case was to limit the pressure fluctuations that cause the re-circulation bubble unsteadiness.

Later Klausmann and Ruck [73] study a 3D cylinder with a porous insert in the back (as in figure 1.9); the authors use a wind tunnel testing with pressure measurements around the body and particle image velocimetry (PIV) flow capture. Their results confirm that the porous layer on the leeward side increases the pressure in that zone, causing the reduction of drag. The drag reduction measured was around 10% over various Reynolds number (in turbulence range); this value was sensible to the geometrical parameters of the medium as the position and its size. At our knowledge this is the first example of actual measurements of flow quantities using PIV, that can later be used to perform some validation on different numerical models. The above results are partially confirmed by a similar experimental analysis by Grizzetti et al. [61].

Some other experimental data can be found in the case of flow over aquatic canopies (Zhang and Nepf [132], Segalini et al. [108] and Hamed et al. [63]) even though the published data is limited and the experiments show the presence of a free surface that increase the

difficulty of the problem and limit the possible use as simple validation.

From this section the main physical mechanism that are tied to permeable surfaces has been introduced. Even though the different approaches in literature seems to be discordant in the predicted values of some fundamental items such as the forces, a general trend on all data shows that porous coatings can be effectively used in many situations. It is clear that the scientific community needs much more experimental data in order to develop new and improved numerical and theoretical models for such permeable coatings.

1.1.4 Canopy flow

Another important class of flows over poroelastic carpets are the *canopy flows* as named in literature. These type of problems involve flows over flexible slender structure such as trees and aquatic vegetation. The behavior of wind over plants is very important in a large variety of fields, like: the transport of substances as CO_2 and nutrients or preventing agricultural damage (wind-throw of crop fields); also some similarities with urban canopies can be found Ghisalberti [52].

The boundary layer profile over such canopies differs substantially from the rough wall one, as figure 1.11 shows. The vegetation resistance causes the creation of an inflection point in the mean velocity profile that lead to a mixing layer type of instability near the vegetation top. As a consequence of such instabilities Finnigan [46] shows that the vegetation can heavily modify the turbulence spectra as a result of the interface instabilities and the coherent structures above it. The two bottom pictures in figure 1.11 outline the above statements; the spectrum in case of canopy flow presents a larger peak in the frequency of the mixing layer instability, a steeper slope in the energy cascade part due to the larger dissipation inside the permeable layer and possible high frequency peaks associated to the swinging of the pants that can emit or absorb small scales vortices.

Is it clear from literature that the dynamic of the permeable substrate made by vegetation is extremely important and should always be taken into account to fully generalize the physics in such problems involving moving canopies; Nepf [94] shows how the interface between aquatic plants and the free flow can be largely modified due to the movement of the fibers.

In order to discriminate the different behavior of the fibrous structure it is convenient to introduce some important non-dimensional parameters used in fluid structure interaction problems:

$$m^* = \rho_\beta / \rho_\sigma, \quad C_Y = \rho_\beta U^2 s^3 / E, \quad s = L/\ell,$$

The first one is the *mass ratio*, the second is called *Cauchy number* and the last one is the *slenderness* of the structure. The mass ratio m^* is a measure of the added mass effects caused by the solid inertia, however these effects are usually negligible in case of fibrous permeable media. The Cauchy number C_Y defines the static deformation of a fiber caused by the fluid flow (E is the modulus of elasticity of the solid material); when Cauchy number is greater than unity, important deformations are expected. This last

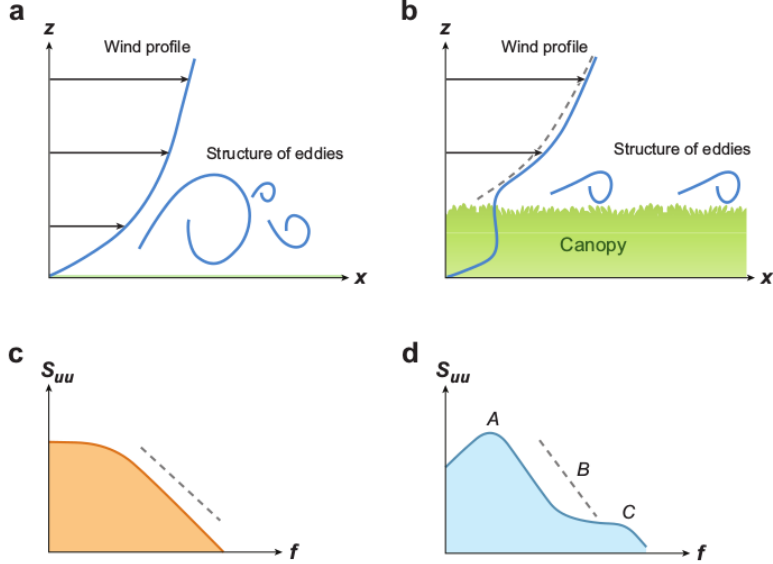


Figure 1.11: Figure **a** and **b** show respectively the schematics of the mean flow over a rough wall and a canopy flow; the difference in the eddy size is clear, also the inflection point in the canopy flow velocity profile is transparent. The figure **c** and **d** instead show the turbulent spectra for the two different flows above, in case of rough wall a Kolmogorov type of spectra can be retrieved; in case of canopy flow it is possible to see a larger peak in the frequency of the mixing layer instability, a steeper slope in the energy cascade part and high frequency peaks at high frequencies. Image from De Langre [38]

parameter is extremely important since it controls a phenomenon called *reconfiguration* that leads to drag reduction (Gosselin and De Langre [59] and Alvarado et al. [4]). The reconfiguration can be defined as the capability of the structure to adopt a new shape when forced by a flow, it can become more streamlined to reduce its exposed frontal area with the aim to reduce the total drag. When dealing with this phenomenon one should take into account of the frontal area A and the drag coefficient C_D as an ensemble, in order to avoid misinterpretation of the drag reduction; in figure 1.12 the ratio of the couple AC_D has been represented for different natural structures against the Cauchy number and it's evident that for a $C_Y > 1$ a drastic drag reduction can be observed.

The overall reconfiguration of the permeable medium can lead to pressure recovery and a wake regularization applied when applied to a bluff body, as the experiments by Gosselin and De Langre [59] show.

Another non-dimensional number to mention is the *reduced velocity*, it can be derived from the previous ones:

$$U_R = \sqrt{C_Y s/m^*},$$

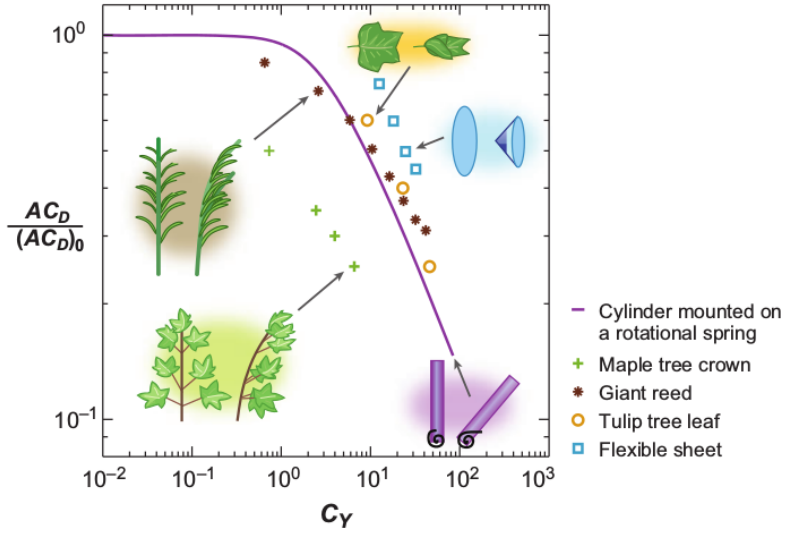


Figure 1.12: The effects of the Cauchy number C_Y on the drag reduction are presented in the figure. The drag reduction has been represented as the ratio between the frontal area A and the drag coefficient C_D at static condition (subscript 0) and the dynamic condition (no subscript). Image from De Langre [38]

this number is used dealing with vortex induced vibration of slender structures; when it is near to one, dynamical coupling between the fluid and the structure is expected, such as resonance or lock-in phenomena.

Canopies can also help to prevent separation in presence of adverse pressure gradients, Belcher et al. [16] show an analysis of the flow over an hill covered with canopies using either numerical and experimental data; the authors show how the permeable layer can present a re-circulation region inside the canopy in the decreasing slope side of the hill, this zone move the separation away from the flow over the hill to the internal structure of the canopy.

It is important to pinpoint that the above results are restricted to fibrous or slender structures and they cannot be extrapolated in general for different porous structure and shapes, even though similar mechanisms are expected.

The research on canopy flow embraces a wide range of configurations and this makes very difficult the comparison of the results since most of the authors use very different models in a lot of various regimes of velocities, using flexible structures with very different shapes. Even if experiments are easier to find, like Segalini et al. [108], Segalini et al. [109], Maza et al. [85], Barsu et al. [9] and Alvarado et al. [4], there is no quantitatively mathematical model established for the fluid and structure equations and almost all models available rely on empirical correlations that fit the data in each different application.

1.2 Models for flows through porous surfaces

In this section we want to show some insight of the various models characteristic of flows through poroelastic layers. In order to be as clear as possible we have taken as example a very simple geometry to sketch the problem; the flow over a wall that include flexible multiple filaments. This simple geometrical configuration still has all the characteristic and difficulties of more interesting applications, such as a bluff body with a poroelastic layer.

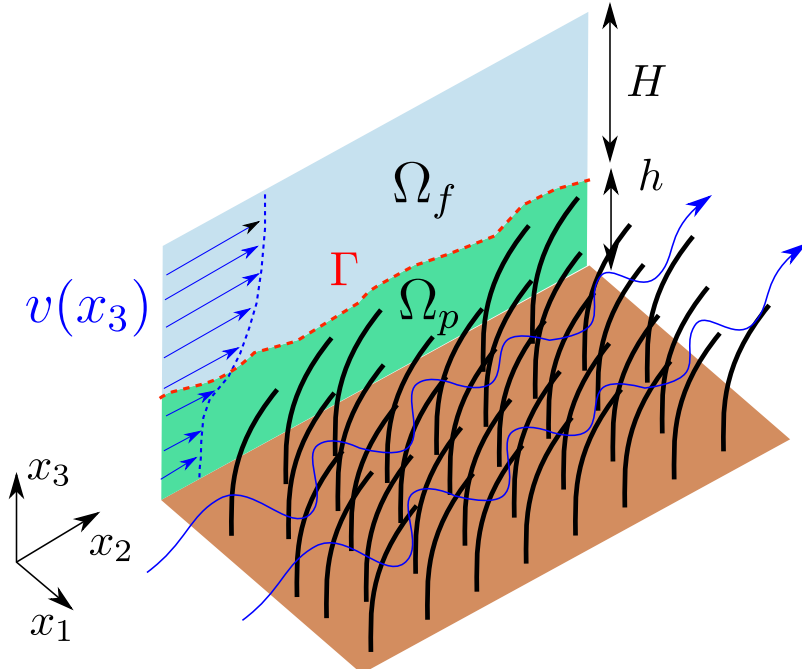


Figure 1.13: Sketch of a fully developed flow over a poroelastic surface made of multiple filaments.

The figure 1.13 shows a graphical schema of such flow; the main fluid direction is aligned with the x_2 axis and the projection of velocity stream-wise component is shown in the plane $x_2 - x_3$. Such flow can bend the filaments and, of course, go by their ensemble. The hypothetical surface that envelops all the filaments lid (Γ), defines the limit between the flow without obstacle (Ω_f) and the one inside the poroelastic medium (Ω_p), their projection are shown in the $x_2 - x_3$ plane.

In order to computationally solve this problem there are some key points to address:

- Length scales: the flow presents interaction at multiple scales. The flow can develop Kelvin–Helmholtz type instabilities on the interface (of size h) and they can even penetrate inside the medium and brake up to very small scales eddies. In order

to resolve this complex dynamic one should use a very fine numerical mesh (highly computational expensive) or come up with a model (like in the context of turbulence modeling). Turbulence dynamic can be also problematic; the hypothesis that pore size eddies can exist deep inside the porous medium is still at debate in the community. How to deal with such small scale dynamic and/or find a model is not an easy task.

- Compliance (fluid structure interaction): if the filaments are flexible, they can bend and swing due to the fluid impact on them. We have to take into account a mechanical solid model for the filaments (for example the Bernoulli beam), including also the computation of energy that the swing motion re-inject inside the fluid. This two-way coupling could also be really computational expensive in presence of a large number of filaments, and also, if the flexibility is important, one should in principle take into account the contact and repulsion between the fibers. If the porous medium has more complicated shape (like the scales in the butterfly wing) to come out with a simplified model for the solid dynamic is even more difficult and the use of a general FEA discretization is probably a necessity (increasing also the computational cost of the problem). Another approach consists of considering a "rheology" model for the medium, for example treating it like a porous medium that has elastic properties as an ensemble. Such models are applicable only to porous media where the solid inclusions are connected to each other; in principle they are convenient, computational speaking, but their mathematical description can be difficult.
- Anisotropy: the model used should be capable of treat permeable surfaces that have different responses when stressed in different directions. For example the geometrical disposition and/or the mechanical properties of the medium can be non-homogeneous, so it appear more permeable in one direction and show a preferential flow path.

Dupont et al. [40] had performed a LES simulation introducing a two way coupling for the fluid-structure interaction problem, they validate their code with video recording of a similar experiment and the frequency measurements of the Kelvin–Helmholtz instabilities at the interface agrees very well. They have not specified the computational configuration used, but they have mentioned an important high performance computing center in the acknowledgment which made us suppose that the computational power involved was substantial. Recently also in Marjoribanks et al. [83] a similar approach has been used.

Some other examples that solve the full coupled problem directly are in Pinelli et al. [99], Favier et al. [45] and Revell et al. [104], but in this case the number of filaments is small and so they can be though more as isolated filaments rather than a poroelastic medium.

Due to the computationally expensiveness of solving the problem directly, the scientific community has came out with different approaches that treat the porous domain with a generalized model that does not resolve the fine scale inside the filaments, but instead expressed them as a function of the larger length scales present in the fluid domain Ω_f .

These are called homogenization approaches and the key point in such methods are:

- The division of the overall domain in two different parts: the fluid domain Ω_f and the porous domain Ω_p
- Two different fluid models are solved in the two domains, in Ω_f the Naver-Stokes equations for incompressible Newtonian fluids are solved. In the porous part there are a number of different models that adds source terms in the former equations to take into account the presence of the porous medium.
- The two domains should be coupled together with a boundary condition at the interface or a special treatment for the equation in the transition region.
- A model for the dynamic of the solid porous part, it can model the structures directly or with an averaged rheology model.

The key points show above are extensively expanded, in chapter 2, for the homogenization method chosen in this thesis. However, in the next sections the two main branches in literature, that take into account the presence of a porous medium layer, are summarized in order to give a panoramic on all possible choices.

1.2.1 Isotropic drag models

In the case of flow through vegetation (canopy flows) it is common to use an isotropic drag model (the drag is equal in the three principal directions of the medium) for parameterize the resistance of the canopy. The drag can be a function of the wall normal direction, but in most of the application is taken as a constant. The isotropic hypothesis can be correct in case of dense vegetation; even if the vertical component of the resistance should be smaller. However since this models are mostly applied in channel problems where the mean flow is mostly stream-wise, the resistance in the vertical direction can be approximated in this manner; in applications where the transpiration of the interface is important (wake control of bluff body) the isotropic drag model is, certainly, not the most adequate.

The drag resistance is included in the Navier-Stokes equations as a sink:

$$\frac{\partial \mathbf{v}_\beta}{\partial t} + \mathbf{v}_\beta \cdot \nabla \mathbf{v}_\beta = -\frac{1}{\rho_\beta} \nabla p_\beta + \nu_\beta \nabla^2 \mathbf{v}_\beta - C_{Da} |\mathbf{v}_\beta| \mathbf{v}_\beta, \quad (1.4)$$

The sink term is quadratic in the velocity, but there is some evidence that the reconfiguration phenomena can change this relationship as a consequence of the drag reduction (Gosselin and De Langre [59] and Alvarado et al. [4]).

The sink term also includes the parameter a that is the frontal area per unit volume of the vegetation, this parameter is an expression of the porosity of the medium.

From our point of view this approach lack of strong mathematical formalism, on the basis of which one should be able to derive all the additional terms of the equations; as a

consequence, this method heavily relies on empirical relations. The other problem is that the isotropic hypothesis rules out the possibility to model the anisotropic nature of most of the surfaces in which we are interested (as equation (1.3) suggest the difference in the permeability along each direction can be important for drag reduction).

In the field of flows through vegetation some authors have successfully used this approach, for example Maza et al. [85] and Maza et al. [86] use it to study wave attenuation and Ghisalberti and Nepf [51], Battiato and Rubol [10] develop simple models for the 2D mean flow over a canopy.

1.2.2 Homogenization models

In this section we want to introduce the most used approach to derive the equations valid in the porous domain. The fundamental idea is to construct a micro-scale model, either for the fluid as for the solid, and then derive the macro-scale equations using some averaging operator over the micro-scale.

The two most used homogenization methods are the *Volume Averaging* method (Whitaker [124]), and the (*Multiple Scales*) method Mei and Vernescu [89]; they can be more broadly classified as perturbations methods. The key differences and the main results retrieved using these approaches are presented in the following.

Volume Averaging

The method of Volume Averaging has been developed to treat transport equations in porous media applications; in this case the presence of two different length scales is obvious, as can be evinced by figure 1.14.

The core idea of the methods is to firstly define an average operator as $\langle \psi \rangle^\beta = \frac{1}{V_\beta} \int_V \psi dV$ in this case the variable ψ represents any vector or scalar variable in the system of equations that we want to homogenize, for Navier-Stokes they are the velocity and the pressure.

The average operator has the purpose to "scale up" the equation, in fact the second crucial step of the method is to decompose the variables as proposed by Gray [60]:

$$\psi = \underbrace{\langle \psi \rangle^\beta}_{O(L)} + \underbrace{\tilde{\psi}}_{O(\ell)}, \quad (1.5)$$

Equation (1.5) shows how each variable can be decomposed in an averaged part that contains only spatial variations at the macro-scale L and a *fluctuation* part that contains only the micro-scale ℓ spatial variations.

The decomposition can be injected in the transport equations that we want to homogenize, and after some mathematical manipulations it is possible to retrieve the new averaged



Figure 1.14: Schematics of a porous medium system of size L , with a zoom on the microscopic structure and its scale ℓ . Image from Whitaker [124].

equations that include only variables of order L . Since this is the method chosen to develop our work, all the technical details are explained in chapter 2.

To introduce briefly some other aspects about the method, we show as example, how to derive the homogenized version of the Stokes equation. The described problem is a flow inside a rigid porous medium, as the one in figure 1.14. The Stokes equation valid for the fluid phase, indicated with the β subscript, reads:

$$0 = -\frac{1}{\rho_\beta} \nabla p_\beta + \nu_\beta \nabla^2 \mathbf{v}_\beta, \quad (1.6)$$

Here it is important to pinpoint that equation (1.6) is valid only in the liquid phase and to solve it we have to consider a no-slip boundary condition at the interface with the solid phase, with the difficulties that come to define the complex structure of the solid inclusion. Applying the Averaging Method, we can derive a homogeneous version of (1.6) that is valid in all the porous domain that include the two different phases, the solid and the liquid one.

The homogenized version of the last is the famous Darcy equation $\langle \mathbf{v}_\beta \rangle^\beta = -\frac{\mathbf{K}^\varepsilon}{\mu_\beta} \nabla \langle p_\beta \rangle^\beta$, developed with this approach by Whitaker [121].

In the Darcy equation it is possible to recognize two additional quantities that arise from the averaging procedure, the first one is a scalar called porosity ε that represents the ratio between the volume of the liquid present in a reference volume, over the total volume itself. The second one is the tensor \mathbf{K} called permeability, it expresses the resistance of the porous medium that affects the flow in its travel. The term \mathbf{K} plays the same role as C_{Da} in the isotropic drag model; the main difference is that the permeability tensor can

be computed directly from the geometry of the medium (see chapter 2) so it does not rely on empirical relations. Also the tensorial nature of this terms allows us to model porous inclusions that are anisotropic.

Applications of the theory include flows where inertial terms are not negligible (Whitaker [123]), porous media with small deformations (Whitaker [122]) and high deformations (Hus-song et al. [66]), turbulent problems (Soulaine and Quintard [113], Breugem et al. [21]), interface between a permeable medium and a free flow (Beavers and Joseph [13]), multi-phase systems (Whitaker [120]) and heat transfer (Carbonell and Whitaker [30]).

It is impossible to go into details of the derivation of equation for each specific problem, but we hope that the readers have understood the differences between this method and the isotropic drag model of the previous section.

Multiple Scales

The multiple scale method is similar to the previous one; and it has also been applied to similar problems in the context of porous media applications.

In this method we start with the assumption of scale separation between ℓ , the micro-scale, and L , the macro-scale. The scale separation factor can be defined as $\epsilon = \ell/L \ll 1$. Using the same examples as before we show how to compute the homogenized version of the Stokes equation for fluid flow through porous media. We introduce the micro-scale and the macro-scale coordinates defined respectively as:

$$X_i = \frac{\tilde{x}_i}{L}, \quad x_i = \frac{\tilde{x}_i}{\ell},$$

where x_i are the original eulerian coordinate of the problem. Using the above separation factor it is possible to expand the variables of the problem (pressure and velocity) into different magnitude orders indicated as superscript:

$$\psi(X_i, x_i) = \psi^{(0)}(X_i, x_i) + \epsilon\psi^{(1)}(X_i, x_i) + \epsilon^2\psi^{(2)}(X_i, x_i) + O(\epsilon^3),$$

Injecting this decomposition inside the equation (1.6) it is possible to derive a set of system of equations for each order of the expansion. It can be shown that analyzing each equation in the set, we can retrieve the homogenized equation:

$$v_i^{(0)} = -K_{ij} \frac{\partial p^{(0)}}{\partial X_j}, \quad (1.7)$$

In which either the pressure or the velocity fields appear only at the order zero, and the equation depends only on the macro-scale length.

The same permeability tensor \mathbf{K} as before is retrieved, with the same definition and interpretation. It is clear that for this example problem we end up with the same set of homogenized equation; what change is the starting hypotheses of the method and the mathematical development to compute them.

A full analysis of the dualism of the two approaches can be found in the work by Davit et al. [37].

The multiple scale has also been used to study many other problems: inertial effects (Mei and Auriault [88], Skjetne and Auriault [111]), coupling between a free fluid and a porous media (Mikelic and Jäger [90]), porous media with small deformations (Auriault and Sanchez-Palencia [7]), heat conduction in composites (Auriault [8]), rigid and moving permeable layers (Zampogna and Bottaro [127], Lăcis et al. [76] and Zampogna and Bottaro [129]).

It is also worth of mention another homogenization based method called *Mixture Theory*. It is based on a similar approach as the previous ones and Rajagopal [102] have shown that it is possible to retrieve the same equation as the previous two methods in case of porous media flow.

1.3 Stability of flows over permeable surfaces

Flows through submerged aquatic plants exhibit large scale vortices at the top of the vegetation, advecting along the flow direction and causing a periodic waving of the plants, referred to as monami (if the fluid is air) and honami (in case of water) Inoue [68], Ackerman and Okubo [1]. The effect of the onset of the monami is depicted in figure 1.17.

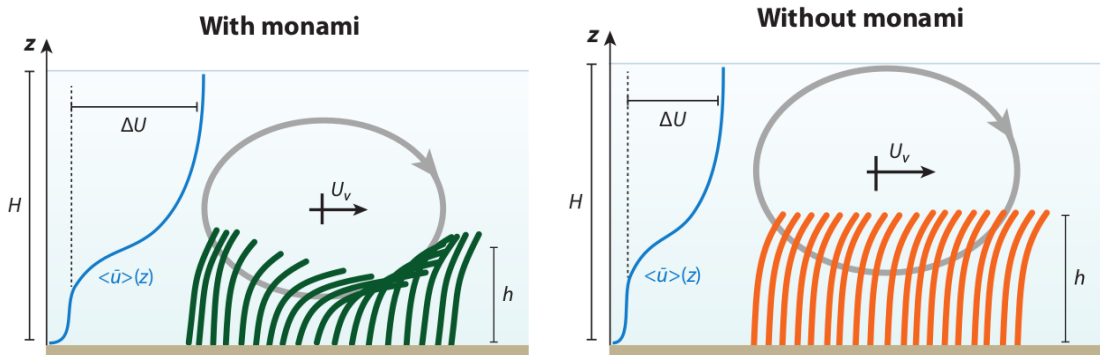


Figure 1.15: Left: when the drag of the canopy is high enough it generates canopy-scale vortices by Kelvin-Helmholtz instability. These vortices may interact with the flexible vegetation and generate a waving motion called monami. Right: when this interaction is too weak, the canopy bend only. Image from Nepf [94].

Vortices arise from the nonlinear amplification of a Kelvin-Helmholtz instability mode, related to the presence of an inflection point in the base flow profile (Asaeda et al. [6]); the profile itself is inflectional because the fluid is slowed down by the drag exerted by the canopy, whose modeling has recently been addressed (Py et al. [100], Singh et al. [110],

Zampogna et al. [131] and Tilton and Cortelezzi [116]). The correct prediction of the onset and characteristics of the Kelvin-Helmholtz instability is important for assessing the effects of turbulence (Finnigan [46], Jimenez et al. [71]) in particular to:

- understand how the vertical exchange of momentum occurs Ikeda and Kanazawa [67].
- clarify how the transport of CO₂ and dissolved nutrients or sediments takes place. This exchange takes place between the obstructed vegetation flow and the free over-flow motion (Gambi et al. [48], Eckman [41], Grizzle et al. [62]).
- assess the changes in the morphology of the vegetation in inland or coastal wetlands in response to continuous periodic forcing Asaeda et al. [6], Patil and Singh [97].

One of the possible approaches to study how and when these instabilities develop is the linear stability analysis; in the following section we briefly introduce the key assumption and simplifications of the method over other possible choices, and in the next section some results in the context of permeable surfaces are presented.

1.3.1 Stability theory generalities

Stability theory in general covers the modeling of transition of fluid systems towards not stables states and at least turbulence. In its most basic form the theory gives us a fast and robust method to compute the frequency and grow rate of the unstable modes, if there is any, in the base flow.

The linear stability relies on the decomposition of the flow variables \mathbf{q} into a steady-state part $\bar{\mathbf{q}}$, called base flow, and an unsteady part $\tilde{\mathbf{q}}$:

$$\mathbf{q}(\mathbf{x}, t) = \bar{\mathbf{q}}(\mathbf{x}) + \eta \tilde{\mathbf{q}}(\mathbf{x}, t)$$

Here η is a small amplitude parameter. Than the unsteady part is simplified by the hypothesis to have a general wave form

$$\tilde{\mathbf{q}} = \hat{\mathbf{q}} e^{i\Theta},$$

where $\hat{\mathbf{q}}$ is the amplitude and Θ is the phase of the perturbation. The choice made to determine the time and space dependence of either the phase function and the amplitude determine a certain hierarchy inside the stability theories; figure 1.16 below show the main choice made in literature and the theory that derives from it:

In our case we have limited our study on the linear stability theory (LST), a local approach based on mode decomposition. In the LST we make the hypothesis that the amplitude and the base flow depend only on the wall normal spatial coordinate (parallel flow) and the phase function take into account the periodicity in time and in the stream-wise and cross-flow directions. The complete formulation is in the following equation:

$$\tilde{\mathbf{q}}(\mathbf{x}, t) = \hat{\mathbf{q}}(x_2) e^{i(\alpha x_1 + \beta x_3 - \omega t)}$$

	Denomination	Basic state assumption	Amplitude function	Phase function Θ
Global	TriGlobal PSE-3D	$\partial_1 \bar{\mathbf{q}} \ll \partial_2 \bar{\mathbf{q}}, \partial_3 \bar{\mathbf{q}}$	$\bar{\mathbf{q}}(x_1, x_2, x_3)$ $\bar{\mathbf{q}}(x_1^*, x_2, x_3)$	$\hat{\mathbf{q}}(x_1, x_2, x_3)$ $\hat{\mathbf{q}}(x_1^*, x_2, x_3)$
	BiGlobal	$\partial_1 \bar{\mathbf{q}} = 0$	$\bar{\mathbf{q}}(x_2, x_3)$	$\hat{\mathbf{q}}(x_2, x_3)$
Nonlocal	PSE	$\partial_1 \bar{\mathbf{q}} \ll \partial_2 \bar{\mathbf{q}}, \partial_3 \bar{\mathbf{q}} = 0$	$\bar{\mathbf{q}}(x_1^*, x_2)$	$\hat{\mathbf{q}}(x_1^*, x_2)$
Local	OSE	$\partial_1 \bar{\mathbf{q}} = \partial_3 \bar{\mathbf{q}} = 0$	$\bar{\mathbf{q}}(x_2)$	$\hat{\mathbf{q}}(x_2)$

Figure 1.16: Classification of modal linear stability theories. Table reported from Juniper et al. [72].

where α is the stream-wise wave-number, β is the cross-flow wave-number and ω is the wave phase.

Casting this form for the pressure and velocity inside the Navier-Stokes equation and neglecting the second order terms (η^2), the equations became linear and describe the evolution of the perturbations, taking the base flow as an input of the problem. If we make the choice to impose that α and β are real and ω is complex the problem became a generalized eigenvalue one. The above choice is made in order to study the stability of the perturbations in their time evolution and it is known as *temporal stability*. The generalized eigenvalue problem for the wave phase has the form

$$A\hat{\mathbf{q}} = \omega B\hat{\mathbf{q}}$$

The solution gives the frequency (real part of the eigenvalues) and the growth-rate (imaginary part) of the perturbation modes (eigenvectors) of the flow.

The above introduction of the method is quite condensed, however, a lot of literature has been developed in these years on the subject, (Juniper et al. [72], Criminale et al. [35], Schmid and Henningson [107]); the problem has also been extensively studied in his computational aspect by Canuto et al. [29].

Monami/Honami and Kelvin-Helmholtz rolls

We have already pinpointed that the above framework for the stability problem has been applied in some porous media flow (canopy) configurations, also including the vegetation movement. Because of the flexibility of the vegetation, some theoretical studies have focused on the modeling of the stems of the aquatic plants and their displacement in response to the forcing by the water flow (Py et al. [100], Patil and Singh [97], Gosselin and De Langre [58] and Py et al. [101]).

It has been studied in Finnigan [46] that these large coherent structures control turbulence dynamics over the canopy. Movements of the latter generate sweeps (and ejections) of fluids that generates the counter-rotating stream-wise eddy evolving as Kelvin-Helmholtz rolls. The complex evolution of vortices is shown in figure 1.17.

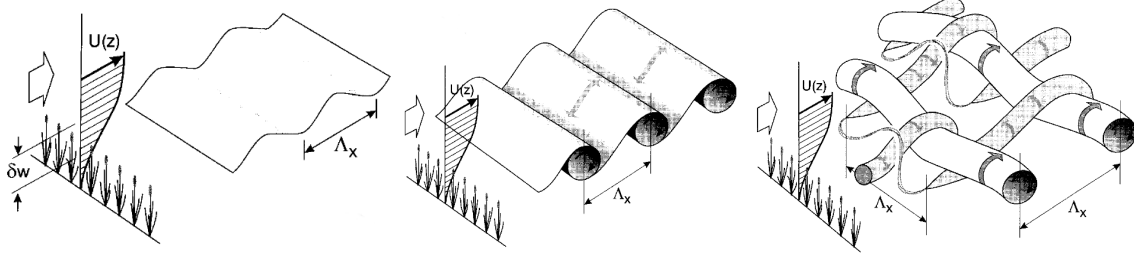


Figure 1.17: Left: first emergence of the Kelvin-Helmholtz instability. The growth-rate is proportional to the shear magnitude at the inflection point. Center: the instability evolves in rollers consisting of high vorticity that are spaced with a similar wave-length Λ_x as the previous stage. Right: secondary instabilities in the rollers lead to their kinking and pairing, coherent structures show up in the transverse and stream-wise dimensions. Image from Finnigan [46].

However, Kelvin-Helmholtz vortices occur whether or not, the plants bend and to ascertain causes and effects to first order it is acceptable to focus on rigid porous structures. The flow over and through a submerged array of rigid, cylindrical pillars has been the basis of the approach by Ghisalberti and Nepf [54], Ghisalberti and Nepf [51] and Ghisalberti and Nepf [53], who have conducted a series of careful experiments; their results have often been used by fluid dynamicists to put forth and test theoretical hypotheses to predict the frequency and wavelength of the large scale vortical motion, for a variety of conditions. The configuration studied consists of a regular grid of rigid pillars, orthogonal to the surface, of identical height h ; in some of the theoretical models proposed to analyze the stability of this system, the Rayleigh equation is used throughout the water channel, with or without a drag term in correspondence of the canopy Raupach et al. [103], Py et al. [100], Singh et al. [110], Zampogna et al. [131] and Luminari et al. [82] have recently demonstrated that the addition of a drag term through the vegetation reduces the amplification factor of the Kelvin-Helmholtz instability throughout the whole range of wave-numbers and increases mildly the wavelength of the fastest growing mode. In chapter 3 we study how the perturbation of the base flow affects the predicted amplification factor and wave-length, we test the difference between the isotropic drag model and the tensorial approach, in order to show which is the most robust approach for stability computations.

Chapter 2

Volume Average Method

Do not worry about your difficulties in mathematics; I can assure you that mine are still greater.

- Letter to junior high school student Barbara Wilson,
January 7, 1943, *Albert Einstein*

2.1 Introduction

Maximum 10 lines recalling some of the things said in the previous chapter.

2.2 Derivation of VANS equations for 3D incompressible fluids

2.2.1 Definition of the averaging filter

In the figure 2.1 is an illustration of our porous problem; in the same figure we show all the main definition that we need to introduce in order to develop our mathematical approach.

Let ψ_β be an arbitrary vector or scalar field defined on the volume V where x is its centroid, we can define two different spacing average operator.

$$\langle \psi_\beta \rangle^\beta|_x = \frac{1}{V_\beta} \int_{V_\beta(x)} m(\mathbf{y}) \psi_\beta(\mathbf{x} - \mathbf{y}, t) dV_\beta, \quad (2.1)$$

$$\langle \psi_\beta \rangle|_x = \frac{1}{V} \int_{V_\beta} m(\mathbf{y}) \psi_\beta(\mathbf{x} - \mathbf{y}, t) dV_\beta, \quad (2.2)$$

$\langle \psi_\beta \rangle^\beta$ is called the *intrinsic average* and $\langle \psi_\beta \rangle$ is the *superficial average*. For the sake of a less heavy notation the $|_x$ has been dropped in the following, within mind that the

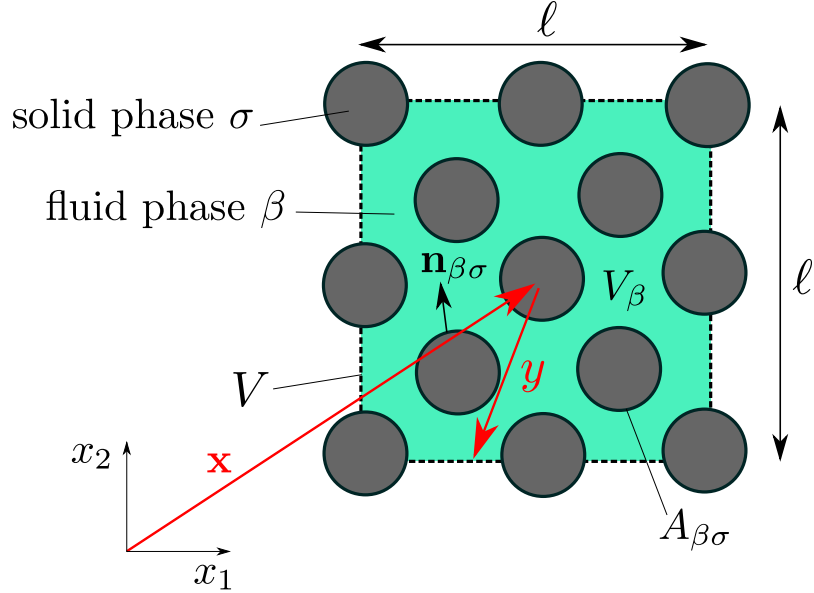


Figure 2.1: Illustration of the REV concept.

volume averaged quantities are intended to be computed in the center of the REV. The filter m act as a ... it is required that

$$\int_{V_\beta(\mathbf{x})} m(\mathbf{y}) dV_\beta = 1$$

Also for the sake of simplicity we will consider a filter m to be rectangular and we will not maintain it in the formulation...

The porosity is defined as:

$$\varepsilon = \frac{V_\beta}{V} \quad (2.3)$$

So we can define the relationship:

$$\langle \psi_\beta \rangle = \varepsilon \langle \psi_\beta \rangle^\beta \quad (2.4)$$

2.2.2 Theorems involving derivatives of spatial averaging

Theorem 2.2.1 (Spatial averaging theorem). *Let ψ_β be a scalar quantity defined in the liquid phase β , then:*

$$\langle \nabla \psi_\beta \rangle = \nabla \langle \psi_\beta \rangle + \frac{1}{V} \int_{A_{\beta\sigma}} \psi_\beta \mathbf{n}_{\beta\sigma} dA \quad (2.5)$$

Corollary 2.2.1 (Vector form of 2.5). *The vector form of the spatial averaging theorem is given by:*

$$\langle \nabla \cdot \psi_\beta \rangle = \nabla \cdot \langle \psi_\beta \rangle + \frac{1}{V} \int_{A_{\beta\sigma}} \mathbf{n}_{\beta\sigma} \cdot \psi_\beta dA \quad (2.6)$$

Corollary 2.2.2. *Applying the theorem 2.5 to a constant field $\psi_\beta = 1$ we obtain:*

$$\nabla \varepsilon = - \int_{A_{\sigma\beta}} \mathbf{n}_{\sigma\beta} dA, \quad (2.7)$$

Theorem 2.2.2 (General transport theorem). *Let ψ_β be a scalar quantity defined in the liquid phase β , then:*

$$\frac{\partial}{\partial t} \int_{V_\beta(t)} \psi_\beta dV = \int_{V_\beta(t)} \frac{\partial \psi_\beta}{\partial t} dV + \int_{A_{\beta\sigma}(t)} \psi_\beta (\mathbf{n}_{\beta\sigma} \cdot \mathbf{w}) dA, \quad (2.8)$$

where \mathbf{w} is the point velocity of the solid-liquid interface $A_{\beta\sigma}$.

2.2.3 Averaged continuity equations

The continuity equation for a Newtonian ... reads:

$$\left\langle \frac{\partial \rho_\beta}{\partial t} \right\rangle + \langle \nabla \cdot (\rho_\beta \mathbf{v}_\beta) \rangle = 0 \quad (2.9)$$

Applying 2.5 to the second term we get:

$$\langle \nabla \cdot (\rho_\beta \mathbf{v}_\beta) \rangle = \nabla \cdot \langle (\rho_\beta \mathbf{v}_\beta) \rangle + \frac{1}{V} \int_{A_{\beta\sigma}} \mathbf{n}_{\beta\sigma} \cdot \rho_\beta \mathbf{v}_\beta dA \quad (2.10)$$

and applying fist the definition of superficial average, than 2.8 to the first one:

$$\left\langle \frac{\partial \rho_\beta}{\partial t} \right\rangle = \frac{1}{V} \int_V \frac{\partial \rho_\beta}{\partial t} dV = \quad (2.11)$$

$$= \frac{1}{V} \left[\frac{\partial}{\partial t} \int_V \rho_\beta dV - \int_{A_{\beta\sigma}} \rho_\beta (\mathbf{n}_{\beta\sigma} \cdot \mathbf{w}) dA \right] \quad (2.12)$$

$$= \frac{\partial \langle \rho_\beta \rangle}{\partial t} - \frac{1}{V} \int_{A_{\beta\sigma}} \rho_\beta (\mathbf{n}_{\beta\sigma} \cdot \mathbf{w}) dA \quad (2.13)$$

The boundary condition at the interface $\mathbf{w} = \mathbf{v}_\beta$ imply that the integrals in 2.10 is equal to the integral in 2.13 so we end up with:

$$\frac{\partial \langle \rho_\beta \rangle}{\partial t} + \nabla \cdot \langle \rho_\beta \mathbf{v}_\beta \rangle = 0 \quad (2.14)$$

Adding the hypothesis of incompressible fluid:

$$\frac{\partial \varepsilon}{\partial t} + \nabla \cdot \langle \mathbf{v}_\beta \rangle = 0 \quad (2.15)$$

2.2.4 Averaged momentum equations

$$\frac{\partial \mathbf{v}_\beta}{\partial t} + \nabla \cdot (\mathbf{v}_\beta \mathbf{v}_\beta) = -\frac{1}{\rho_\beta} \nabla p_\beta + \nu_\beta \nabla^2 \mathbf{v}_\beta \quad (2.16)$$

first term

Using theorem 2.8:

$$\left\langle \frac{\partial \mathbf{v}_\beta}{\partial t} \right\rangle = \frac{\partial \langle \mathbf{v}_\beta \rangle}{\partial t} - \frac{1}{V} \int_{A_{\beta\sigma}(t)} (\mathbf{n}_{\sigma\beta} \cdot \mathbf{w}) \mathbf{v}_\beta dA, \quad (2.17)$$

second term

Using theorem 2.6:

$$\langle \nabla \cdot (\mathbf{v}_\beta \mathbf{v}_\beta) \rangle = \nabla \cdot \langle \mathbf{v}_\beta \mathbf{v}_\beta \rangle + \frac{1}{V} \int_{A_{\beta\sigma}} \mathbf{n}_{\sigma\beta} \cdot (\mathbf{v}_\beta \mathbf{v}_\beta) dA, \quad (2.18)$$

The boundary condition at the interface $\mathbf{w} = \mathbf{v}_\beta$ imply that the integrals in the last two equations are equals so we end up with the total left end side of the momentum equation:

$$\frac{\partial \langle \mathbf{v}_\beta \rangle}{\partial t} + \nabla \cdot \langle \mathbf{v}_\beta \mathbf{v}_\beta \rangle$$

third term

Using theorem 2.5:

$$\left\langle -\frac{1}{\rho_\beta} \nabla p_\beta \right\rangle = -\frac{1}{\rho_\beta} \nabla \langle p_\beta \rangle - \frac{1}{V} \int_{A_{\beta\sigma}} \frac{p_\beta}{\rho_\beta} \mathbf{n}_{\sigma\beta} dA, \quad (2.19)$$

fourth term

Expressing the ∇^2 operator with the identity $\nabla^2 = \nabla \cdot (\nabla)$ (laplacian = div (grad)), and applying the theorem 2.6:

$$\left\langle \nu_\beta \nabla^2 \mathbf{v}_\beta \right\rangle = \langle \nu_\beta \nabla \cdot \nabla \mathbf{v}_\beta \rangle = \nabla \cdot \langle \nu_\beta \nabla \mathbf{v}_\beta \rangle + \frac{1}{V} \int_{A_{\beta\sigma}} \mathbf{n}_{\sigma\beta} \cdot \nu_\beta \nabla \mathbf{v}_\beta dA, \quad (2.20)$$

Now re-using the theorem 2.6 on the term $\langle \nabla \mathbf{v}_\beta \rangle$ we get:

$$(2.20) = \nabla \cdot \nu_\beta \nabla \langle \mathbf{v}_\beta \rangle + \nabla \cdot \left(\frac{1}{V} \int_{A_{\beta\sigma}} \mathbf{n}_{\sigma\beta} \cdot \nu_\beta \mathbf{v}_\beta dA \right) + \frac{1}{V} \int_{A_{\beta\sigma}} \mathbf{n}_{\sigma\beta} \cdot \nu_\beta \nabla \mathbf{v}_\beta dA = \\ = \nu_\beta \nabla^2 \langle \mathbf{v}_\beta \rangle + \nabla \cdot \left(\frac{1}{V} \int_{A_{\beta\sigma}} \mathbf{n}_{\sigma\beta} \cdot \nu_\beta \mathbf{v}_\beta dA \right) + \frac{1}{V} \int_{A_{\beta\sigma}} \mathbf{n}_{\sigma\beta} \cdot \nu_\beta \nabla \mathbf{v}_\beta dA =$$

and using Gauss theorem on the second term

$$= \nu_\beta \nabla^2 \langle \mathbf{v}_\beta \rangle + \nabla \cdot \left(\frac{1}{V} \int_{V_\beta} \nabla \cdot \nu_\beta \mathbf{v}_\beta dV_\beta \right) + \frac{1}{V} \int_{A_{\beta\sigma}} \mathbf{n}_{\sigma\beta} \cdot \nu_\beta \nabla \mathbf{v}_\beta dA =$$

which is zero due to the continuity equation

$$= \nu_\beta \nabla^2 \langle \mathbf{v}_\beta \rangle + \frac{1}{V} \int_{A_{\beta\sigma}} \mathbf{n}_{\sigma\beta} \cdot \nu_\beta \nabla \mathbf{v}_\beta dA \quad (2.21)$$

The above use of the Gauss theorem, to prove that the first integral term is zero, can be bypassed in case of rigid porous media. Which due to the b.c. at the fluid-solid is zero.

Before continue the development lets put all the pieces together:

$$\frac{\partial \langle \mathbf{v}_\beta \rangle}{\partial t} + \nabla \cdot \langle \mathbf{v}_\beta \mathbf{v}_\beta \rangle = -\frac{1}{\rho_\beta} \nabla \langle p_\beta \rangle + \nu_\beta \nabla^2 \langle \mathbf{v}_\beta \rangle + \\ + \frac{1}{V} \int_{A_{\beta\sigma}} \left(-\frac{p_\beta}{\rho_\beta} \mathbf{n}_{\sigma\beta} + \nu_\beta \nabla \mathbf{v}_\beta \cdot \mathbf{n}_{\sigma\beta} \right) dA \quad (2.22)$$

2.2.5 Length scale decomposition

To further simplify the equations we use the decomposition proposed by Gray [60]:

$$\psi_\beta = \langle \psi_\beta \rangle^\beta + \tilde{\psi}_\beta \quad (2.23)$$

The non-homogeneous terms in equation 2.22:

$$\langle \mathbf{v}_\beta \mathbf{v}_\beta \rangle = \langle \langle \mathbf{v}_\beta \rangle \langle \mathbf{v}_\beta \rangle \rangle + 2 \langle \langle \mathbf{v}_\beta \rangle \tilde{\mathbf{v}}_\beta \rangle + \langle \tilde{\mathbf{v}}_\beta \tilde{\mathbf{v}}_\beta \rangle \quad (2.24)$$

Applying the superficial average to the perturbation term is possible to demonstrate that it has null mean:

$$\langle \tilde{\psi}_\beta \rangle = \langle \psi_\beta \rangle - \langle \langle \psi_\beta \rangle^\beta \rangle = \langle \psi_\beta \rangle - \varepsilon \langle \psi_\beta \rangle^\beta = 0$$

Using this results to equation (2.24):

$$\langle \mathbf{v}_\beta \mathbf{v}_\beta \rangle = \varepsilon \langle \mathbf{v}_\beta \rangle^\beta \langle \mathbf{v}_\beta \rangle^\beta + \langle \tilde{\mathbf{v}}_\beta \tilde{\mathbf{v}}_\beta \rangle \quad (2.25)$$

Now expressing the time derivative in the intrinsic form:

$$\frac{\partial \langle \mathbf{v}_\beta \rangle}{\partial t} = \frac{\partial (\varepsilon \langle \mathbf{v}_\beta \rangle^\beta)}{\partial t} = \frac{\partial \varepsilon}{\partial t} \langle \mathbf{v}_\beta \rangle^\beta + \varepsilon \frac{\partial \langle \mathbf{v}_\beta \rangle^\beta}{\partial t}$$

For each integral term of 2.22 we first apply the decomposition:

$$\begin{aligned} \frac{1}{V} \int_{A_{\beta\sigma}} -\frac{p_\beta}{\rho_\beta} \mathbf{n}_{\sigma\beta} dA &= \frac{1}{V} \int_{A_{\beta\sigma}} -\frac{1}{\rho_\beta} (\langle p_\beta \rangle^\beta + \tilde{p}_\beta) \mathbf{n}_{\sigma\beta} dA = \\ &= +\frac{1}{\rho_\beta} \nabla \varepsilon \langle p_\beta \rangle^\beta - \frac{1}{V} \int_{A_{\beta\sigma}} \frac{\tilde{p}_\beta}{\rho_\beta} \mathbf{n}_{\sigma\beta} dA \end{aligned} \quad (2.26)$$

The same for the other two terms:

$$\begin{aligned} \frac{1}{V} \int_{A_{\beta\sigma}} \nu_\beta \nabla \mathbf{v}_\beta \cdot \mathbf{n}_{\sigma\beta} dA &= \frac{1}{V} \int_{A_{\beta\sigma}} \nu_\beta \nabla (\langle \mathbf{v}_\beta \rangle^\beta + \tilde{\mathbf{v}}_\beta) \cdot \mathbf{n}_{\sigma\beta} dA = \\ &= -\nu_\beta \nabla \varepsilon \nabla \langle \mathbf{v}_\beta \rangle^\beta + \frac{1}{V} \int_{A_{\beta\sigma}} \nu_\beta \nabla \tilde{\mathbf{v}}_\beta \cdot \mathbf{n}_{\sigma\beta} dA \end{aligned} \quad (2.27)$$

Now we need to further develop the remaining terms, the viscous one became:

$$\nabla^2 \langle \mathbf{v}_\beta \rangle = \nabla^2 (\varepsilon \langle \mathbf{v}_\beta \rangle^\beta) = \varepsilon \nabla^2 \langle \mathbf{v}_\beta \rangle^\beta + \langle \mathbf{v}_\beta \rangle^\beta \nabla^2 \varepsilon + 2 \nabla \varepsilon \nabla \langle \mathbf{v}_\beta \rangle^\beta \quad (2.28)$$

the pressure one:

$$\nabla \langle p_\beta \rangle = \nabla (\varepsilon \langle p_\beta \rangle^\beta) = \varepsilon \nabla \langle p_\beta \rangle^\beta + \langle p_\beta \rangle^\beta \nabla \varepsilon \quad (2.29)$$

Putting now altogether:

$$\begin{aligned} &\frac{\partial \varepsilon}{\partial t} \langle \mathbf{v}_\beta \rangle^\beta + \varepsilon \frac{\partial \langle \mathbf{v}_\beta \rangle^\beta}{\partial t} + \nabla \cdot (\varepsilon \langle \mathbf{v}_\beta \rangle^\beta \langle \mathbf{v}_\beta \rangle^\beta) + \nabla \cdot (\varepsilon \langle \tilde{\mathbf{v}}_\beta \tilde{\mathbf{v}}_\beta \rangle) = \\ &= -\varepsilon \nabla \left(\frac{\langle p_\beta \rangle^\beta}{\rho_\beta} \right) - \frac{\langle p_\beta \rangle^\beta}{\rho_\beta} \nabla \varepsilon + \nu_\beta \varepsilon \nabla^2 \langle \mathbf{v}_\beta \rangle^\beta + \nu_\beta \langle \mathbf{v}_\beta \rangle^\beta \nabla^2 \varepsilon + 2 \nabla \varepsilon \nabla \langle \mathbf{v}_\beta \rangle^\beta \\ &+ \frac{1}{\rho_\beta} \nabla \varepsilon \langle p_\beta \rangle^\beta - \frac{1}{V} \int_{A_{\beta\sigma}} \frac{\tilde{p}_\beta}{\rho_\beta} \mathbf{n}_{\sigma\beta} dA \\ &- \nu_\beta \nabla \varepsilon \nabla \langle \mathbf{v}_\beta \rangle^\beta + \frac{1}{V} \int_{A_{\beta\sigma}} \nu_\beta \nabla \tilde{\mathbf{v}}_\beta \cdot \mathbf{n}_{\sigma\beta} dA \end{aligned} \quad (2.30)$$

After the proper simplification we have the final versions of the equations using only intrinsic quantities:

$$\begin{aligned} &\frac{\partial \varepsilon}{\partial t} \langle \mathbf{v}_\beta \rangle^\beta + \varepsilon \frac{\partial \langle \mathbf{v}_\beta \rangle^\beta}{\partial t} + \nabla \cdot (\varepsilon \langle \mathbf{v}_\beta \rangle^\beta \langle \mathbf{v}_\beta \rangle^\beta) + \nabla \cdot (\varepsilon \langle \tilde{\mathbf{v}}_\beta \tilde{\mathbf{v}}_\beta \rangle) = \\ &= -\varepsilon \nabla \left(\frac{\langle p_\beta \rangle^\beta}{\rho_\beta} \right) + \nu_\beta \varepsilon \nabla^2 \langle \mathbf{v}_\beta \rangle^\beta + \nabla \varepsilon \nabla \langle \mathbf{v}_\beta \rangle^\beta \\ &+ \frac{1}{V} \int_{A_{\beta\sigma}} \left(-\frac{\tilde{p}_\beta}{\rho_\beta} \mathbf{n}_{\sigma\beta} + \nu_\beta \nabla \tilde{\mathbf{v}}_\beta \cdot \mathbf{n}_{\sigma\beta} \right) dA \end{aligned} \quad (2.31)$$

The crucial difference between the superficial and the intrinsic quantities can be found in the averaged version of the continuity equations; in case of porosity that vary spatially (great advantage for using penalization methods) only the superficial velocity field is solenoidal.

The equation (2.31) is also *non-local* since it has volume average quantities and surface integrals. One should notice that at this stages the equations are not closed; because in (2.31) there are still two terms that depends on the perturbations of the pressure and velocity field. We will call it *sub-filter stresses* and *microscopic force* at the fluid-solid interface:

$$\zeta = \nabla \cdot (\varepsilon \langle \tilde{\mathbf{v}}_\beta \tilde{\mathbf{v}}_\beta \rangle)$$

$$\mathbf{F}^m = \frac{1}{V} \int_{A_{\beta\sigma}} \left(-\frac{\tilde{p}_\beta}{\rho_\beta} \mathbf{n}_{\sigma\beta} + \nu_\beta \nabla \tilde{\mathbf{v}}_\beta \cdot \mathbf{n}_{\sigma\beta} \right) dA$$

2.3 Closure problems

2.4 Interface condition

Penalization method Angot et al. [5] used in[24] [25] [26]...

We think that using a boundary condition at the interface is not a superior approach nor physically neither mathematically. Using penalization method the slip velocity at the interface can be computed as well as using a boundary condition, and either methods require a parameter to close the formulation, with the advantage using penalization method that the parameter is the spatial distribution of the porosity field that is trivial to compute known the geometry of the medium.

Also in case of very low Reynolds number the boundary condition can be a necessity since the Stokes equations, for the free fluid, and the Darcy one for the porous media are not mathematically compatible; but for $Re > 10$ when the Brinkmann model for the porous media is applicable the two set of equations are of the same order and the continuity of pressure and velocity can be imposed directly.

Also there is evidence in literature through numerical and computational experiments Ochoa-Tapia et al. [95] that exist a transition zone with the size of the pore scale in which the velocity and pressure have a continuous variation.

Chapter 3

Drag-model sensitivity of Kelvin-Helmholtz waves in canopy flows

While knowledge can create problems, it is not through ignorance that we can solve them.

- Asimov's New Guide to Science, 1984, Isaac Asimov

Gomez-de Segura et al. [57] state that their results agree with yours ??

3.1 Introduction

modify the introduction to not repeat the same parts that you have presented in the intro

Flows through submerged aquatic plants exhibit large scale vortices at the top of the vegetation, advecting along the flow direction and causing a periodic waving of the plants, referred to as monami [1]. Vortices arise from the nonlinear amplification of a Kelvin-Helmholtz instability mode, related to the presence of an inflection point in the base flow profile; [6] the profile itself is inflectional because the fluid is slowed down by the drag exerted by the canopy, whose modeling has recently been addressed [100] [110] [131]. The correct prediction of the onset and characteristics of the Kelvin-Helmholtz instability is important for assessing the effects of turbulence, in particular to

- understand how the vertical exchange of momentum occurs, 6
- clarify how the transport of CO_2 , dissolved nutrients or sediments takes place between the obstructed vegetation flow and the free overflow motion, 7–10 and also

- assess the changes in the morphology of the vegetation in inland or coastal wetlands in response to continuous periodic forcing [6] [97]

Because of the flexibility of the vegetation, some theoretical studies have focussed on the modeling of the stems of the aquatic plants and their displacement in response to the forcing by the water flow. [100] [97] However, Kelvin-Helmholtz vortices occur whether or not the plants bend and—to ascertain causes and effects to first order—it is acceptable to focus on the flow over and through a submerged array of rigid, cylindrical pillars. This has been the basis of the approach by Ghisalberti and Nepf [54] [51] [53] who have conducted a series of careful experiments; their results have often been used by fluid dynamicists to put forth and test theoretical hypotheses to predict the frequency and wavelength of the large scale vortical motion, for a variety of conditions. The configuration studied consists of a regular grid of rigid pillars, orthogonal to the surface, of identical height h ; in some of the theoretical models proposed to analyze the stability of this system, the Rayleigh equation is used throughout the water channel, with or without a drag term in correspondence of the canopy. [103] [100] [110] [131] have recently demonstrated that the addition of a drag term through the vegetation reduces the amplification factor of the Kelvin-Helmholtz instability throughout the whole range of wavenumbers and increases mildly the wavelength of the fastest growing mode; further unpublished work by the same authors shows that the addition of a mixing length turbulence model in the stability equations has but a negligible influence on the leading instability mode. Questions remain, however, on the accuracy of the drag model and on its sensitivity. A partial answer to these questions is provided in [131]: there, a different model, applicable within the vegetated layer and based on the equations ruling the behavior of a transversely isotropic porous medium, has been developed and the stability results appear to better match experimental correlations. This conclusion is, however, not consolidated yet, and further studies are needed to assess the influence of the model of the drag force through the vegetation, both in setting up a particular (inflectional) mean flow and on the onset and growth of Kelvin-Helmholtz waves. The present work addresses the points above through an adjoint-based sensitivity analysis along the lines of [20] the direct stability equations are written with account of viscosity, and the adjoint equations are found and solved in the temporal framework. Results in the spatial setting are discussed in Appendix B, where a digression is made on the computation of the group velocity of the instability waves by the use of the adjoint fields. The sensitivity functions to both mild modifications in the base shear layer and in the drag coefficient are computed and discussed. Finally, a different sensitivity analysis is developed on the basis of the recent anisotropic model by [131] and the results qualitatively compared to those obtained with the more conventional isotropic-drag-force model.

3.2 Model of the canopy flow

3.2.1 The mean flow

To obtain the mean flow on top of which small amplitude perturbations are superimposed, the procedure outlined by [51] and recently closely followed by [131] is used. For the sake of conciseness, the procedure which relies on several empirical correlations is not repeated here, aside from a few brief comments. A mildly inclined water channel is considered, with a canopy formed by rigid cylindrical dowels of height h equal to 13.8 cm and diameter $d = 0.64\text{ cm}$. The frontal area of the vegetation per unit volume, i.e., the packing density of the elements, is either $a = 0.04\text{ cm}^{-1}$ or 0.08 cm^{-1} ; the free surface is positioned at a level $H = 46.7\text{ cm}$ from the bottom plate and the flow velocity at the free surface, U_2 , varies from 4.4 to 13.7 cm/s . The Froude number, $F_r = \frac{U_2}{gH}$ is thus very low and water surface fluctuations can be ignored [22]. To a good approximation the mean flow can be taken as steady and parallel, with the streamwise velocity varying from the value U_1 at the bottom wall (not accounting for the thin bottom boundary layer) to the value U_2 at the top, near the free surface (3.1). The slope of the bottom surface is very small; it is denoted as S and, in the experiments by [51] varies from 1.8×10^{-6}

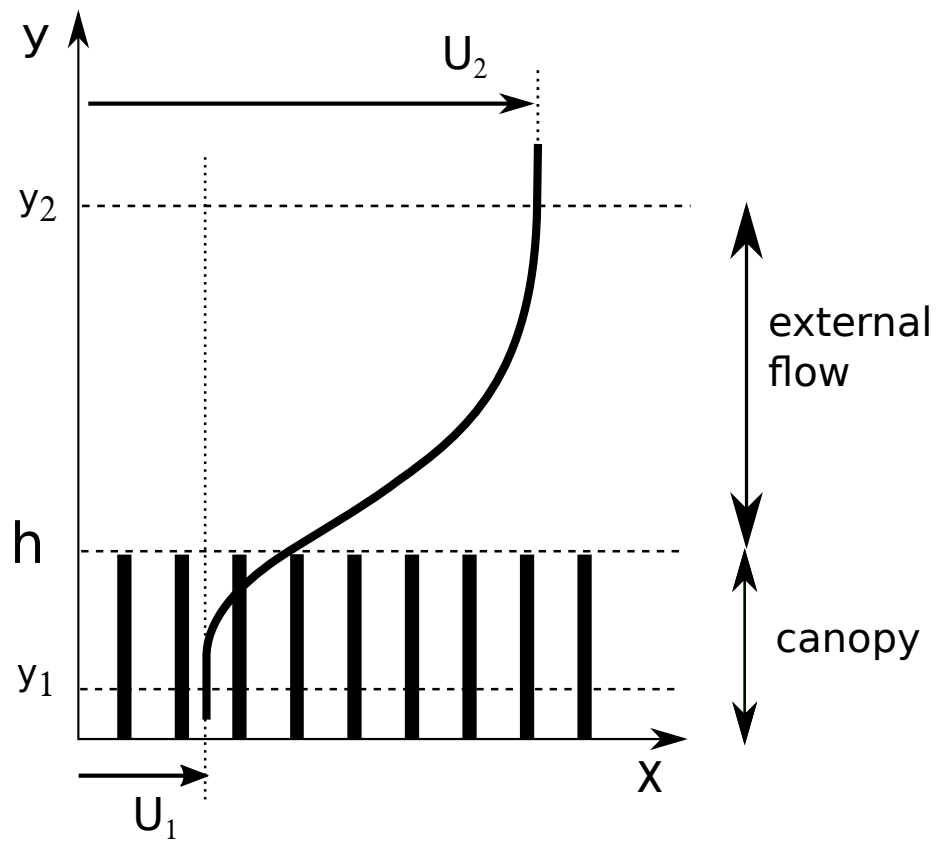


Figure 3.1: Configuration studied with main notations

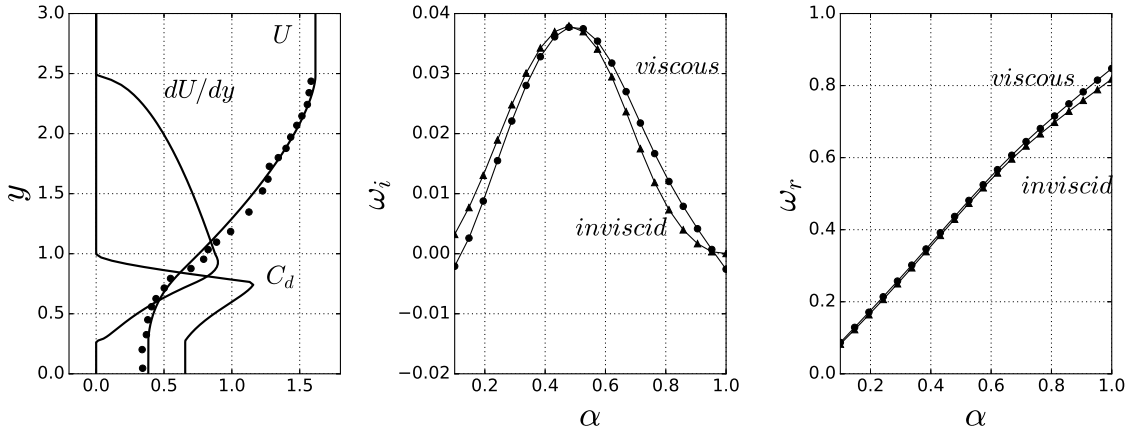


Figure 3.2: Left frame: mean flow U , together with experimental data points [51], its first derivative, and drag coefficient distribution (case G). Center: viscous and inviscid growth rates, ω_i , as a function of the streamwise wavenumber α . Right: corresponding frequencies, ω_r

to 10^{-4} ; such a slope provides the driving force for the motion. The viscous term is small compared to the turbulent diffusion term, so that the mean streamwise momentum equation can be approximated by

$$gS = \frac{\partial \bar{u}'v'}{\partial y} + \frac{1}{2}C_D(y)aU(y)^2 \quad (3.1)$$

with g the acceleration of gravity and C_d an isotropic drag function available from the experiments, variable across the canopy and equal to zero when $y \geq h$. The Reynolds stress $\bar{u}'v'$ is modelled with the Boussinesq assumption, introducing a turbulent viscosity which depends on a mixing length and on the gradient of the mean velocity U . Referring to [51] for details of the empirical correlations used to close the equations and the solution method, we limit ourselves here to stating that the results obtained for the mean flow are very close to those reported in [131] (cf. their Figure 3) and closely match experimental points for the cases G, H, I, and J considered (we use the same terminology of [54] [51] [53] to indicate the different flow configurations). An example of mean flow is reported in 3.2 (left frame). There, one can observe the computed flow (against discrete measurement points), its first derivative, and the drag coefficient distribution for one representative case (experiment G), used below also to discuss stability and sensitivity results. Other procedures have been employed in the past to calculate the mean flow, with satisfactory results. For example, [110] have considered a constant value of C_d through the canopy, while [131] have coupled, at a fictitious interface, the fluid equations outside the canopy to Darcy's law within the vegetation. Thus, for the purposes of the present paper, the mean flow is assumed as given; it could be, for example, simply a fit through experimental data.

Nonetheless, in Appendix A we provide some considerations on how C_d affects the mean flow in the model used here.

3.2.2 Stability and sensitivity equations

A temporal linear stability analysis is carried out, with the generic perturbation $q'(x, y, t)$ of the form

$$q'(x, y, z, t) = \tilde{q}(y)e^{i(\alpha x - \omega t)} \quad (3.2)$$

with α the real streamwise wavenumber and ω a complex number whose real part, ω_r , is the frequency of the mode and the imaginary part, ω_i , is the growth rate. The dimensionless linear stability equations in primitive variables read

$$\begin{aligned} i\alpha u + Dv &= 0, & D &= d/dy \\ \left[i(\alpha U - \omega) - \frac{D^2 - \alpha^2}{Re} + aC_d U \right] u + U' v + i\alpha p &= 0, & U' &= \frac{dU}{dy} \\ \left[i(\alpha U - \omega) - \frac{D^2 - \alpha^2}{Re} \right] v + Dp &= 0 \end{aligned} \quad (3.3)$$

with the perturbation velocity components which vanish when $y = 0$ and y_∞ . The upper boundary of the computational domain is taken far enough away from the lower boundary to ensure that the results do not vary upon modifications of y_∞ . All the terms in the equations are dimensionless; the mean speed through the shear layer, $U_m = \frac{U_1 + U_2}{2}$, is used to scale the disturbance velocity components, pressure is scaled with ρU_m^2 , distances with h , and time with h/U_m . The Reynolds number in the equations above is thus defined as $Re = \rho U_m / \mu h$, with ρ and μ the fluid's density and dynamic viscosity, respectively. The computations are performed both at the Re values of the experiments and in the inviscid limit ($Re^{-1} \rightarrow 0$), for comparison purposes. In the latter case, the boundary conditions are simply $v = 0$ at $y = 0$ and y_∞ . System 3.3 above and its boundary conditions are, in the following, also written in short notation as $\mathcal{L}q = 0$. The eigenvalues of the system are those complex values of ω which yield non-trivial solutions for u , v , and p . Two numerical collocation codes are written, and successfully compared; one is based on the equations in primitive variables form, the second solves an Orr-Sommerfeld-like equation (with the addition of the drag term) along the lines of [110]. In both cases, a spectral scheme based on N Chebyshev polynomials is used (N is typically equal to 300 to ensure grid-converged results), with an algebraic mapping between the physical and the spectral domains ([65]). Viscous and inviscid stability results for case G are shown in 3.2 (center and right frames); differences are small, in consideration of the fact that the Reynolds number of the viscous case is relatively large ($Re = 3450$). The viscous wavenumber of largest amplification is

found for $\alpha = 0.4790$; the waves are weakly dispersive, particularly at low wavenumbers (an original interpretation of phase and group velocities is proposed in Appendix B). The wavelength of largest growth is smaller than that found by [131] which was 0.73; this is related to the slightly different base flow in the two cases (in the present contribution a smoothing has been applied to the U velocity distribution to render dU/dy continuous across y) and highlights the sensitivity of this stability problem to base flow variations. Following [20] it is assumed that small variations in base flow and drag coefficient entail infinitesimal variations in the system's eigenvalues and eigenfunctions. We stress here the fact that C_d is identically equal to zero outside of the canopy, and this implies that there are no possible variations in C_d for $y \geq 1$. The sensitivity functions to variations in U and C_d are obtained by using the properties of the adjoint system which is defined from the Lagrange identity

$$0 = \delta\langle q^\dagger, \mathcal{L}q \rangle = \langle q^\dagger, \mathcal{L}\delta q \rangle + \langle q^\dagger, \frac{\partial \mathcal{L}}{\partial U} q \delta U \rangle + \langle q^\dagger, \frac{\partial \mathcal{L}}{\partial C_d} q \delta C_d \rangle + \langle q^\dagger, \frac{\partial \mathcal{L}}{\partial \omega} q \rangle \delta \omega \quad (3.4)$$

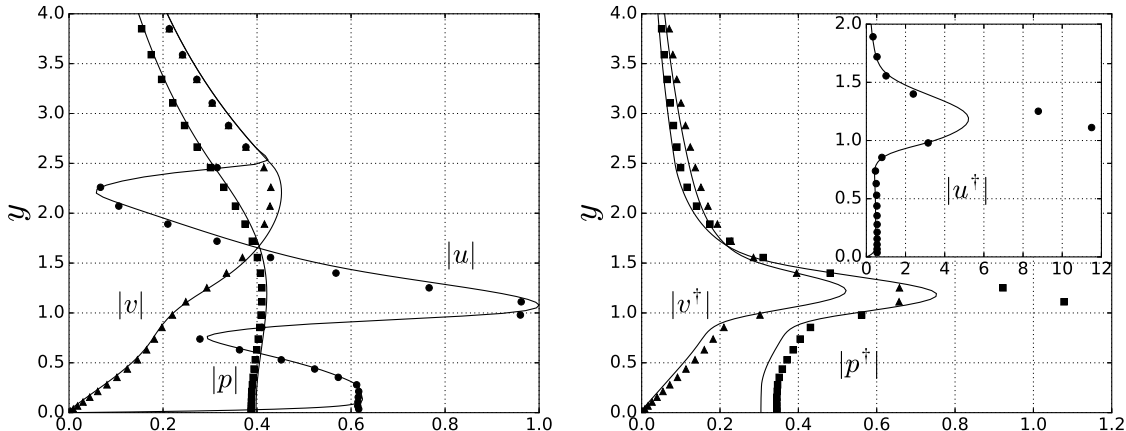


Figure 3.3: Moduli of direct (left frame) and adjoint (right frame) eigenfunctions for the viscous (continuous lines, $Re = 3450$) and the inviscid (symbols) case, in correspondence to the wavenumber of largest amplification.

and considering the effect of independent variations of U and C_d onto q and ω . It is found that

$$\delta\omega = \delta\omega_r + i\delta\omega_i = \int_0^{y_\infty} G_U(y)\delta U(y)dy + \int_0^1 G_{C_D}(y)\delta C_D(y)dy \quad (3.5)$$

with

$$\begin{aligned} G_U &= \alpha \left[\bar{v^\dagger v} + \bar{u^\dagger u} \right] + i(\bar{u^\dagger v})' - iaC_d \bar{u^\dagger u} \\ G_{C_d} &= -iaU \bar{u^\dagger u} \end{aligned} \quad (3.6)$$

the required sensitivity functions; the real parts of G_U and G_{C_d} express sensitivities to variations in the frequency of the mode while the imaginary parts are sensitivities to variations in the growth rate. Direct and adjoint eigenfunctions are normalized so that $N_\omega = 1$, with

$$N_\omega = \int_0^{y_\infty} \left[\bar{v^\dagger v} + \bar{u^\dagger u} \right] dy \quad (3.7)$$

An example of direct and adjoint eigenfunctions is provided in 3.3, both in the viscous case ($Re = 3450$) and in the inviscid limit, for $\alpha = 0.4790$. It is interesting to observe that while the direct eigenfunctions are almost overlapped, the same is not the case for the adjoint eigenfunctions, with the inviscid mode (drawn with symbols) which has a larger amplitude than the viscous one. The shapes of the direct eigenfunctions are very close to those reported in [131]. The adjoint modes reveal that the flow is most sensitive to streamwise forcing, particularly when it occurs slightly above the edge of the canopy. Source terms in the mass conservation and in the vertical momentum equations are much less effective.

3.3 SENSITIVITY RESULTS FOR THE ISOTROPIC DRAG MODEL

Some representative sensitivity functions are plotted in 3.4; viscous and inviscid results concur in showing that the largest sensitivities to variations of U are found right above the vegetation's edge, where there are peaks in the adjoint eigenfunctions and where d^2U/dy^2 vanishes. The U -sensitivities are negligible within the vegetated layer and for values of y larger than twice the canopy's height. The C_d -sensitivities are non-negligible only in close proximity of the interface. It is interesting to observe that real and imaginary parts of the U -sensitivity functions are shifted in y with respect to one another; this means that, for example, a localized perturbation at a given y position (above the canopy) might have a strong repercussion on the growth rate but not on the frequency of the most unstable Kelvin-Helmholtz mode, or vice versa. Comparing left and right frames of the figure, it is seen that inviscid G_U sensitivity functions display sharper peaks and steeper gradients, and yield larger variations in ω than their viscous counterparts in the proximity of the U inflection point, a clear consequence of the inviscid mechanism ruling the instability. In both the viscous and the inviscid models, the sensitivity to base flow variations is typically one order of magnitude larger than the sensitivity to changes in the drag coefficient.

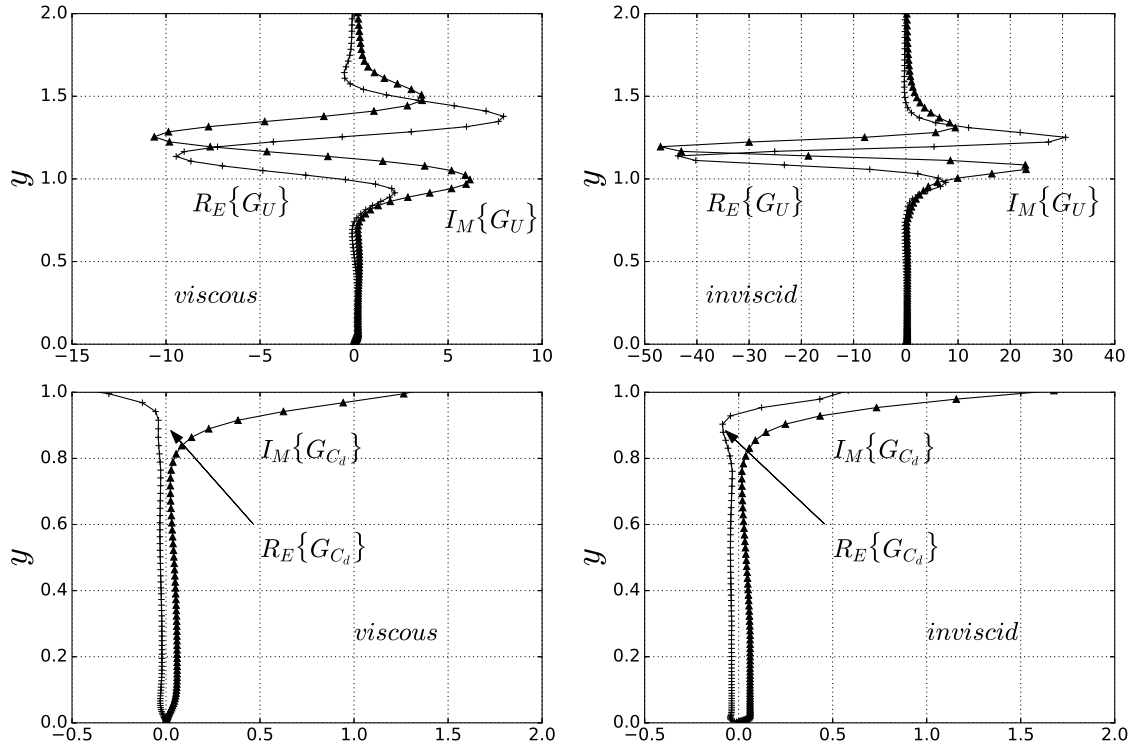


Figure 3.4: Real and imaginary parts of the sensitivities to mean flow variations (top) and to variations in the drag distribution function (bottom), for the parameters of 3.3

The infinite norm of the sensitivities for the four cases studied (G, H, I, and J) is reported in 3.5; the main result found is that $|G_U|_\infty$ grows monotonically with α (and more so in the inviscid case) whereas $|G_{C_d}|_\infty$ does not. It is consistently found that $|G_U|_\infty$ of case H is larger than that of case I, which exceeds the corresponding value of case J, in turn larger than $|G_U|_\infty$ of case G. This is not unexpected in view of the values of the mean shear $\frac{U_2 - U_1}{H}$ which are, going from H to G, equal

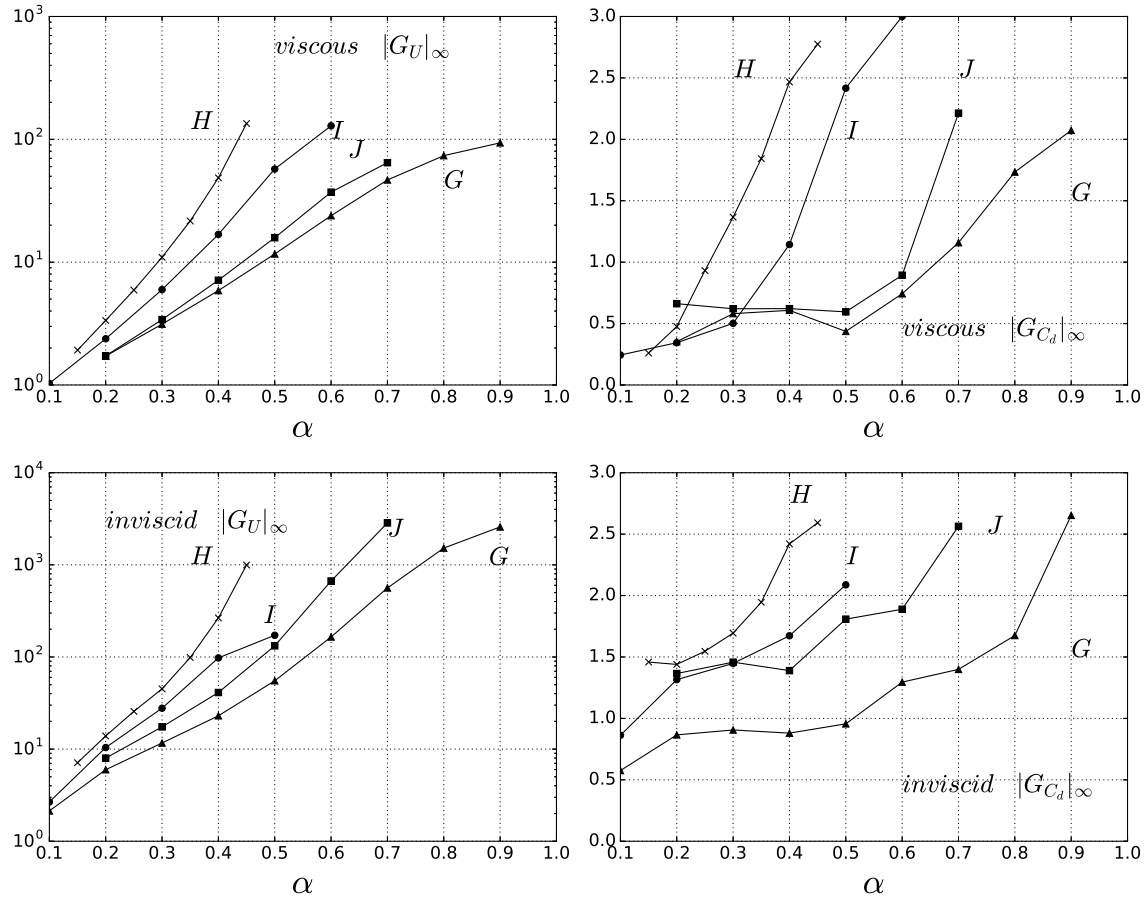


Figure 3.5: Infinite norms of the sensitivity functions for varying α

to 0.236 , 0.158 , 0.084 , and $0.071 s^{-1}$, respectively. The sensitivity of the eigenvalue ω to variations in the mean flow is generally stronger than the corresponding sensitivity to variations in the drag coefficient (aside for the long wave limit, where they are comparable). This might be interpreted positively, considering that the use of a scalar coefficient C_d to represent the drag within the canopy is but a crude approximation. An alternative model to represent the flow throughout a network of rigid, cylindrical dowels has recently been proposed by [131]. The sensitivity results for such a new model are discussed next.

3.4 AN ALTERNATIVE SENSITIVITY MODEL: ACCOUNTING FOR THE CANOPY ANISOTROPICITY

The stability problem in this section is based on the coupling between two regions, one outer region dominated by inertia and ruled by the inviscid equations and an inner one dominated by viscosity and ruled by Darcy's law, with account of the canopy geometry through a tensorial permeability, as described by [131] Normalizing the disturbance equation which couples pressure and velocity in the inner region with the same scales as previously, we obtain

$$u_i' = -Re \frac{d}{ah^2} \mathcal{K}_{ij} \frac{\partial p'}{\partial x_j}, \quad (x_1, x_2) = (x, y) \quad (3.8)$$

with \mathcal{K}_{ij} the dimensionless permeability. The effective interface between the inertial region and the slow, viscosity-dominated region does not coincide with the edge of the canopy; in fact, the rapid outer flow penetrates through the upper part of the vegetation and an effective matching between outer and inner flows must be enforced some distance δ below the canopy's edge [79]. This distance, a penetration depth, has been successfully computed by [127] for a few cases and is found to increase with the Reynolds number of the flow; for experiment G discussed below it is $\delta = 0.40$ [128]. On account of the results shown in 3.4, with the sensitivities which are negligible for $y \approx 0.60$, we expect that the exact position of the effective interface will not affect the results significantly. Using the fact that the velocity within the orthotropic porous medium is divergence free, the interface condition to be applied at $y_{itf} = 1 - \delta$ is found to be 3.9

$$v|_{itf} + B(\alpha)p|_{itf} = 0 \quad (3.9)$$

with

$$B(\alpha) = Re \frac{d}{ah^2} \sqrt{\mathcal{K}_{11} \mathcal{K}_{22}} \alpha \tanh(\theta), \quad \theta = \alpha \sqrt{\frac{\mathcal{K}_{11}}{\mathcal{K}_{22}}} y_{itf}$$

The second boundary condition that the Rayleigh stability equation must satisfy at y_∞ is simply $v = 0$. Thus, we solve only for the inviscid flow in the outer region, and the permeability of the inner domain enters the equations only through the interface condition 3.9. \mathcal{K}_{ij} is a two- by-two diagonal tensor; \mathcal{K}_{11} is the component of the dimensionless permeability along x and \mathcal{K}_{22} is the y component. For case G considered here, the packing density of the elements is $a = 0.04\text{cm}^{-1}$; it is also found that $\mathcal{K}_{11} = 0.0512$ and $\mathcal{K}_{22} = 0.0575$ [128], so that the function $B(\alpha)$ reads $B = 15.727\alpha \tanh(0.566\alpha)$.

3.4.1 The sensitivity equations

The adjoint equations in this case are the same as system 3.3, without the terms containing $1/Re$ and C_d , and the boundary conditions are

$$v^\dagger|_{itf} - B(\alpha)p^\dagger|_{itf} = 0, \quad v^\dagger|_{y_\infty} = 0 \quad (3.10)$$

The variation in the complex frequency is related to variations in the mean flow and in the permeability components through the equation

$$\delta\omega = \int_{y_{itf}}^{y_\infty} G_U(y)\delta U(y)dy + G_{\mathcal{K}_{11}}\delta\mathcal{K}_{11} + G_{\mathcal{K}_{22}}\delta\mathcal{K}_{22}$$

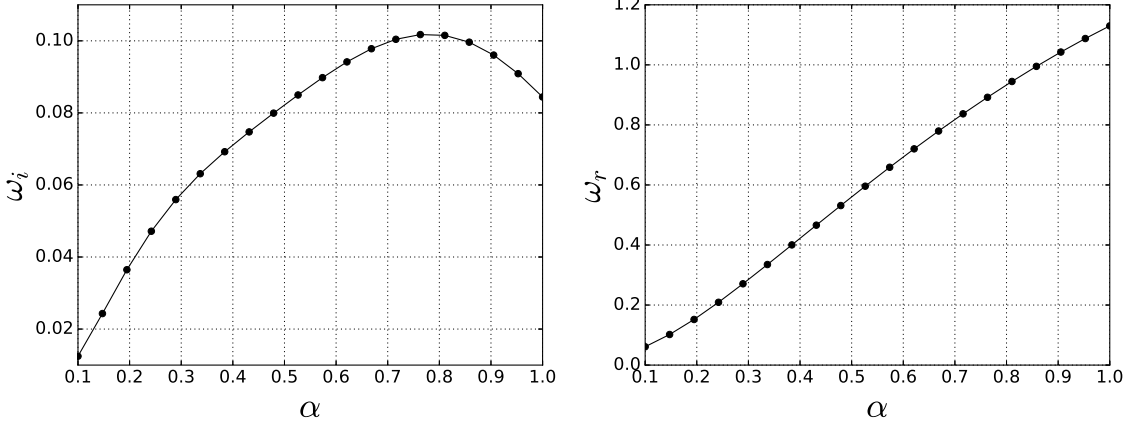


Figure 3.6: Amplification factor (left) and frequency of the most unstable mode as a function of α , for the anisotropic drag model

with

$$\begin{aligned} G_U &= \alpha \left[\overline{v^\dagger v} + \overline{u^\dagger u} \right] + i(\overline{u^\dagger v})' \\ G_{\mathcal{K}_{11}} &= -\frac{i}{2}\alpha Re \frac{d}{ah^2} \left[\overline{p^\dagger p} \right] |_{itf} \sqrt{\frac{\mathcal{K}_{22}}{\mathcal{K}_{11}}} \left\{ \tanh \theta + \frac{\theta}{\cosh^2 \theta} \right\} \\ G_{\mathcal{K}_{22}} &= -\frac{i}{2}\alpha Re \frac{d}{ah^2} \left[\overline{p^\dagger p} \right] |_{itf} \sqrt{\frac{\mathcal{K}_{11}}{\mathcal{K}_{22}}} \left\{ \tanh \theta - \frac{\theta}{\cosh^2 \theta} \right\} \end{aligned} \quad (3.11)$$

the required sensitivities, with the normalization $\int_{y_{itf}}^{y_\infty} [\overline{v^\dagger v} + \overline{u^\dagger u}] = 1$. In writing $\delta\omega$ above, we have made the assumption that the mean flow U does not vary at the two extreme points of the integration domain. The stability results (for the same parameters as in 3.2)

are displayed in 3.6. As already observed in [131], both the growth rate and the frequency are slightly larger with this model than with the isotropic resistance model, for all α 's, and the most unstable mode is found at a larger value of α (here $\alpha \approx 0.8$) in better agreement with experimental correlations [131] [103]. Also in this case the waves are found to be only weakly dispersive. Eigenfunctions are plotted in 3.7, together with the real and imaginary parts of the G_U sensitivity function. As in 3.3, the modulus of the u eigenfunction peaks near the edge of the canopy ($y = 1$), whereas the adjoint eigenfunctions have a maximum value slightly above. As a general remark, the shapes of the direct and adjoint modes are quite similar to those found with the isotropic resistance model; as reported at the end of 3.2.2, it is found that the flow is most sensitive to streamwise momentum forcing. Also, real and imaginary parts of G_U have a double-peak structure, like in the isotropic-drag model, but now the largest absolute value of G_U is

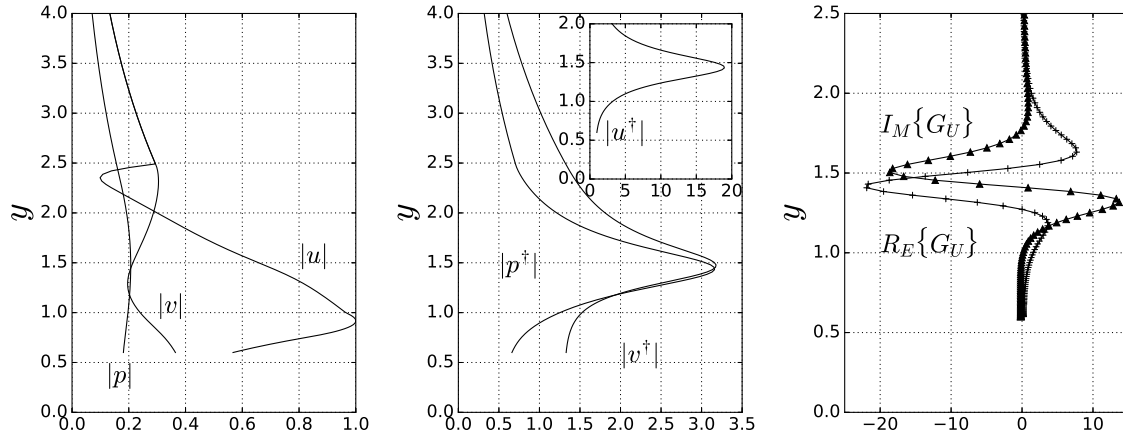


Figure 3.7: Left and center frames: moduli of direct and adjoint eigenfunctions; pressure and “adjoint pressure” are drawn with dashed lines. Right: real and imaginary parts of the sensitivity function G_U ($\alpha = 0.4790$)

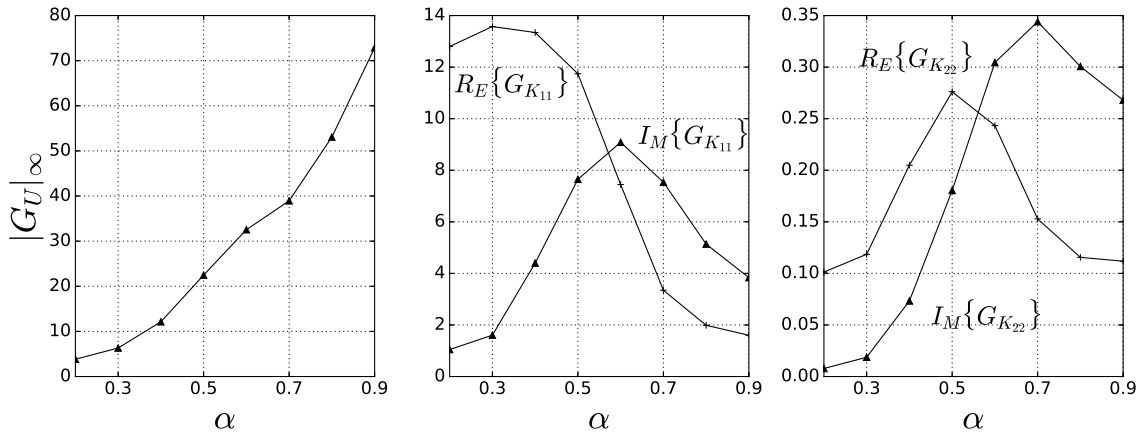


Figure 3.8: Case G. Left: infinite norm of G_U for varying α . Center and right frames: real and imaginary parts of the sensitivity coefficients to variations in the permeability components

smaller and shifted towards a larger y than in the previous inviscid case (cf.3.4, top-right frame). This can also be appreciated by the inspection of 3.8 (left); $|GU|_\infty$ still grows monotonically with α , but the sensitivity is smaller than that computed earlier (cf. 3.5) with either the viscous or inviscid model (it is actually closer to the viscous sensitivity, as an effect of the interface condition). Furthermore, it is interesting to observe that both real and imaginary parts of G_U vanish for $y = y|_{itf}$ (cf.3.7, right), and this supports the statement made previously that a small shift in the position of the effective interface has but a minor influence on the most unstable mode. The sensitivity coefficients for the two components of the permeability tensors are displayed in 3.8 (center and right frames): the present model is more effective to variations in \mathcal{K}_{11} than to \mathcal{K}_{22} as far as modifying the complex eigenfrequency. Significantly, different ranges of wavenumbers behave differently as far as the variation in ω is concerned. The frequency ω_r of long waves (around $\alpha \approx 0.3$) is more easily modified by acting on \mathcal{K}_{11} (with an almost negligible effect on the growth rate of the wave); conversely, the growth rate of modes with large values of α is affected efficiently by variations in the first component of the permeability tensor.

3.5 CONCLUDING REMARKS

We have considered two different models of the flow through a vegetated layer experiencing Kelvin-Helmholtz destabilization. One model is based on the use of a single drag coefficient to express the force exerted by the vegetation on the fluid, the second considers the canopy as an orthotropic porous medium and is based on Darcy's equation with a tensorial permeability [127]. Both models have advantages and drawbacks. The main

advantage of the first model is that the drag coefficient can be taken to vary across the canopy; whether this positive consideration, based on macroscopic experimental measurements [54] [51] [53], carries over to the stability problem remains to be established. The second model, applicable to dense porous media, considers two independent parameters to express the disturbance flow perpendicular and parallel to the rigid dowels forming the canopy. Such parameters and components of the transversely isotropic permeability tensor K_{ij} arise from the solution of a local Oseen problem [127]. The drawback of the second model is the fact that an interface (whether real or effective) appears, and adequate matching conditions must be enforced there. Despite much work since the seminal contribution by [12], a consensus on the “best” interface conditions between a pure fluid region and a porous medium has not yet emerged. The models have been put to test through a classical sensitivity analysis [20]. Beyond displaying stability results which correspond better to those to be expected from available experimental correlations [103] [131], the anisotropic model is less sensitive to variations in the base flow (with potentially larger variations in frequency and growth rate of the instability mode for the case of shorter waves). As far as a direct comparison between G_{C_d} and $G_{K_{ii}}$ is concerned, this can hardly be made since the variables represent different objects; in particular, the pressure drop through the canopy depends directly on C_d and inversely on the permeability. The present results indicate that the anisotropic model depends significantly on the value of the apparent [127] permeability component K_{11} , whose evaluation must thus be conducted carefully. This model is also of interest for further developments, in particular for the study of instabilities developing over waving canopies. Darcy’s law in this latter case would need to be modified, as described in [89] and [130].

Acknowledgment

The authors would like to thank the IDEX Foundation of the University of Toulouse for the financial support granted to the last author under the project “Attractivity Chairs.” The computations have been conducted at the CALMIP center, Grant No. P1540. The referees are gratefully acknowledged for their comments leading, in particular, to the correct interpretation of the sensitivity of the drag coefficient and to the material in Appendix A.

APPENDIX A: EFFECT OF C_d ON THE MEAN FLOW

In 3.2 of the paper it is described how the eigenvalue ω varies as an effect of independent variations of U and C_d . However, since C_d is not zero within the canopy and it is used to compute the mean flow profile U , we should in principle have expressed δU as $\delta U = \frac{dU}{dC_d} \delta C_d$ and considered a single sensitivity function $G^*_{C_d} = G_{C_d} + \frac{dU}{dC_d} G_U$, instead of the two sensitivities given in 3.6. This would have certainly been the appropriate line

of action if the mean flow equation were issued from exact equations, in which case we should have considered also the adjoint of the base flow equation in our variational problem. However, the mean flow model by [51] contains empirical approximations and parameters, and alternative models [110], [131]—including very different ones—have been used successfully in the past to predict the mean field; we have thus made the choice, in both 3.3 and 3.4, of considering the mean flow as given, and to take independent variations of U and C_d in the stability analysis to assess the effect of modifications in either variable. If we were to find how much the base flow depends on the drag coefficient in this particular problem, we would need to determine the function $U(C_d)$ and take its derivative. Since both U and C_d are functions of the space coordinate y , the implicit dependence can be found, and we have plotted it for one case on the left frame of 3.9. Clearly, the function $U = f(C_d)$ is not single-valued and therefore the derivative can be calculated only over two separate U (or, equivalently, y) intervals. We have carried out the derivation numerically over each interval, within the range $0.3 \leq y \leq 1$, and the result is reported on the right frame of 3.9. The filled triangle and circle symbols indicate the two y intervals within the canopy. We first observe that both the location where C_d is maximum and the shape of the function $U = f(C_d)$ are strongly correlated to the drag law $C_d(y)$, modeled by [51]

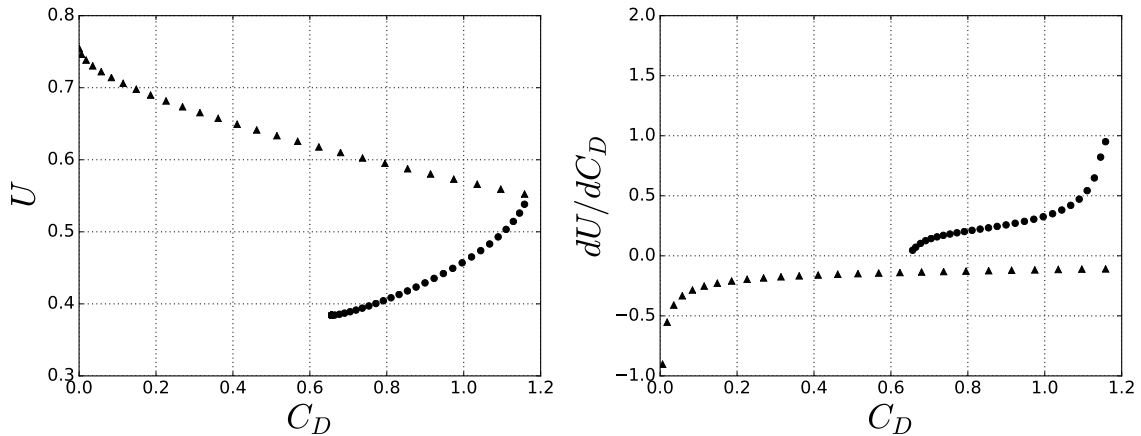


Figure 3.9: Case G. Left: mean velocity profile, U , versus the drag coefficient, C_d . Right: first derivative, dU/dC_d . The triangles denote the region $y \in [0.76, 1]$, the filled circles denote the region $y \in [0.3, 0.76]$.

through their measurement data (cf. their Figure 7 and Equation (18)). We also notice that the derivative dU/dC_d is reasonably small except locally at the point where the derivative of the function is not continuous, where it is of order 1. The discontinuity there is however artificial since the function $C_d(y)$ given in Equation (18) of [51], where C_d is divided into a parabolic and a linear part, can be easily modified to yield a continuous first derivative at $y = 0.76$ if required, still maintaining a mean flow very close to the measured

one.

APPENDIX B: A DIGRESSION ON SPATIAL STABILITY THEORY AND GROUP VELOCITY

Stability problems such as the first one considered in this paper can be approached with the spatial theory framework, with the wavenumber α complex, its imaginary part being a growth rate, and the circular frequency ω a real constant parameter. Let us generalize the sensitivity analysis by considering, as a first step, α and ω as complex numbers which can vary. Equation 3.4 contains one additional term and reads:

$$0 = \delta\langle q^\dagger, \mathcal{L}q \rangle = \langle q^\dagger, \mathcal{L}\delta q \rangle + \langle q^\dagger, \frac{\partial \mathcal{L}}{\partial U} q\delta U \rangle + \langle q^\dagger, \frac{\partial \mathcal{L}}{\partial C_d} q\delta C_d \rangle + \langle q^\dagger, \frac{\partial \mathcal{L}}{\partial \omega} q \rangle \delta \omega + \langle q^\dagger, \frac{\partial \mathcal{L}}{\partial \alpha} q \rangle \delta \alpha \quad (3.12)$$

To obtain the sensitivities in the spatial problem (for which $\delta\omega = 0$) we now have to solve an adjoint system similar to 3.3, where ω^\dagger is replaced by ω and α by α^\dagger . The variation of the wavenumber $\delta\alpha = 0$ is thus given by:

$$\delta\alpha = \delta\alpha_r + i\delta\alpha_i = \int_0^{y_\infty} G_U(y)\delta U(y)dy + \int_0^1 G_{C_d}(y)\delta C_d(y)dy$$

the functions G_U and G_{C_d} maintain the same form as in the temporal theory 3.6, with the direct and adjoint eigenfunctions which are now normalized by imposing that $N_\alpha = -1$, with

$$N_\alpha = \int_0^{y_\infty} \left[\left(U - \frac{2i\alpha}{Re} \right) (\bar{v}^\dagger v + \bar{u}^\dagger u) + \bar{p}^\dagger u + \bar{u}^\dagger p \right] dy$$

Let us now consider a problem in which U and C_d are not allowed to vary, but α and ω are. With reference to Equation 3.12, with any choice of normalization of direct and adjoint modes, it is found that $N_\omega\delta\omega = N_\alpha\delta\alpha$. Thus, once the adjoint problem is solved, it is possible to accurately compute the group velocity c_g of any stability problem using the value of N_ω and N_α , i.e.,

$$c_g := \frac{d\omega_r}{d\alpha_r} \approx \frac{\text{real}(N_\alpha)}{\text{real}(N_\omega)} \quad (3.13)$$

Note that c_g above is different from the “complex group velocity” $C_g := \frac{d\omega}{d\alpha} \approx \frac{N_\alpha}{N_\omega}$, and it is also $c_g \neq \text{real}(C_g)$. Relation 3.13 can be employed in either a spatial or temporal stability analysis and some representative results (for case G) are provided in Table I with the phase velocity $c_r := \omega_r/\alpha_r$ and the group velocity determined from Equation 3.13. The temporal or spatial amplification factors, ω_i or $-\alpha_i$, respectively, are also given for all

cases using Gaster's transformation: $\omega_i = -\alpha_i c_g$. Two types of errors on the calculation of the group velocity (noted *err*) are given in the table; the top four values, relative to the temporal theory, are defined as

$$err = \frac{|c_g|_{3.13} - c_g|_{FD}|}{c_g|_{3.13}}$$

with $c_g|_{FD}$ arising from a first-order finite difference approximation of the group velocity. The bottom four values are defined by the formula

$$err = \frac{|c_g|_{temporal} - c_g|_{spatial}|}{c_g|_{temporal}}$$

The relative difference on c_g between temporal and spatial theory is rather low. It has to be kept in mind, however, that a stability analysis in the spatial framework yields a nonlinear eigenvalue problem, with a consequent larger numerical system than in the temporal framework; therefore, by inverting matrices of the same size, the accuracy is expected to be slightly lower. The accuracy of the growth rate approximated through Gaster's relationship is also found to be acceptable.

Theory	<i>Re</i>	α_r	ω_r	$-\alpha_i$	ω_i	c_r	c_g	<i>err</i> (%)
Temporal	500	0.5	0.4778	<i>0.0248</i>	0.0254	0.9556	1.0245	0.54
	3450	0.5	0.4601	<i>0.0413</i>	0.0404	0.9202	0.9797	0.06
	10^5	0.5	0.4514	<i>0.0436</i>	0.0421	0.9028	0.9661	0.63
	10^9	0.5	0.4508	<i>0.0451</i>	0.0425	0.9016	0.9427	2.90
Spatial	500	0.4993	0.4778	0.0248	0.0250	0.9569	1.0100	1.41
	3450	0.4990	0.4601	0.0427	0.0404	0.9220	0.9471	3.30
	10^5	0.4996	0.4514	0.0449	0.0416	0.9109	0.9371	3.46
	10^9	0.4993	0.4508	0.0450	0.0411	0.9028	0.9143	3.01

Table 3.1: Temporal versus spatial stability, Case G. The model employed here is based on a modified Orr-Sommerfeld equation—rather than a system based on primitive variables as done in the bulk of the paper—which is why the temporal results have slightly larger growth rates ω_i than those displayed in Fig. 3.2; this is related to the need of computing numerically d^2U/dy^2 and dC_d/dy in the Orr-Sommerfeld-like equation. In italics, the growth rates obtained from Gaster's transformation are reported; the parameters imposed in each simulation are indicated with bold characters. The solutions for $Re = 10^9$ coincide with those found using the inviscid equations.

The amplitude of the sensitivity functions, $|G_U(y)|$ and $|G_{C_d}(y)|$, in the spatial and temporal stability frameworks is of same order of magnitude (not shown here) since they are related through temporal spatial the complex group velocity C_g . It is found that

$|G_U^{temporal}| \approx |C_g| |G_U^{spatial}|$ with $|C_g| \approx c_g \approx 1$ in the present case. Obtaining and comparing results in the temporal and spatial stability frameworks, such as in Table I, is a good means to validate the sensitivity functions and to verify the accuracy of the computations of the adjoint stability equations.

APPENDIX C: correction to compare continuous and discrete adjoint eigenfunctions

The discretization operation transform the operator \mathcal{L} into a matrix \mathbf{A} and of course do the same things to the unknown functions that becomes vectors.

continuous	discrete
\mathcal{L}	\mathbf{A}
q	\hat{q}

This has a serious and most often hidden repercussion in th approach to solve the adjoint equations.

As above stated the derivation of the adjoint equation start with the enforcing of the Lagrange identity:

$$\langle q; \mathcal{L}q \rangle = \langle \mathcal{L}^\dagger q^\dagger; q \rangle \quad (3.14)$$

where the scalar product $\langle ; \rangle$ is defined in our case as:

$$\langle a; b \rangle = \int_0^{y_\infty} \bar{a} \cdot b dy \approx \sum_{i=1}^N \sum_{j=1}^N \hat{a}_i^T w_{i,j} \hat{b}_j = \hat{a}_i^T \mathbf{M} \hat{b}_j = \langle a; b \rangle_{\mathbf{M}} \quad (3.15)$$

Is it clear from equation 3.15 that the scalar product takes two different forms in the continuous and in the discrete case. In fact in the discrete case is mandatory to introduce the quadrature rule weights $w_{i,j}$ of the chosen discretization. \mathbf{M} is the matrix representation of the weights and is symmetric and positive defined.

In order to compute and solve the adjoint equation one could proceed as follow:

- The direct problem is defined in the continuous space as $\mathcal{L}q = 0$
- Chose a discretization (FEM, FD, Chebychev polynomials...) and transform the above problem in a discrete one $\mathbf{A}\hat{q}$
- Solve it to obtain the discrete version of the eigenfunctions \hat{q}

For the adjoint problem on should at first compute the adjoint operator, this can be done using the Lagrangian identity at a continuous level:

$$\begin{aligned} \langle q; \mathcal{L}q \rangle &= \langle \mathcal{L}^\dagger q^\dagger; q \rangle \\ \Rightarrow \int_0^{y_\infty} \overline{q^\dagger} \mathcal{L}q dy &= \int_0^{y_\infty} \overline{\mathcal{L}^\dagger q^\dagger} q dy \end{aligned} \quad (3.16)$$

From the last equation starting from the left part is it possible after some manipulation to retrieve the form on the right part and so find the formulation of the adjoint operator.

It is important to pinpoint that in the above equation the scalar product $\langle a; b \rangle$ is enforced at a continuous level.

And now to solve the adjoint system the procedure 3.5 can be used changing the direct system with the adjoint one. The above way of computing the adjoint and solve the system is called **continuous approach**.

To summarize this approach one can straight forward solve the direct problem computationally, mathematically find the adjoint operator using the continuous scalar product and the Lagrange identity and then discretize the adjoint problem and solve it computationally. This is why the **continuous approach** is sometimes known as derive than discretize. And the stability and accuracy problems derive directly from the fact that we discretize the problem two times (the direct first and than the adjoint).

On the contrary in the **discrete approach** the scalar product 3.15 is enforced at the discrete level in order to use the already discretized direct equation to retrive the adjoint system at a discrete level, to limit the computational errors.

$$\begin{aligned} \langle q^\dagger; \mathcal{L}q \rangle &= \langle \mathcal{L}^\dagger q^\dagger; q \rangle \\ \Rightarrow \overline{\hat{q}^\dagger}^T \mathbf{M} \mathbf{A} \hat{q} &= (\overline{\mathbf{A}^\dagger \hat{q}^\dagger})^T \mathbf{M} \hat{q} \\ \Rightarrow \mathbf{M} \mathbf{A} &= \overline{\mathbf{A}^\dagger}^T \mathbf{M} \\ \Rightarrow \mathbf{A}^\dagger &= \mathbf{M}^{-1} \overline{\mathbf{A}}^T \mathbf{M} \end{aligned} \quad (3.17)$$

Chapter 4

Effect of geometrical parameters and inertia on the apparent permeability tensor in fibrous porous media

It is far better to foresee even without certainty than not to foresee at all.

- The Foundations of Science, *Henri Poincare*

4.1 Introduction

The flow through porous media is a problem of importance for several natural and technological applications. Since Darcy's original formulation [36], which relates the flow rate through a porous bed to the pressure drop across the bed's sides, many corrections have been made to account, for example, for viscous effects [23] or for the consequences of inertia [47]. All of the cited works are of empirical nature, but homogenisation has been able to recover all of these formulations rigorously starting from the Navier-Stokes equations [124]. This latter approach is sometimes defined VANS, for Volume-Averaged Navier-Stokes.

The theory requires the knowledge of a number of terms, most notably, in the case of an isotropic porous bed, a permeability coefficient and a Forchheimer coefficient. Initial efforts in defining these terms were based on a combination of physical reasoning and measurements, leading to expressions known as the Kozeny-Carman [75, 31] and the Ergun [43] correlations. The first provides the permeability for the laminar flow of a single-phase fluid through a packed bed of sand grains, as function of the porosity and the diameter of the grains, while the second extends Darcy's law to let the pressure drop depend on two terms, one proportional to the velocity and the second to its square, thus accounting for inertia.

These approaches do not consider microstructural or geometrical features of the porous bed, which can render the permeability a tensorial quantity, and are often restricted to simple unidirectional flows. In the present work we are concerned with a transversely isotropic material composed by parallel fibers of circular cross-section, with one axis of symmetry, (O, x_3) ; in such materials the permeability is a diagonal tensor with the component in the direction parallel to the fibers greater than those along the transverse axes. For such an arrangement we will investigate the effects of both the direction of the forcing pressure gradient and inertia. When the latter effect is present, embodied by a Reynolds number Re_d , based on mean velocity through the medium and fibers' diameter, exceeding an order one threshold, the permeability is no more simply defined upon geometrical properties. This new permeability, which arises from a well-defined closure problem, is then called *apparent permeability*.

The influence of the geometry of the solid inclusions has been addressed previously by Yazdchi et al. [125] for arrays of cylinders in both square and hexagonal (or staggered) patterns, with the cylinders' section which can vary in shape. The results, in the two-dimensional and low Reynolds number limits, demonstrate the dependence of the permeability component along the flow direction to both the porosity and the direction of the macroscopic pressure gradient. The direction of the pressure gradient is found to have a weak effect for beds of medium-high porosity ($\varepsilon > 0.7$) and a stronger dependence appears upon the geometry of the solid inclusions.

The influence of the Reynolds number on the permeability and on the Forchheimer correction has been presented in a number of papers. One of the contributions most relevant here is due to Edwards et al. [42]. These authors show that, for arrays of fibers, the apparent permeability decreases with the increase of the Reynolds number, and the rate of this decrease depends on the geometry of the array; also, the Reynolds number is found to have a stronger influence on the apparent permeability when the medium is highly porous. The results of the work by Edwards et al. [42] agree with those by Zampogna and Bottaro [126] and with our own work (as shown later), all for the case of cylindrical fibers, although some issues remain on the persistence of steady solutions in the simulations by Edwards et al. [42] in cases for which a limit cycle should have set in. A fully three-dimensional porous medium, more complex than those discussed so far, has been considered by Soulaine and Quintard [113], confirming the decreasing trend of the apparent permeability with the Reynolds number.

Another contribution which deserves mention is that by Lasseux et al. [78]; they have computed the permeability tensor for various Reynolds numbers, in a two-dimensional geometry with cylinders of square cross-section. Forcing the flow along the main symmetric directions of the fiber, Lasseux et al. [78] have identified different regimes:

- a creeping flow regime for $0 < Re_d < 10^{-3}$, without Forchheimer terms;
- a weak inertia regime for $10^{-3} < Re_d < 1$, with the Forchheimer correction quadratic in Re_d ;

- a strong inertia regime for $1 < Re_d < 10$, where the Forchheimer correction is linear with the Reynolds number;
- a turbulent regime, for $Re_d > 10$, with the Forchheimer correction again quadratic with the Reynolds number.

The boundaries between the different regimes are specific to the geometrical arrangements and to the porosities being considered; a step forward in rendering (some of) these boundaries rigorous and independent of the arrangement of the pores, through the definition of a Reynolds number which accounts for a "topological" coefficient, has been recently made by Pauthenet et al. [98]. For the purposes of the present paper, we must retain that Lasseux et al. [78] have parametrized the Forchheimer correction with the Reynolds number, and have found that the inertial correction is orders of magnitude smaller than the Darcy's term, at least before the turbulent regime sets in. Moreover, Lasseux et al. [78] have studied how a Forchheimer tensor, \mathbf{F} , depends upon the direction of the macroscopic forcing term with respect to the orientation of the square cross-section of the fibers, for Re_d up to 30. It is concluded that a deviation angle, γ , exists between the direction of the pressure gradient and that of the mean flow, because of the fibers' geometry. Finally, the inertial correction is strongly influenced by the orientation of the driving pressure gradient, and the tensor \mathbf{F} is not symmetric (in fact the off-diagonal components are found to be inversely proportional to the diagonal terms, and symmetric with respect to rotations about the diagonal axis of the square, i.e. the direction at 45° in the $x_1 - x_2$ plane).

The effect of variations in the forcing angle, with restrictions to angles in the $x_1 - x_2$ plane, is also examined by Soulaine and Quintard [113] with conclusions in qualitative agreement with those of both the contribution just cited and our results described further below. In all cases, the off-diagonal components of the apparent permeability tensor are small and the diagonal components display but a small variation upon rotation of the driving pressure gradient.

As already anticipated, this work investigates how the direction of the macroscopic pressure gradient, the porosity and the Reynolds number can modify the Darcy and Forchheimer closures arising from a VANS model of a fibrous porous medium. We will consider a three-dimensional unit cell for the microscopic model (such a unit cell is sometimes denoted REV, for Representative Elementary Volume), with a generic forcing whose direction is defined by two Euler angles. Given the formidable space of parameters, some representative results are first shown and discussed. Response surfaces in the space of parameters are then identified by the use of a metamodel based on kriging interpolation. For the sake of space, only the first diagonal component of the apparent permeability tensor is discussed in detail in the paper; however, all components have been computed. They represent an extremely useful data base which we are now in the process of using in macroscopic simulations of flows through bundles of fibers of varying orientation and density.

4.2 The Volume-Averaged Navier-Stokes (VANS) method

4.3 Validation and setup

In this section the numerical methodology, the parameters, the setup and the validation for some reference cases are given.

4.3.1 Computational domain

The geometry used for the base REV is shown in figure 4.1: a cylindrical inclusion is present at the centre of the REV and four quarters of cylinders are situated at the corners. The lateral length of the cubic envelop is ℓ , which is used as length scale for the microscopic problem; the diameter d of the cylinders is adapted as a function of the desired porosity ε , ratio between the fluid volume over the total REV volume (ℓ^3).

The forcing term \mathbf{f} of the DNS is a vector whose direction is defined by two Euler angles, with rotations of the form: $\theta \mathbf{e}_3 + \phi \mathbf{e}_2^I$ (cf. figure 4.1). Its amplitude is set a priori and is connected to the Reynolds number, Re_d , defined with the mean velocity over the REV and the fiber diameter, d . Re_d is a result of the calculations, once the mean velocity is evaluated.

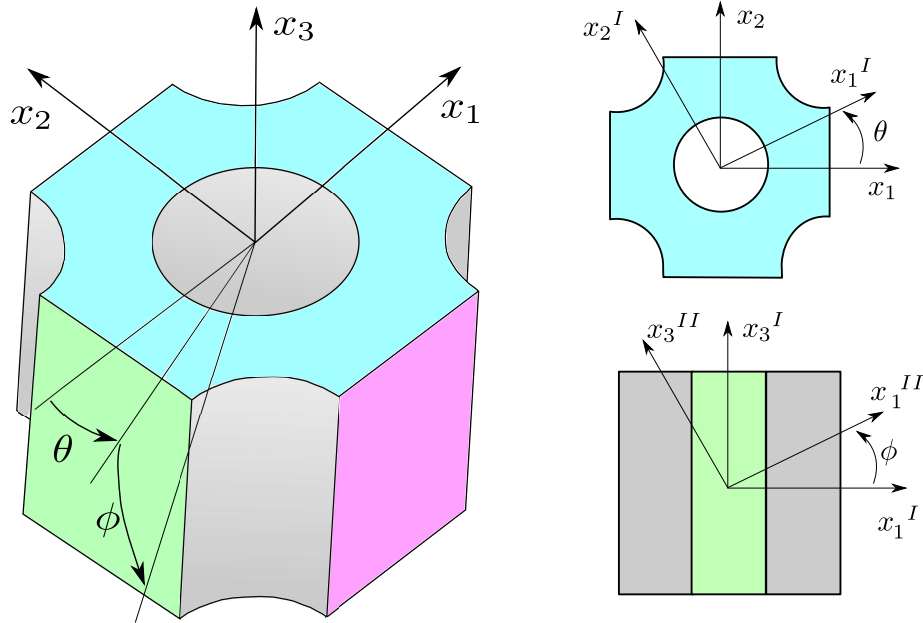


Figure 4.1: REV for the fiber geometry investigated.

4.3.2 Numerical setup

The simulations have been carried out with the open-source code OpenFOAM [119], based on a finite volume discretization with a colocated arrangement for the unknowns. The standard solver `icoFoam` (incompressible Navier-Stokes) has been modified in order to include a constant pressure gradient acting as a forcing term \mathbf{f} in equation (2.16). The coupling between the velocity and the pressure equations is based on the pressure implicit split operator referred to as the PISO algorithm. The time derivative term is discretized using the second order backward Euler scheme and all the spatial terms use a second-order central difference stencil based on Gauss finite volume approach. The velocity system is solved with a preconditioned bi-conjugate gradient (PBiCG) iterative solver with the tolerance on the velocity residuals set to 10^{-8} , associated to a diagonal incomplete lower upper preconditioner (DILU). The pressure equation is solved with a geometric-algebraic multigrid (GAMG) algorithm associated to a Gauss-Seidel smoother and the tolerance on the pressure residuals is here equal to 10^{-6} . Cyclic boundary conditions are applied to all fields on all fluid boundaries along the three directions, and the no-slip condition is imposed on the surface of the solid inclusions. The time step Δt is automatically determined to ensure that the maximum Courant number, Co , respects the condition: $Co = \|v_\beta\| \Delta t / \Delta x < 1/2$, in which $\|v_\beta\|$ is the local velocity magnitude in the REV and Δx is the local grid spacing. Co is basically the ratio between the fluid speed and the velocity to propagate information through the mesh and the condition $Co < 1/2$ is found to be sufficient to have a stable solver.

4.3.3 Mesh convergence analysis

The mesh has been computed using the internal OpenFOAM mesher named *snappy-HexMesh*. The final grid is mainly composed by hexahedral cells with a refined regular grid in the boundary layer regions next to the solid surfaces. Three different mesh sizes, with 0.65×10^6 , 10^6 and 1.5×10^6 elements, have been tested in order to demonstrate spatial convergence. This has been assessed using the Grid Convergence Index (*GCI*) introduced by Roache [105].

Details of the coarsest mesh used are shown in figure 4.2. On the right frame a close up of the grid in the neighbourhood of the fiber's boundary is displayed: twenty points are used in the structured portion of the mesh along the wall-normal direction.

The GCI method is based upon a grid refinement error estimator derived from the theory of generalized Richardson extrapolation. It measures the ratio between the computed value of a quantity over the asymptotic numerical value, thus indicating how far the solution is from the asymptotic ("exact") value. The procedure is simple and provides a method to estimate the order of the spatial convergence, based on two or three different grid sizes. First of all, the grids must be generated with the same algorithm and they must have the same final quality. In each simulation a physical scalar quantity representative of

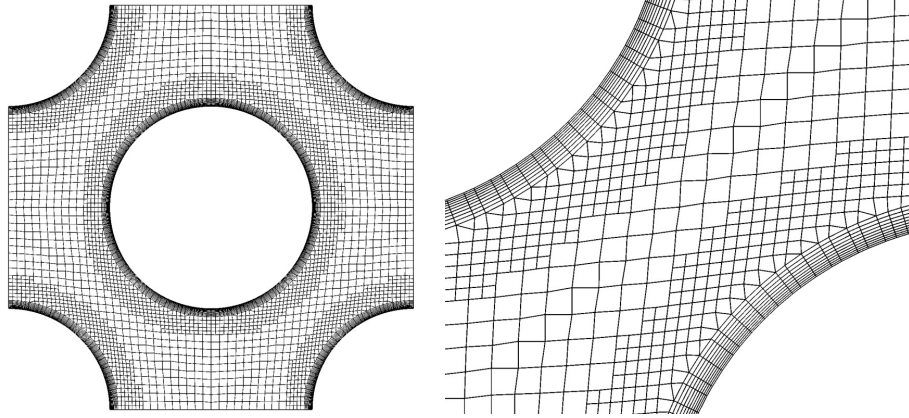


Figure 4.2: Mesh used for the computation; top view (left) and zoom in the boundary layer region (right). $\varepsilon = 0.6$.

the physical phenomenon must be sampled. The method follows the following four steps:

1. Estimate the order of convergence of the procedure, defined as $p = \ln \left(\frac{f_3 - f_2}{f_2 - f_1} \right) / \ln r$, where r is the grid refinement ratio between each grid (it is computed as the ratio between the number of elements of two consecutive grids; the approach imposes that r should remain constant between any couple of consecutive grids and be larger than 1.1), and f_i represents the quantity of interest in each grid (1=coarse, 2=medium and 3=fine).
2. Compute the relative error between grid i and j : $|\epsilon|_{ij} = \frac{f_j - f_i}{f_i}$, for $(i, j) \in \{(1, 2), (2, 3)\}$.
3. Compute $GCI_{ij} = \frac{F_s |\epsilon|_{ij}}{r^p - 1}$, with F_s a safety factor equal to 1.25 if the grids are three, and equal to 3 if the grids are only two [105].
4. Check whether each grid level yields a solution that is in the asymptotic range of convergence; this means that the quotient $AC = \frac{GCI_{23}}{GCI_{12}} \frac{1}{r^p}$ should be as close as possible to one.

In our case the quantity of interest chosen is the intrinsic average velocity inside the porous medium, and the results are summarized in table 4.1. From the table it can be seen that the intrinsic velocity difference is very small from one grid to the next and the coarse grid provides results close to the expected asymptotic value. This is taken as a sufficiently convincing argument to carry out all the computations in the following with a grid density equal to that of grid 1.

mesh index	mesh identifier	average velocity REV	metric	value
3	fine	1.11	GCI_{23}	0.366%
2	medium	1.07	GCI_{12}	1.11%
1	coarse	1.09	AC	1.006

Table 4.1: Convergence analysis. Left: average velocity within the REV, normalized with $\frac{K_{11}}{\nu_\beta} \|\mathbf{f}\|$. Right: grid convergence metrics. The REV has $\varepsilon = 0.6$, the motion is along x_1 , i.e. $\theta = \phi = 0$ and $Re_d \rightarrow 0$.

4.3.4 Validation on two different configurations

The results published in the literature by Zampogna and Bottaro [126] and Yazdchi et al. [125] are now used to validate both the methodology and our choices of the computational parameters. In the cited papers, three-dimensional computations of the permeability components in different cells geometries are presented.

Figure 4.3 displays the comparison for a cell with a square arrangements of the fibers; here the permeability is evaluated along the two principal directions, x_1 and x_3 . A good agreement is found with the published results. Figure 4.4 shows a similar comparison for a staggered arrangement of the inclusions in the unit cell. In this case the section of the cell is rectangular. The agreement for the only permeability component available in the literature is again satisfactory.

Finally, to check the correct implementation of the closure model (??) it is important to verify the equality (??) between the amplitude F^M of the macroscopic force and its microscopic counterpart obtained through an integration of the DNS fields over the solid boundaries of the inclusions in the REV. Figure 4.5 shows a plot of the relative error between these two forces, i.e. $\frac{\|F^M - F^m\|}{\|F^m\|}$, as function of the Reynolds number. We consider the successful comparison displayed in figure 4.5 as the conclusive demonstration of the validity of the approach described here. We have nonetheless carried out the same verification displayed in figure 4.5 for each one of the simulations described in the following, to our satisfaction.

4.3.5 Tests with larger REV's

Since the Reference Elementary Volume (REV) is the unit cell within the porous medium over which average quantities of the VANS are computed, it is important to choose its dimensions appropriately in the inertial regime for, if the REV is too small, it might be easy to miss crucial features of the wakes. For example, to predict the critical Reynolds number, Re_c , of the first Hopf bifurcation, a REV containing at least three solid inclusions

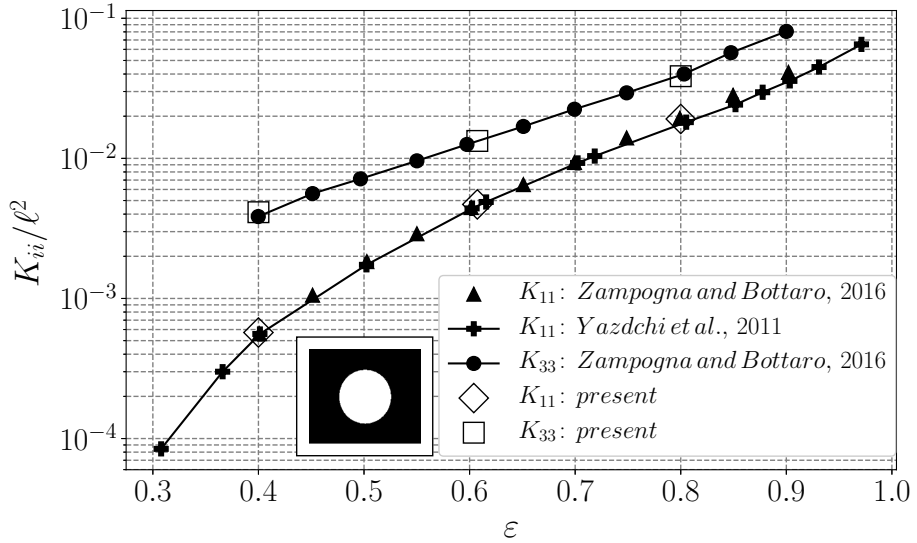


Figure 4.3: Permeability versus porosity for a square arrangement of cylinders. The scaling of the permeability is ℓ^2 and is explicitly indicated in the vertical axis.

in the direction of the mean pressure gradient is necessary in the simulations by Agnaou et al. [3]. Among the results reported, it is found that, for a fixed REV size, the error committed in the evaluation of the critical Reynolds number increases with the porosity. This same error is considerably reduced when the mean pressure gradient angle is $\theta = 45^\circ$. Thus, the choice of the number of inclusions in a REV is a task not to be overlooked, and the final choice must account for the porosity, the direction of the pressure gradient and the microscopic Reynolds number.

Here, the influence of the numbers of inclusions present in a REV is assessed by focussing only on the velocity components after averaging over the REV. The unit cubic cell of side ℓ is used as reference: starting from this, two additional REV's are built, as shown in figure 4.6. The first one is doubled in both the x_1 and x_2 directions and the case tested numerically is characterised by $\theta = 0$, $\phi = 0$ (i.e. the forcing pressure gradient is directed along x_1), porosity $\varepsilon = 0.6$ and $Re_d = 50$. The second REV configuration is a composition of 3 reference REVs on top of one another along x_3 , with the parameters set to $\theta = 45^\circ$, $\phi = 45^\circ$, $\varepsilon = 0.6$ and $Re_d = 100$.

For both these test cases, no appreciable differences, neither in the mean velocity nor in the forces on the fibers, have been observed, with relative errors on the mean velocity with respect to the reference case which remain below 2%. We take this as sufficient evidence to use, in the following, only the reference cubic REV of side equal to ℓ , with the understanding that only configurations with Re_d up to around 100 can be considered.

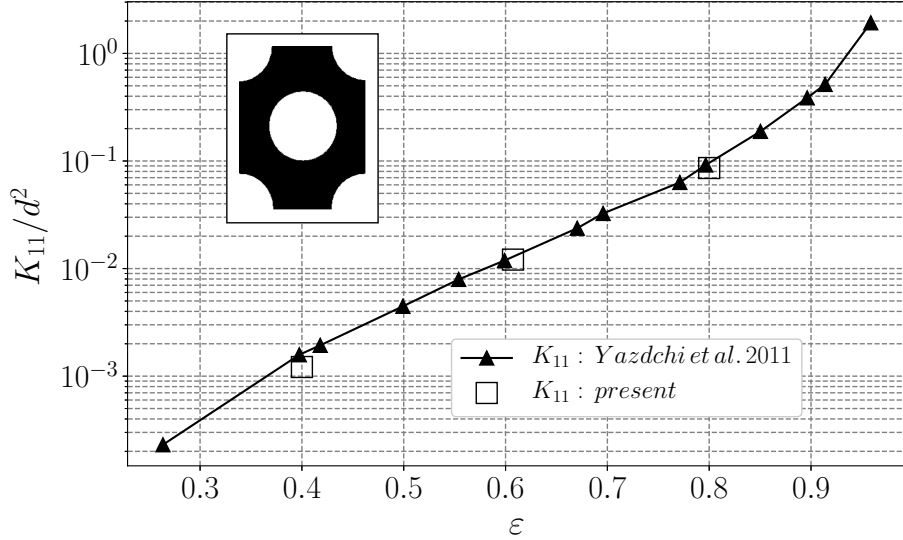


Figure 4.4: Permeability versus porosity for a staggered arrangement of cylinders. The permeability component is here scaled with d^2 (and not ℓ^2), with d the diameter of the inclusions.

4.4 Microscopic solutions

In this section, some local microscopic fields computed with direct numerical simulations are shown, together with components of the intermediate tensor \mathbf{M} coming from the numerical solution of the closure equations (??).

In figure 4.7 (top row) the local x_1 velocity component is drawn for the two-dimensional flow when $\varepsilon = 0.6$, for three Reynolds numbers, to cover the transition from the Stokes to the inertial regime. In all plots, the velocities are rendered non-dimensional by the corresponding value of $\frac{K_{11}}{\nu_\beta} \|\mathbf{f}\|$. When inertia is absent, the flow has a central symmetry; by increasing the Reynolds number, only the symmetry with respect to the x_1 axis is maintained (x_1 is the direction of the forcing pressure gradient), with the wake's length which increases with Re_d . When Re_d is of order 100 the wake spreads to the downstream boundary of the REV, re-entering, because of periodicity, at the upstream side. This Re_d represents the upper limit of validity for the cubic unit cell of side ℓ ; larger values of Re_d could only be investigated with longer/larger/thicker REV's.

The non-dimensional local M_{11} fields for the same parameters are displayed in figure 4.7 (mid row). All values in the figures arise from scaling \mathbf{M} with ℓ^2 . Visually, these local fields are strongly correlated to the local streamwise velocity component in the whole Re_d range. This is not unexpected since the local velocity drives the convective term of system

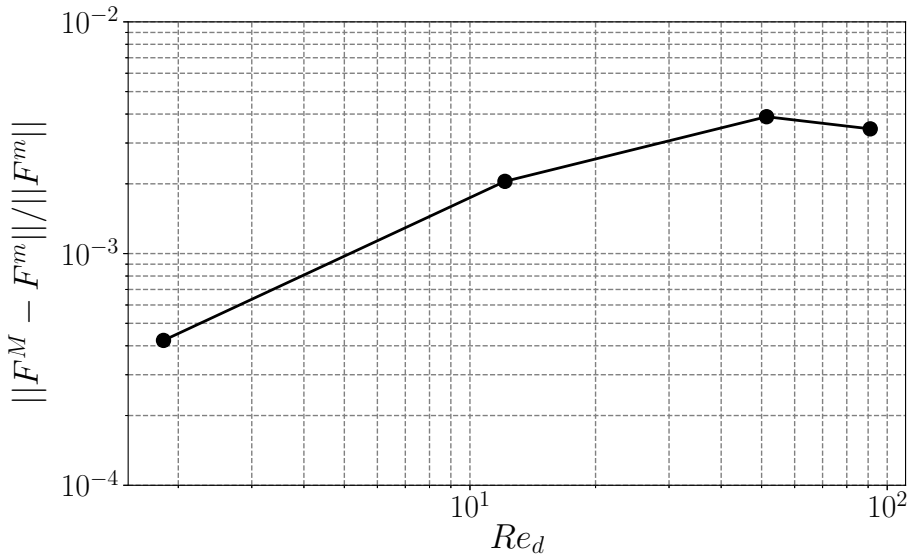


Figure 4.5: Relative error between the microscopically computed forces along the x_1 direction and those arising from the Darcy-Forcheimber model; $\varepsilon = 0.8$ for the REV in the staggered arrangement of Yazdchi et al. [125].

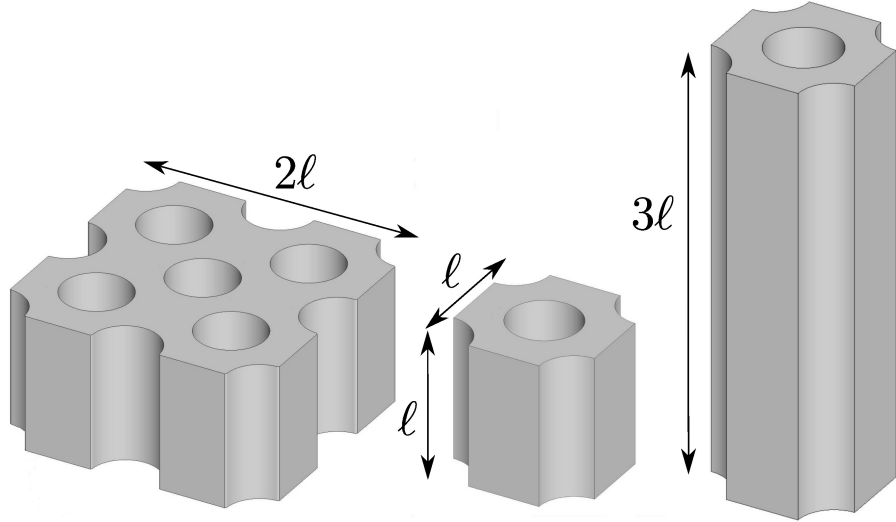


Figure 4.6: REV configurations. Left: $2 \times 2 \times 1$ arrangement; centre: $1 \times 1 \times 1$ arrangement (reference); right $1 \times 1 \times 3$ arrangement.

(??). The central symmetry of all components of \mathbf{M} in the Stokes regime is coupled to the

rotational invariance of the apparent permeability tensor in two-dimensional flows.

The effect of varying the porosity is shown in figure 4.7 (bottom row) where ε is taken equal to 0.4. Even at such a low porosity the stretching of the wake can be noticed, and it increases with Re_d . Interestingly, this effect is milder when the forcing is inclined by an angle ϕ , since the tighter packing of the inclusions causes a strong deviation of the mean flow along the axis of the fiber. In this case, M_{11} and M_{22} behave very similarly to the case $\phi = 90^\circ$.

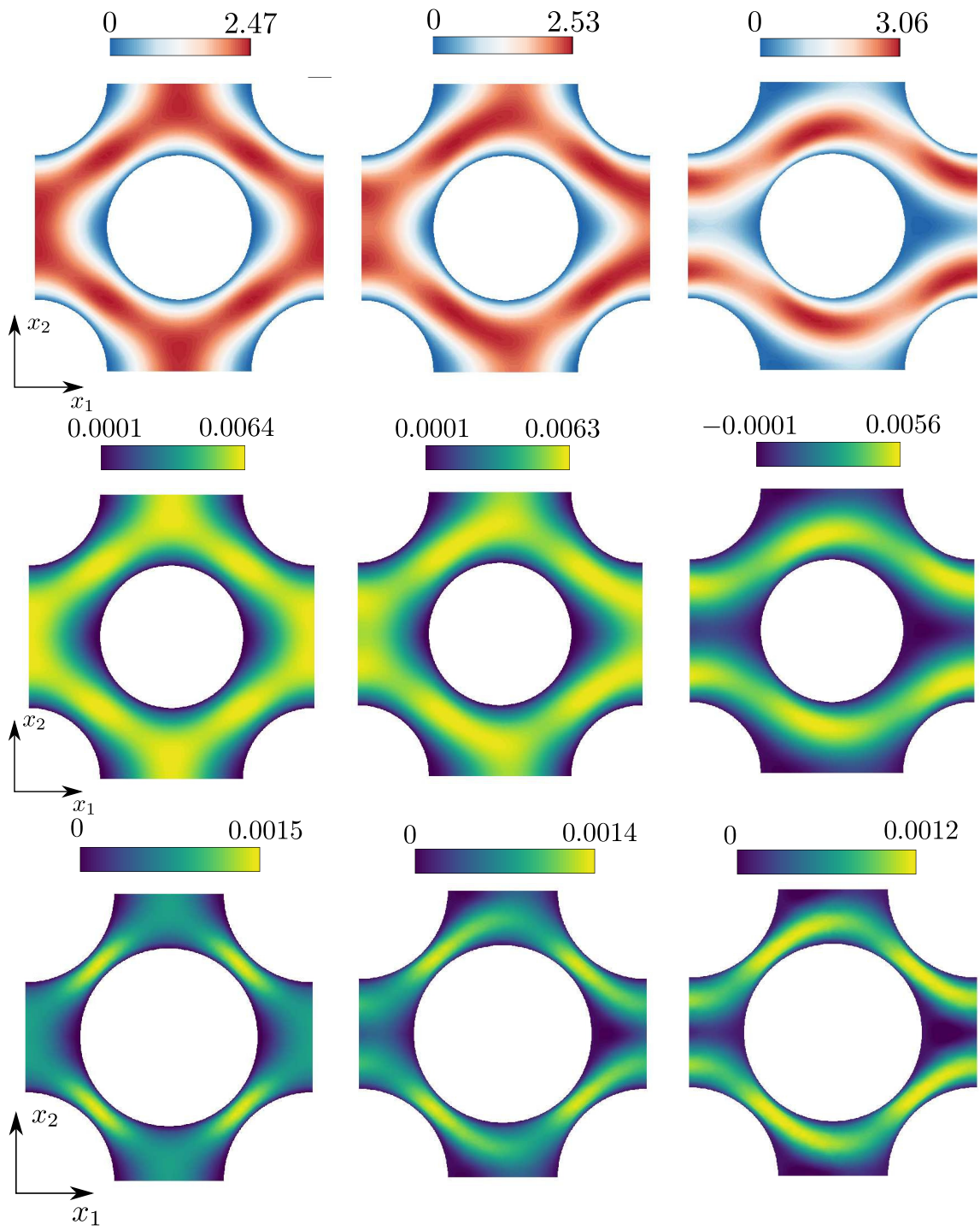


Figure 4.7: Top row: plane view of the dimensionless x_1 component of the local velocity field \mathbf{v}_β for the case $\theta = 0$, $\phi = 0$, $\varepsilon = 0.6$ and for three Reynolds numbers $Re_d = 0, 10, 50$, from left to right. Mid row: microscopic M_{17} fields corresponding to the images in the top row. Bottom row: M_{11} fields for the same Euler angles and Reynolds number as in the top two rows, and smaller porosity ($\varepsilon = 0.4$).

Another interesting point emerges by inspection of figure 4.8 where two off-diagonal components of \mathbf{M} are shown for two porosity values; the first image (left frame) represents a plane flow in the Stokes regime while the second is the plane cut of a three-dimensional solution in the inertial regime. Positive and negative values of the microscopic fields can be seen in both images but, once averaging is applied over the REV, the resulting permeability component is very close to zero (in fact, exactly equal to zero in the Stokes case). This same features occurs for all off-diagonal terms in all cases examined, so that, within the current range of Reynolds numbers, the apparent permeability tensor is, to a good approximation, diagonal¹.

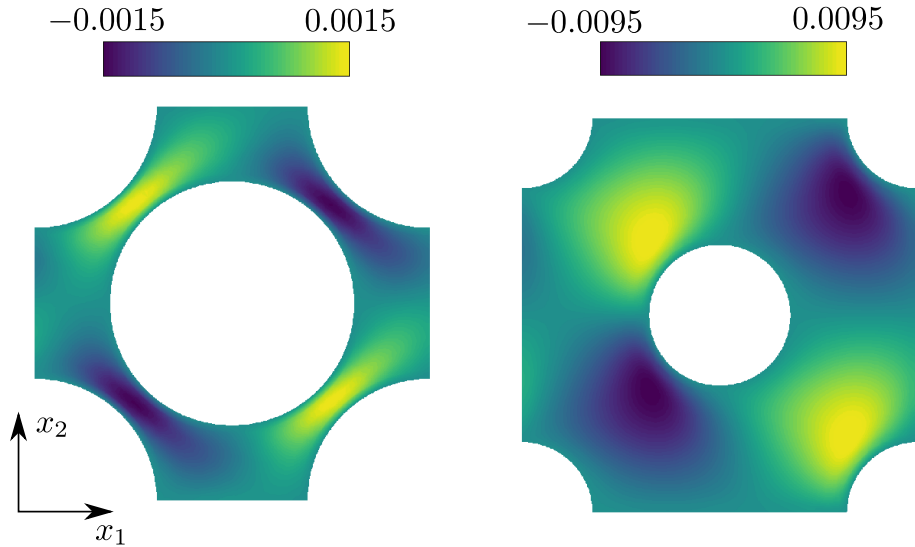


Figure 4.8: right: Non-dimensional M_{21} field for $\theta = 0, \phi = 0, Re_d = 10, \varepsilon = 0.8$, left: Non-dimensional M_{12} field for $\theta = 22.5^\circ, \phi = 45^\circ, Re_d = 50, \varepsilon = 0.4$.

A three-dimensional case is shown in figure 4.9, where all the non-zero terms of the \mathbf{M} tensor are plotted for a porous structure with $\varepsilon = 0.6$. The components shown are $M_{11}, M_{22}, M_{33}, M_{12}$ and M_{21} , while M_{i3} and M_{3j} are not plotted because they are identically zero to machine accuracy. Distinct features are visible in each image; in particular, in the last frame the M_{33} microscopic component displays a low wavelength structure along the cylinder's axis. Increasing the dimensions of the REV along x_3 does not alter such a structure, i.e. the ℓ^3 domain chosen with its periodic boundary conditions does not filter out significant high wave-numbers of the flow. We further note that the tensor \mathbf{M} is not symmetric in this case since each off-diagonal component represents the solution of the

¹In fact, there are always at least two orders of magnitude differences between the diagonal and the off-diagonal components. While the latter should not, in principle, be ignored, we will focus attention here only on the dominant terms of the permeability tensor.

closure problem in a specific direction (first index of the field) and the forcing term acts orthogonally to it (second index of the field). Once averaged over the REV it is found that both H_{12} and H_{21} are very close to zero.

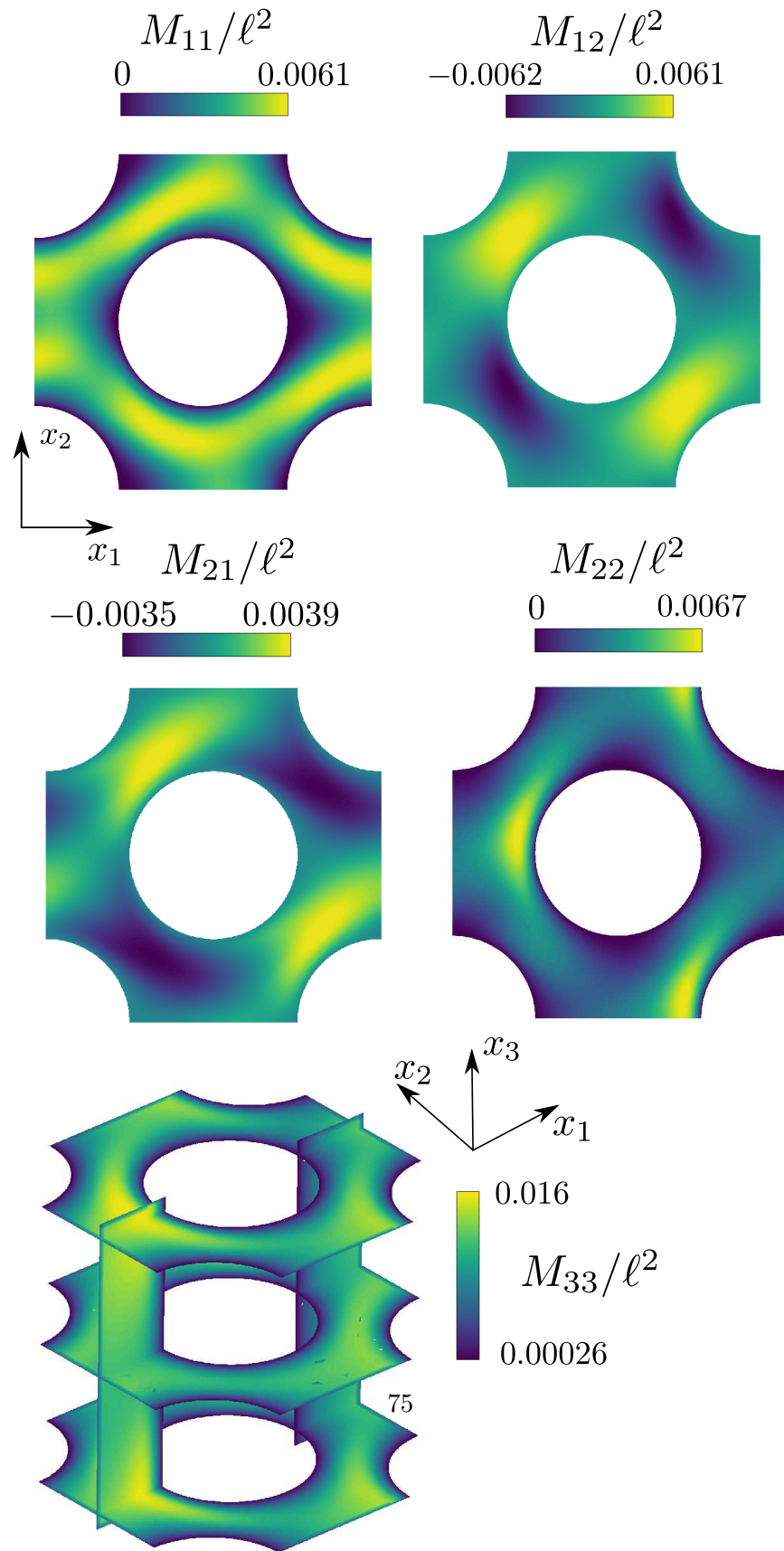


Figure 4.9: Non-dimensional \mathbf{M} components fields for the case $\theta = 22.5^\circ, \phi = 45^\circ, Re_d = 50, \varepsilon = 0.6$.

index	θ	ϕ	field properties
1	0°	0°	2D symmetric
2	22.5°	0°	2D non-symmetric
3	0°	45°	3D symmetric
4	22.5°	45°	3D non-symmetric
5	–	90°	3D symmetric

Table 4.2: Directions of the forcing tested and property of the solutions.

4.5 The apparent permeability tensor

In this section the variations of the diagonal components of the permeability tensor \mathbf{H} are discussed as function of the direction of the mean forcing, the Reynolds number and the porosity. As stated previously, the Reynolds number ranges from 0 to approximately 100 in order to capture phenomena associated with inertia; the cases considered never lead to unsteady signals. The porosity parameter ε is set to either 0.4 (low porosity), 0.6 (medium) or 0.8 (high). The forcing direction is defined by the Euler angles and all the configurations considered in this section are summarized in table 4.2; the choice has been made to explore a reasonably large range of parameters, with both two-dimensional and three-dimensional flows characterized by symmetric and asymmetric patterns.

Let us briefly recall the methodology. First, a DNS is carried out to compute the microscopic flow. Then the closure problem is solved for the tensor \mathbf{M} . Finally, each component of the apparent permeability \mathbf{H} is obtained by averaging (equation (2.1)). The results are collected in figures 4.10, 4.11 and 4.12, showing the variation of the diagonal components of \mathbf{H} .

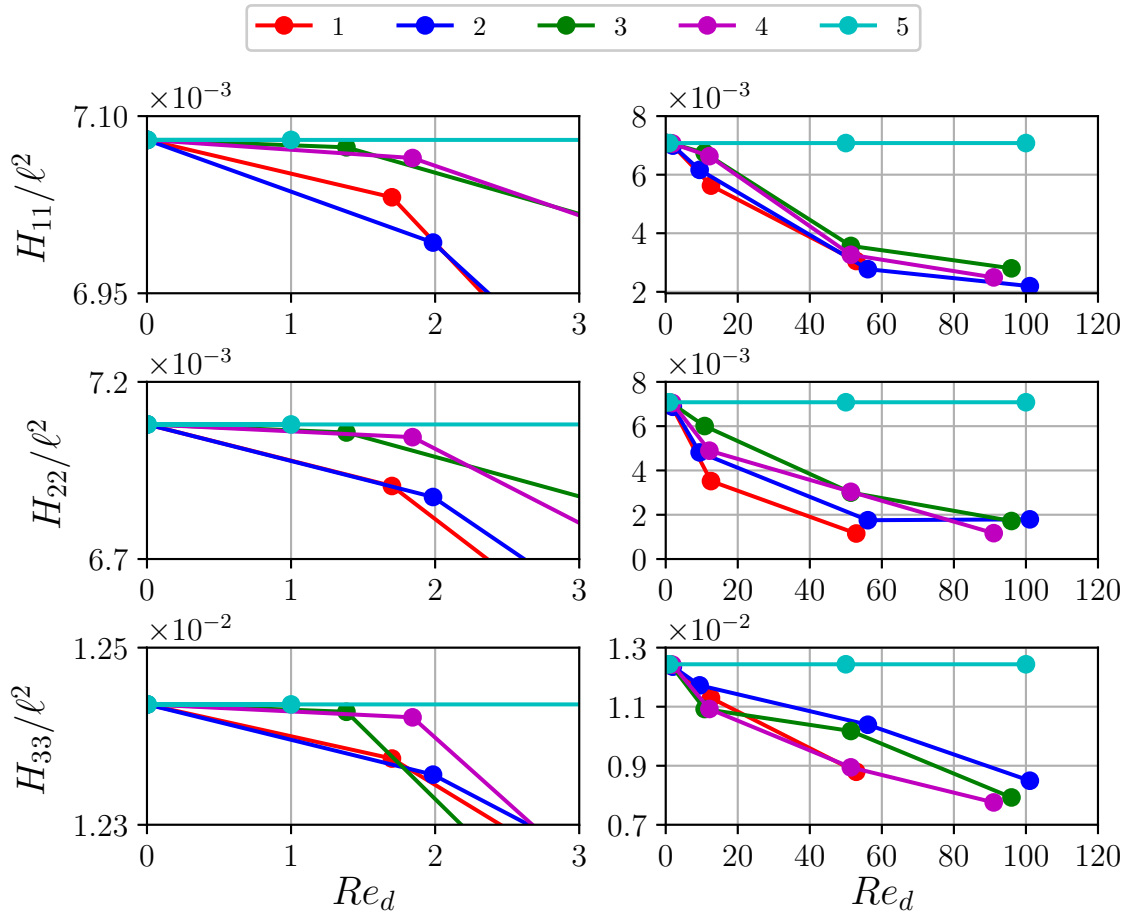


Figure 4.10: Diagonal elements of the apparent permeability \mathbf{H} as function of the Reynolds number for porosity $\varepsilon = 0.8$. The forcing direction is represented through the couple of Euler angles (θ, ϕ) (cf. table 4.2 for the case index). Left column: low- Re_d regime; right column: inertial regime.

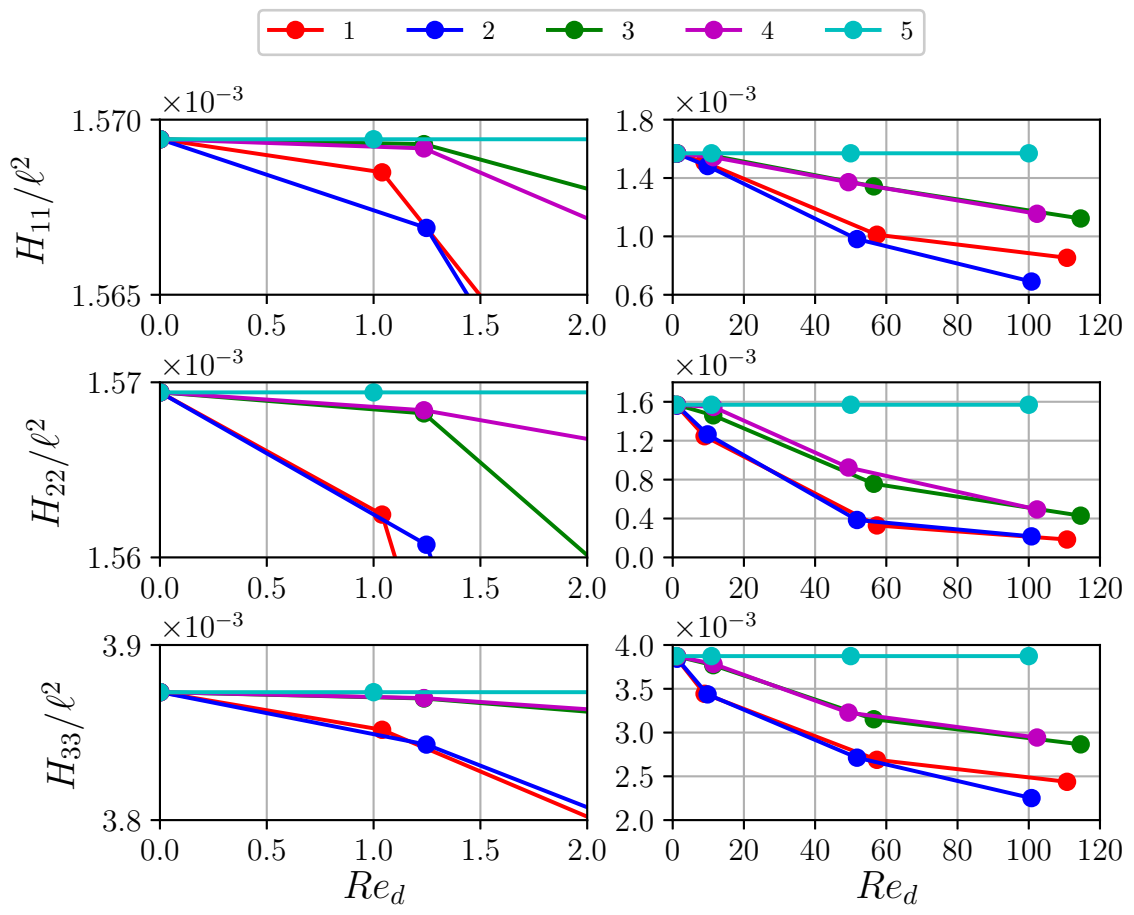


Figure 4.11: Same as figure 4.10 with porosity $\varepsilon = 0.6$.

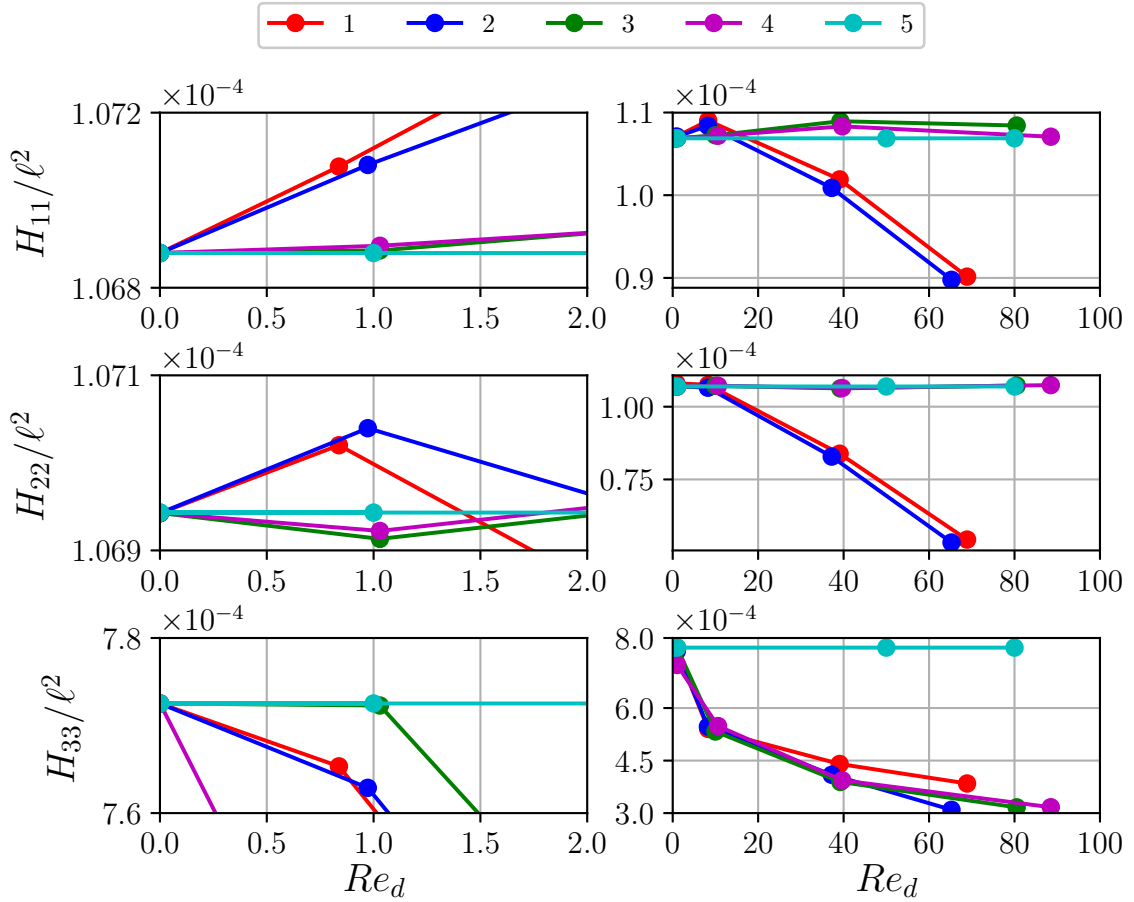


Figure 4.12: Same as figure 4.10 with porosity $\varepsilon = 0.4$.

In the left column of each figure we focus on the low- Re_d regime ($0 < Re_d < 2$), while in the right column the effect of inertia can be assessed. As expected, when Re_d is small the apparent permeability is quasi-Reynolds-number-independent (and can be approximated well by the true permeability). As the Reynolds number increases above a few units, inertial effects grow in importance yielding typically a monotonic decrease of all components of \mathbf{H} , aside from case indexed 5 ($\phi = 90^\circ$) for which the flow remains aligned with the cylinder's axis. In case 5 the microscopic flow solution is invariant with x_3 and does not change with Re_d in the range considered, so that \mathbf{H} is a constant tensor.

When the porosity is large all components show a similar behaviour irrespective of the forcing angle (except, clearly, case 5). Differences start appearing at $\varepsilon = 0.6$; the two cases with $\phi = 0^\circ$ (index 1 and 2) behave similarly, and so do the two cases indexed 3 and 4 (with $\phi = 45^\circ$). This seems to suggest a weaker effect of θ on the permeability components.

For even smaller porosity ($\varepsilon = 0.4$), the blockage which the inclusions cause to the flow produces the unexpected behaviour displayed in figure 4.12. When the flow is purely two-dimensional (cases 1 and 2), variations in the Reynolds number affect \mathbf{H} significantly; when a pressure gradient along x_3 is present the strong packing of the fibers constrain the fluid to flow prevalently along the fibers' axis, and the apparent permeability is almost Re_d -independent. When assessing variations in H_{jj} for this case, attention should also be paid to the fact that the permeability is now at least one order of magnitude smaller than in the previous cases so that variations of the diagonal components shown in figure 4.12 are tiny in absolute terms. This is related to the fact that the inverse of the permeability plays the role of a drag coefficient in the macroscopic expression of the force (cf. equation (??)). In other words, materials with higher porosity (larger space between solid inclusions) offer lower resistance to the motion of the fluid.

Applying the intrinsic average operator to the non-diagonal component of the tensor \mathbf{M} results in terms that are negligible with respect to their diagonal counterparts, and these results are true for all the parameters considered. This means that there is a very weak coupling between the principal directions of the fiber. The directional decoupling and the diagonal property of the apparent permeability tensor has also been computationally demonstrated on a completely different REV geometry by Soulaine and Quintard [113]. Conversely, Lasseux et al. [78] have carried out a two-dimensional study with fibers of square cross-section, finding that the off-diagonal terms are non-negligible and only about one order of magnitude smaller than the diagonal components. This result is a consequence of the non-rotationally-invariant geometry considered. The present work and the two articles just cited suggest that the diagonal property of the tensor \mathbf{H} is closely related to the geometry of the porous material, more than to the flow regime.

4.6 A metamodel for \mathbf{H}

The previous sections has shown how the apparent permeability depends on the two Euler angles, the Reynolds number and the porosity. The space of parameters is formidable and the results found so far are not sufficient to treat, for example, cases characterized by multiple inclusions' sizes and orientations in different regions of the domain, or cases involving a poroelastic medium, with temporally and spatially varying porosity, flow direction and local Reynolds number. The complete solution of the closure problem for a single set of parameters takes approximately 4 CPU hours on our two-processor Intel(r) IVYBRIDGE 2.8Ghz, each with 10 cores and 64 GB of RAM, so that a complete parametric study is, to say the least, unpractical. In view of this, the construction of a metamodel capable to provide a full characterisation of the permeability as a function of all parameters is a worthy endeavor. We have tested several surrogate models, before eventually settling on the kriging approach [74] described in the following.

parameter	values			
θ	0°	22.5°	45°	
ϕ	0°	22.5°	45°	67.5°
Re_d	0	10	50	100
ε	0.4	0.6	0.8	

Table 4.3: Sampling parameters.

4.6.1 DACE sampling

The first step to build a metamodel is the collection of relevant samples. The quality of the final metamodel strongly depends on the samples collected and their number and distribution is of primary importance. The apparent permeability tensor, \mathbf{H} , depends on four independent variables; the samples have been generated starting from the set of parameters given in table 4.3.

One of the best options to generate the relevant database would be to use a full factorial design approach in which all the combinations of the four variables from table 4.3 are computed. Because of the large number of computations required, this approach has not been retained. We have resorted to the methodology known as DACE (Design and Analysis of Computer Experiments), a technique to fill in the best possible way the space of the parameters of the problem. The Dakota library [2] has been selected for the purpose and the Monte-Carlo incremental random sampling algorithm [55] has been chosen, in order to make efficient use of the cases already computed. This incremental approach selects in a quasi-random way the new samples to generate, starting from the existing ones. In the end, the set of samples comprises 118 cases.

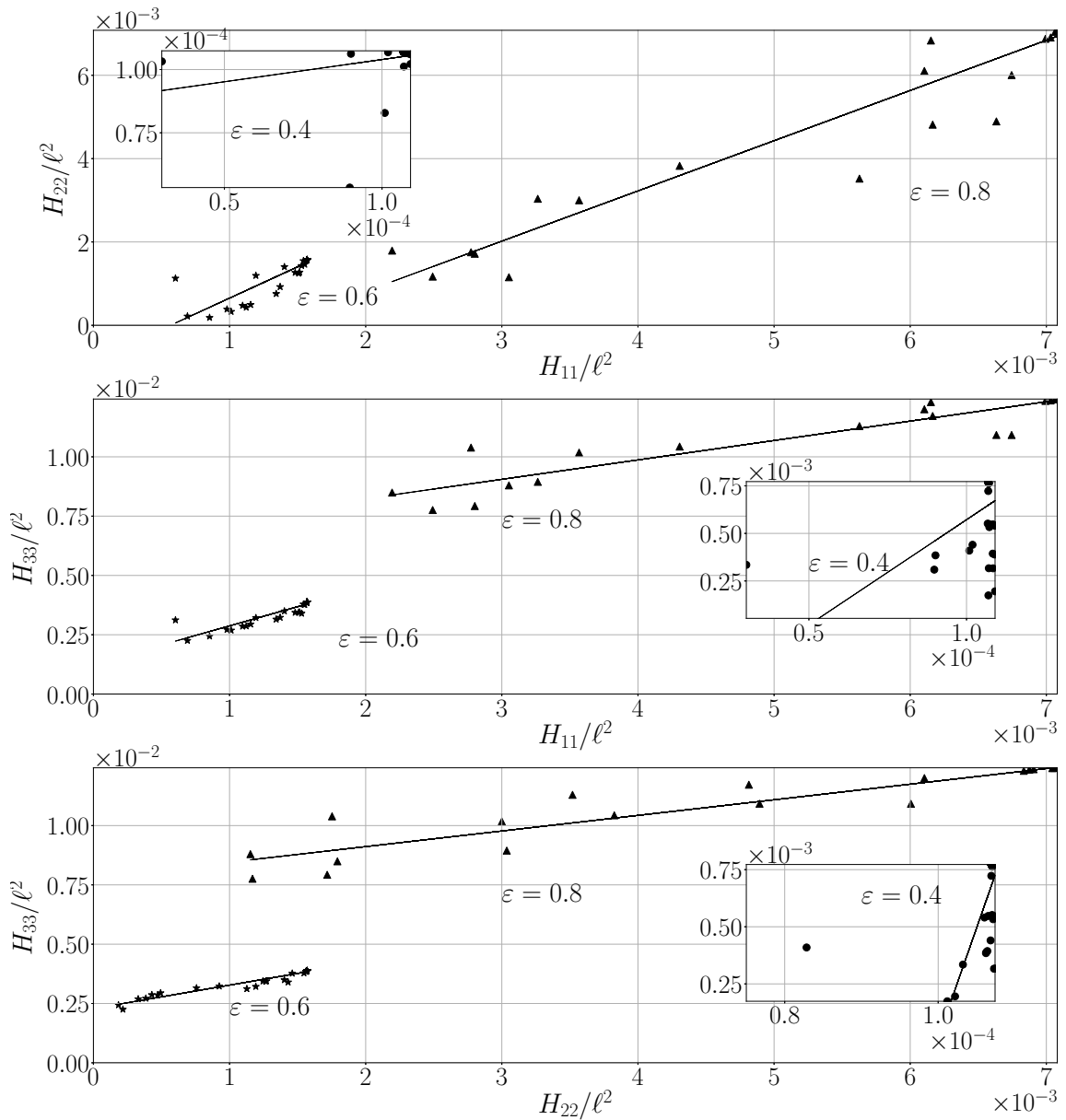


Figure 4.13: Scatter matrix plot for the collected numerical data of the apparent permeability tensor.

In the scatter plot of figure 4.13 the three diagonal components of the permeability tensor are shown as function of one another. The three porosities are separately considered in each of the above plot, and the permeability points are represented with their linear

regression on top. This kind of plot is common in statistical analysis to determine if correlations in the data are present. The permeability components show some correlation with the data points which lie reasonably well on a straight line. This result has a physical implication. Remembering the diagonal dominance of the permeability tensor, we have in the low Re_d limit:

$$\left(\langle u_\beta \rangle^\beta, \langle v_\beta \rangle^\beta, \langle w_\beta \rangle^\beta\right) \sim \left(H_{11} \frac{\partial p}{\partial x_1}, H_{22} \frac{\partial p}{\partial x_2}, H_{33} \frac{\partial p}{\partial x_3}\right). \quad (4.1)$$

It is then possible to compute the angle between the forcing term, ∇p , and the average velocity vector, represented in figure 4.14 for the two-dimensional case, $\phi = 0$. This is achieved by taking the ratio between the first two components of Darcy's equation, calling γ the flow deviation with respect to the mean forcing. We thus have:

$$\tan(\theta + \gamma) = \frac{H_{22}}{H_{11}} \tan \theta. \quad (4.2)$$

If the ratio between the two permeability components is equal to one, the angle γ vanishes. The correlation between H_{11} and H_{22} controls the deviation of the flow in the (x_1, x_2) plane, and the argument can easily be extended to H_{11}/H_{33} and H_{22}/H_{33} for deviation angles in three-dimensions.

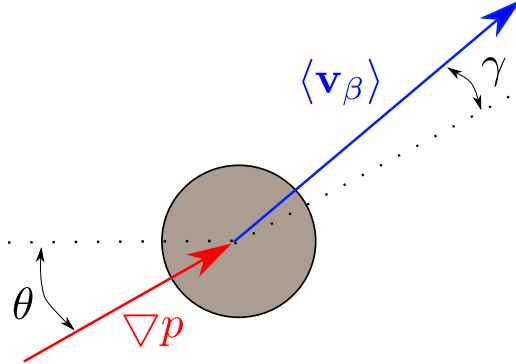


Figure 4.14: Explanatory sketch for the relation between mean pressure gradient and mean velocity field.

Using a linear correlation such as that shown in table 4.4 and figure 4.13, it is observed that in the low porosity case ($\varepsilon = 0.4$) the ratio can become very large indicating a strong deviation of the flow from the forcing direction, because of the strong constraint provided by the inclusions. As the porosity increases, the ratio does not differ much from unity, which means that the deviation remains limited. It is simple to see that the deviation

ε	H_{11}/H_{22}	H_{11}/H_{33}	H_{22}/H_{33}
0.4	1.57	11.06	96.03
0.6	1.50	1.62	0.99
0.8	1.20	0.82	0.66

Table 4.4: Permeability components ratio for three values of the porosity. The permeability ratios here are given by the angular coefficients of the linear correlations displayed in figure 4.13.

angle, for example in the (x_1, x_2) plane, satisfies the approximate relation

$$\tan \gamma = \frac{\left(1 - \frac{H_{11}}{H_{22}}\right) \tan \theta}{\frac{H_{11}}{H_{22}} + \tan^2 \theta},$$

so that for $\frac{H_{11}}{H_{22}}$ equal to, say, 1.5, the largest deviation remains always below 12° for any θ . It should however be kept in mind that trends based on these ratios are valid only as long as Darcy's law and linear correlations are acceptable. Cases exists for which such trends are violated; for example, a flow with $\theta = 45^\circ$ and $\phi = 0^\circ$ has deviation angle γ equal to zero, for whatever porosity. In this case H_{11}/H_{22} is equal to one and such a point is an outlier in the regression plots of figure 4.13.

4.6.2 Kriging interpolation method

The kriging approach is a linear interpolation/extrapolation method that aims to build a predictor field based on a set of observations $(\mathbf{x}_i, y(\mathbf{x}_i))$, for $i = 1, \dots, n$.

The predictor $\hat{f}(\mathbf{x})$ is a sum of a trend function $t(\mathbf{x})$ and a Gaussian process error model $e(\mathbf{x})$:

$$\hat{f}(\mathbf{x}) = t(\mathbf{x}) + e(\mathbf{x}). \quad (4.3)$$

The aim of the error model is to make adjustments on the trend function so that, for any point of the sampling the predictor is exactly equal to the sample, i.e. $\hat{f}(\mathbf{x}_i) = y(\mathbf{x}_i)$. This property represents one of the main qualities of this approach. In addition, when the model parameters are conveniently set, the trend function and the covariance model can take into account both smooth and steep variations in the data set.

The trend function defined here is based on a second order least-square regression, with the coefficients found from the solution of the associated linear system. The Gaussian process error model has zero-mean and its covariance between two generic data-points, x_i and x_j , is written as

$$\text{Cov}(y(\mathbf{x}_i), y(\mathbf{x}_j)) = \sigma^2 r(\mathbf{x}_i, \mathbf{x}_j).$$

The coefficient σ is an amplitude parameter and $r(x^i, x^j)$ is a correlation function, based on the Matérn covariance model that reads:

$$r(\mathbf{x}_i, \mathbf{x}_j) = \frac{2^{1-\nu}}{\Gamma(\nu)} \left(\frac{\sqrt{2\nu}|\mathbf{x}_i - \mathbf{x}_j|}{|\boldsymbol{\lambda}|} \right)^\nu K_\nu \left(\frac{\sqrt{2\nu}|\mathbf{x}_i - \mathbf{x}_j|}{|\boldsymbol{\lambda}|} \right), \quad (4.4)$$

where $K_\nu(\cdot)$ is a modified Bessel function and $\Gamma(\cdot)$ is the gamma function. The parameters that can be used to tune the metamodel are the amplitude parameter σ , the exponent ν and the scale vector $\boldsymbol{\lambda}$. The kriging metamodel outputs can show different behaviours for different selections of the above three parameters and their setting is thus crucial. The amplitude parameter σ is chosen to be equal to 1; larger value lead to steeper gradients and undesirable local extrema around the data points. The vector $\boldsymbol{\lambda} = (\lambda_\theta, \lambda_\phi, \lambda_{Re_d}, \lambda_\varepsilon)$ is a scaling parameter for the distance $|\mathbf{x}_i - \mathbf{x}_j|$. In this study, through systematic variations of the parameters it is found that the choice $\boldsymbol{\lambda} = (1.2, 1, 1, 1)$ yields acceptable results; in particular, the weight along θ is mildly larger than in the other directions in order to obtain smoother metamodel surfaces in this direction. The exponent ν controls the covariance function and more especially its gradients. When $\nu = 1/2$ the covariance can be approximated by a negative exponential, $\exp(-\alpha x)$ and when ν goes to infinity it behaves as $\exp(-\alpha x^2)$. In the present study, the best (i.e. smoother) results are obtained for ν equal to 1.9. The above parameters have been chosen in order to avoid unphysical or unrealistic behaviour of the apparent permeability such as, for instance, negative values or steep, spurious local maxima/minima. The method above is implemented in OpenTURNS and full details are provided by Baudin et al. [11].

In order to prove the robustness of the metamodel we have performed a procedure called cross-validation. This s

and that the number of points choose for the database are enough

The metamodel provides a scalar function (for each term of the \mathbf{H} tensor) defined in a four-dimensional space. In each of the following figures two parameters are fixed and the response surface is displayed as function of the remaining two, focussing on the H_{11} component. The other diagonal components of the apparent permeability tensor behave in a similar fashion and will not be shown for brevity. All the results of the metamodel are, however, available from the authors upon request.

In figure 4.15 the angle ϕ is fixed to zero, and the isolines display H_{11} as function of the angle θ and of the Reynolds number, Re_d , for three values of porosity. The white square symbols indicate the samples used to build the metamodel. The maximum value of each surface is always found for Re_d equal to zero and H_{11} typically decreases with Re_d , when the porosity is sufficiently large. As seen previously, for a porosity approximately greater or equal to 0.6 the variation of the apparent permeability with the angle θ is weak in this two-dimensional configuration. For the lowest porosity studied (left frame) the permeability has very small values and the isolines display an irregular behaviour; this is a feature common to all plots relative to the smaller value of ε , signaling that it is probably

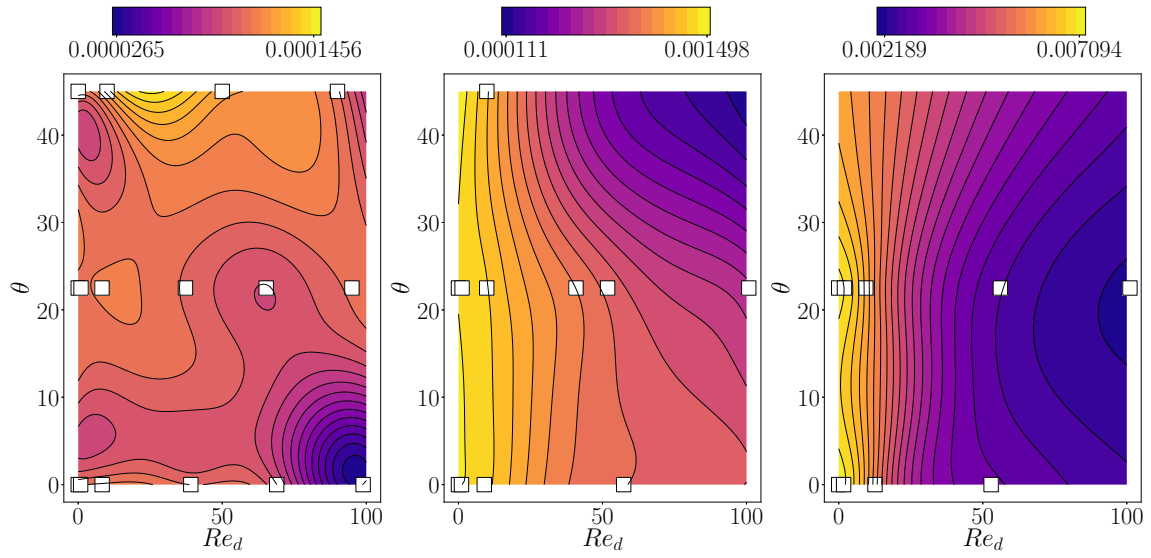


Figure 4.15: Response surfaces of H_{11} with $\phi = 0^\circ$ for porosity $\varepsilon = 0.4, 0.6, 0.8$, from left to right.

necessary, in this specific case, to insert additional sample points in building the response surfaces.

In figure 4.16 the parameter θ is set to 0° and the response surface is displayed in the $Re_d - \phi$ plane. As already indicated, the results confirm that an increase of the Reynolds number is generally associated to a decrease of the first diagonal component of the apparent permeability tensor. However, the H_{11} variations with respect to ϕ are more pronounced than those found with respect to θ and are due to a real three-dimensionalization of the flow. This conclusion remains to be verified in the lower porosity case (left frame) where the variations are very tiny and more irregular.

In figure 4.17 the Reynolds number is set to the inertial range value of 40 and the response surface is displayed in the $\theta - \phi$ plane. For the two highest porosity values, 0.6 and 0.8, the results confirm that H_{11} has a much stronger dependence on ϕ than on θ , suggesting that the real test of permeability models must include three-dimensional effects. As seen earlier, the behaviour of the permeability when the porosity is low (left frame in the figure) is not intuitive, with a significant effect of the angle ϕ and a minor influence of θ . Again this occurs from the constraint provided to the flow by the inclusions, and from the occurrence of a large deviation γ in these cases.

The response surface is shown in the $Re_d - \varepsilon$ plane of figure 4.18 for three sets of $\theta - \phi$ angles. Here a significant effect of the porosity with respect to the Reynolds number is observable. In fact the surface gradient is almost aligned with the porosity direction, i.e. a quasi-Reynolds independence is demonstrated in this plane, and the apparent permeability

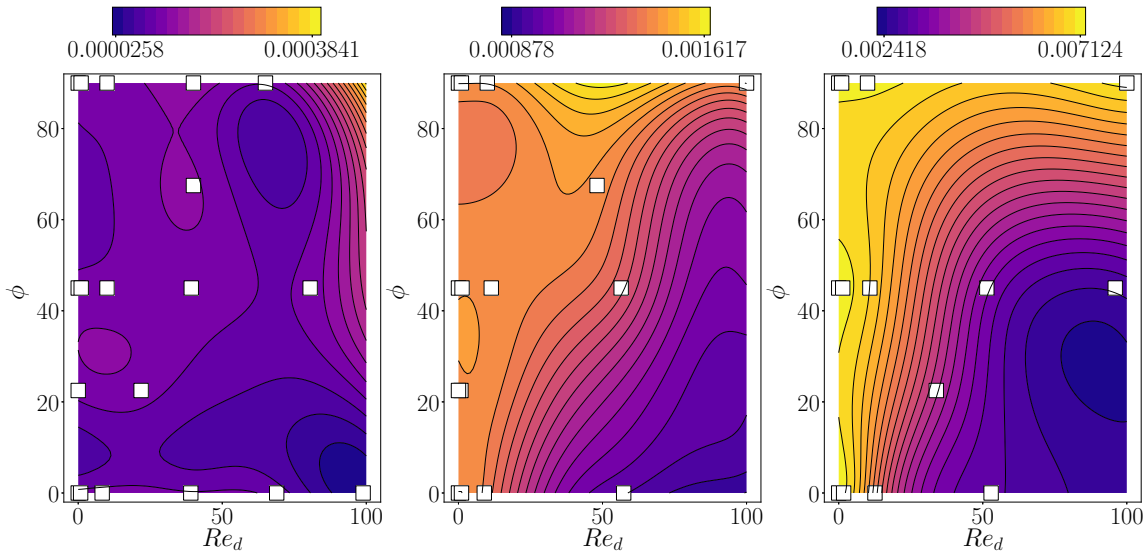


Figure 4.16: Response surfaces of H_{11} with $\theta = 0^\circ$ for porosity $\varepsilon = 0.4, 0.6, 0.8$, from left to right.

can change by one order of magnitude in the range of the analysed porosity.

Some relatively small Reynolds number effects are visible at porosity equal to 0.8, when the wake of the flow has more space to develop in the inertial regime. In the central figure the flow is aligned with the direction of the fibers and, as expected, it shows practically no dependence with respect to the Reynolds number.

The response surface analysis has confirmed the qualitative trends which had been reached earlier on the basis of a few selected flow cases, yielding at the same time much more detailed information on the behaviour of the apparent permeability with the parameters of the problem. The data base which has been built will be used in future work which will focus, via the VANS approach, on configurations for which neither the porosity nor the local Reynolds number are constant in space or time.

4.7 Concluding remarks

The components of the permeability tensor are essential ingredients for any solution of flow through anisotropic porous media. When the flow through the pores resents of significant acceleration effects, the permeability must be modified (it is then called *apparent*) by the presence of a second tensor, the Forchheimer tensor \mathbf{F} , defined by

$$\mathbf{F} = \mathbf{K}\mathbf{H}^{-1} - \mathbf{I}.$$

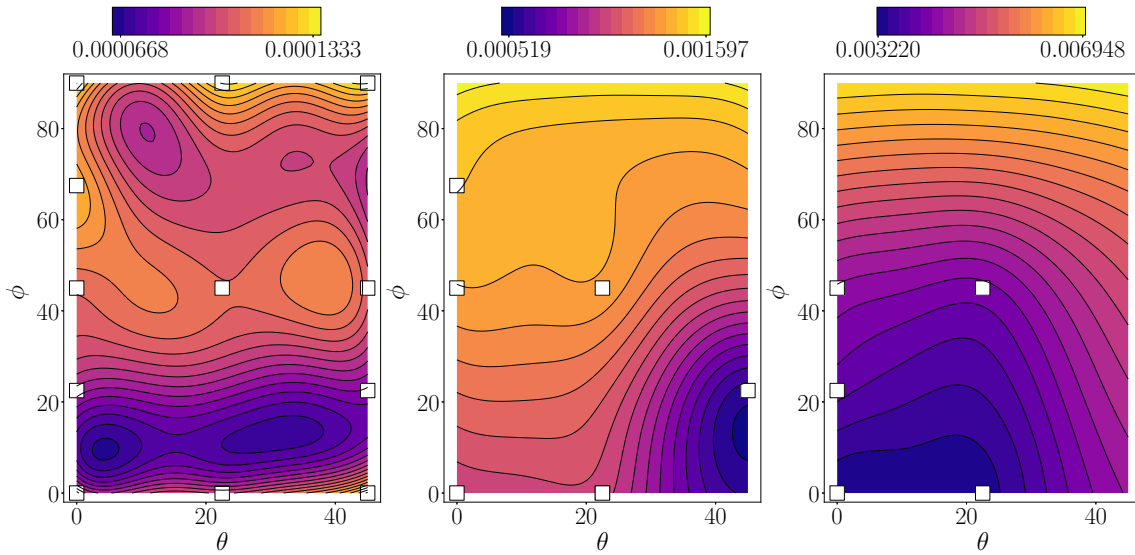


Figure 4.17: Response surfaces of H_{11} with $Re = 40$ for porosity $\varepsilon = 0.4, 0.6, 0.8$, from left to right.

The permeability, \mathbf{K} , and the apparent permeability, \mathbf{H} , can be formally deduced by two closure problems which have been briefly recalled in section 4.2. The real obstacle to the solution of the problem for \mathbf{H} is the need to know the microscopic velocity fields through the pores. We have solved for such fields in a unit cell (the REV), varying the forcing amplitude and direction, treating over one hundred different cases of flows through arrangements of parallel fibers. From this, we have thus been able to solve the linear system (4.1) for all the unknown elements of the intermediate tensor \mathbf{M} , from which, through averaging, we have computed the apparent permeability. Such a tensor is indispensable to evaluate accurately the drag force caused by the presence of the fibers, for a macroscopic solution of the flow on the basis of equations [124] when inertial effects are present.

It has been found that the apparent permeability tensor is strongly diagonally dominant for whatever forcing direction and porosity, provided the local Reynolds number remains below a value approximately equal to 100; this results – which is a direct consequence of the transverse isotropy of the material which has been considered here – can be used to compute \mathbf{H} rapidly, approximating it as a diagonal tensor.

Finally, a metamodel has been used to produce results so as to cover the whole space of parameters, and this has allowed the construction of a complete data base. This data base is now being used in simulations of poroelastic media based on the VANS approach.

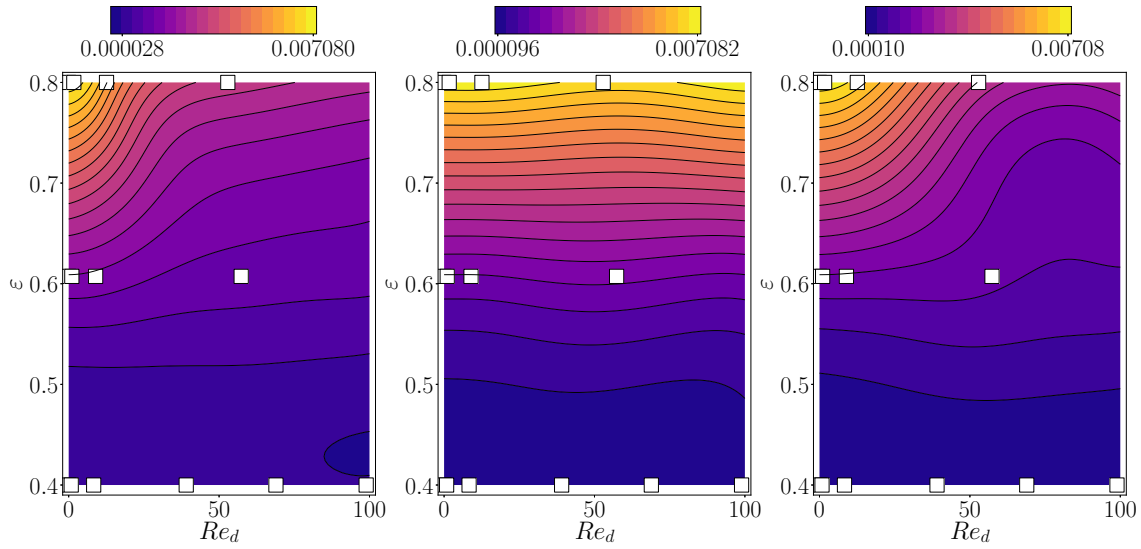


Figure 4.18: Response surface of H_{11} ; in the left frame $\phi = \theta = 0$, in the centre frame $\phi = 90^\circ$, $\theta = 0$ and on the right $\phi = 45^\circ$, $\theta = 22.5^\circ$.

Bibliography

- [1] JD Ackerman and A Okubo. Reduced mixing in a marine macrophyte canopy. *Functional Ecology*, pages 305–309, 1993.
- [2] B.M. Adams, L.E. Bauman, W.J. Bohnhoff, K.R. Dalbey, M.S. Ebeida, J.P. Eddy, M.S. Eldred, P.D. Hough, K.T. Hu, J.D. Jakeman, J.A. Stephens, L.P. Swiler, D.M. Vigil, , and T.M. Wildey. Dakota, a multilevel parallel object-oriented framework for design optimization, parameter estimation, uncertainty quantification, and sensitivity analysis: Version 6.0 Theory Manual. Technical report, Sandia National Laboratories, SAND2014-4253, 2014.
- [3] Mehrez Agnaou, Didier Lasseux, and Azita Ahmadi. From steady to unsteady laminar flow in model porous structures: an investigation of the first Hopf bifurcation. *Computers & Fluids*, 136:67–82, 2016.
- [4] José Alvarado, Jean Comtet, Emmanuel de Langre, and A. E. Hosoi. Nonlinear flow response of soft hair beds. *Nature Physics*, 13:1014–1019, 2017.
- [5] Philippe Angot, Charles-Henri Bruneau, and Pierre Fabrie. A penalization method to take into account obstacles in incompressible viscous flows. *Numerische Mathematik*, 81(4):497–520, 1999.
- [6] Takashi Asaeda, Takeshi Fujino, and Jagath Manatunge. Morphological adaptations of emergent plants to water flow: a case study with *typha angustifolia*, *zizania latifolia* and *phragmites australis*. *Freshwater Biology*, 50(12):1991–2001, 2005.
- [7] Jean-Louis Auriault and E Sanchez-Palencia. Etude du comportement macroscopique d'un milieu poreux saturé déformable. *Journal de mécanique*, 16(4):575–603, 1977.
- [8] JL Auriault. Effective macroscopic description for heat conduction in periodic composites. *International Journal of Heat and Mass Transfer*, 26(6):861–869, 1983.
- [9] Sylvie Barsu, Delphine Doppler, J John Soundar Jerome, Nicolas Rivière, and Michel Lance. Drag measurements in laterally confined 2d canopies: Reconfiguration and sheltering effect. *Physics of Fluids*, 28(10):107101, 2016.

- [10] Ilenia Battiatto and Simonetta Rubol. Single-parameter model of vegetated aquatic flows. *Water Resources Research*, 50(8):6358–6369, 2014.
- [11] Michaël Baudin, Anne Dutfoy, Bertrand Iooss, and Anne-Laure Popelin. *OpenTURNS: An industrial software for uncertainty quantification in simulation*. Springer International Publishing, Cham, 2016. ISBN 978-3-319-11259-6. doi: 10.1007/978-3-319-11259-6_64-1. URL http://dx.doi.org/10.1007/978-3-319-11259-6_64-1.
- [12] Gordon S Beavers and Daniel D Joseph. Boundary conditions at a naturally permeable wall. *Journal of fluid mechanics*, 30(1):197–207, 1967.
- [13] Gordon S Beavers and Daniel D Joseph. Boundary conditions at a naturally permeable wall. *Journal of fluid mechanics*, 30(01):197–207, 1967.
- [14] DW Bechert, M Bruse, W Hage, and R Meyer. Biological surfaces and their technological application—laboratory and flight experiments on drag reduction and separation control. *AIAA paper*, 1960, 1997.
- [15] DW Bechert, M Bruse, W vd Hage, JG Th Van der Hoeven, and G Hoppe. Experiments on drag-reducing surfaces and their optimization with an adjustable geometry. *Journal of fluid mechanics*, 338:59–87, 1997.
- [16] Stephen E Belcher, Ian N Harman, and John J Finnigan. The wind in the willows: flows in forest canopies in complex terrain. *Annual Review of Fluid Mechanics*, 44: 479–504, 2012.
- [17] S Bhattacharyya and AK Singh. Reduction in drag and vortex shedding frequency through porous sheath around a circular cylinder. *International Journal for Numerical Methods in Fluids*, 65(6):683–698, 2011.
- [18] Bharat Bhushan. *Biomimetics: bioinspired hierarchical-structured surfaces for green science and technology*. Springer, 2016.
- [19] A Boomsma and F Sotiropoulos. Direct numerical simulation of sharkskin denticles in turbulent channel flow. *Physics of Fluids*, 28(3):035106, 2016.
- [20] Alessandro Bottaro, Peter Corbett, and Paolo Luchini. The effect of base flow variation on flow stability. *Journal of Fluid Mechanics*, 476:293–302, 2003.
- [21] WP Breugem, BJ Boersma, and RE Uittenbogaard. The influence of wall permeability on turbulent channel flow. *Journal of Fluid Mechanics*, 562:35–72, 2006.
- [22] W Brevis, M García-Villalba, and Y Niño. Experimental and large eddy simulation study of the flow developed by a sequence of lateral obstacles. *Environmental Fluid Mechanics*, 14(4):873–893, 2014.

- [23] HC Brinkman. A calculation of the viscous force exerted by a flowing fluid on a dense swarm of particles. *Applied Scientific Research*, 1(1):27–34, 1949.
- [24] Charles-Henri Bruneau and Iraj Mortazavi. Passive control of the flow around a square cylinder using porous media. *International Journal for Numerical Methods in Fluids*, 46(4):415–433, 2004.
- [25] Charles-Henri Bruneau and Iraj Mortazavi. Numerical modelling and passive flow control using porous media. *Computers & Fluids*, 37(5):488–498, 2008.
- [26] Charles-Henri Bruneau, Emmanuel Creusé, Delphine Depeyras, Patrick Gilliéron, and Iraj Mortazavi. Coupling active and passive techniques to control the flow past the square back ahmed body. *Computers & Fluids*, 39(10):1875–1892, 2010.
- [27] Dennis M Bushnell, Jerry N Hefner, and Robert L Ash. Effect of compliant wall motion on turbulent boundary layers. *The Physics of Fluids*, 20(10):S31–S48, 1977.
- [28] J-P Caltagirone. Sur l’interaction fluide-milieu poreux; application au calcul des efforts exercés sur un obstacle par un fluide visqueux. *Comptes rendus de l’Académie des sciences. Série II, Mécanique, physique, chimie, astronomie*, 318(5):571–577, 1994.
- [29] Claudio Canuto, M Yousuff Hussaini, Alfio Quarteroni, and Thomas A Zang. Spectral methods in fluid dynamics. Technical report, Springer, 1988.
- [30] Ruben G Carbonell and Stephen Whitaker. Heat and mass transfer in porous media. *Fundamentals of transport phenomena in porous media*, 82:121–198, 1984.
- [31] P. C. Carman. Fluid Flow Through Granular Beds. *Transactions - Institution of Chemical Engineers*, 15:150–166, 1937.
- [32] Peter W Carpenter. Status of transition delay using compliant walls. *Viscous drag reduction in boundary layers*, 123:79–113, 1990.
- [33] Rao Chen, Ikeda Teruaki, Nakata Toshiyuki, and Liu Hao. Owl-inspired leading-edge serrations play a crucial role in aerodynamic force production and sound suppression. *Bioinspiration & Biomimetics*, 12(4):046008, 2017.
- [34] Haecheon Choi, Parviz Moin, and John Kim. Direct numerical simulation of turbulent flow over ripples. *Journal of fluid mechanics*, 255:503–539, 1993.
- [35] William O Criminale, Thomas Luther Jackson, and Ronald Douglas Joslin. *Theory and computation of hydrodynamic stability*. Cambridge University Press, 2003.
- [36] Henry Darcy. *Les fontaines publiques de la ville de Dijon*. Victor Dalmont, 1856.

- [37] Yohan Davit, Christopher G Bell, Helen M Byrne, Lloyd AC Chapman, Laura S Kimpton, Georgina E Lang, Katherine HL Leonard, James M Oliver, Natalie C Pearson, Rebecca J Shipley, et al. Homogenization via formal multiscale asymptotics and volume averaging: How do the two techniques compare? *Advances in Water Resources*, 62:178–206, 2013.
- [38] Emmanuel De Langre. Effects of wind on plants. *Annu. Rev. Fluid Mech.*, 40:141–168, 2008.
- [39] Brian Dean and Bharat Bhushan. Shark-skin surfaces for fluid-drag reduction in turbulent flow: a review. *Philosophical Transactions of the Royal Society of London A: Mathematical, Physical and Engineering Sciences*, 368(1929):4775–4806, 2010.
- [40] S Dupont, F Gosselin, Charlotte Py, Emmanuel De Langre, Pascal Hemon, and Yves Brunet. Modelling waving crops using large-eddy simulation: comparison with experiments and a linear stability analysis. *Journal of Fluid Mechanics*, 652:5–44, 2010.
- [41] James E Eckman. The role of hydrodynamics in recruitment, growth, and survival of argopecten irradians (l.) and anomia simplex (d'orbigny) within eelgrass meadows. *Journal of Experimental Marine Biology and Ecology*, 106(2):165–191, 1987.
- [42] DA Edwards, M Shapiro, P Bar-Yoseph, and M Shapira. The influence of Reynolds number upon the apparent permeability of spatially periodic arrays of cylinders. *Physics of Fluids A: Fluid Dynamics*, 2(1):45–55, 1990.
- [43] Sabri Ergun and Ao Ao Orning. Fluid flow through randomly packed columns and fluidized beds. *Industrial & Engineering Chemistry*, 41(6):1179–1184, 1949.
- [44] Julien Favier, Antoine Dauptain, Davide Basso, and Alessandro Bottaro. Passive separation control using a self-adaptive hairy coating. *Journal of Fluid Mechanics*, 627:451–483, 2009.
- [45] Julien Favier, Cuicui Li, Laura Kamps, Alistair Revell, Joseph O'Connor, and Christoph Brücker. The pelskin project—part i: fluid–structure interaction for a row of flexible flaps: a reference study in oscillating channel flow. *Meccanica*, 52(8):1767–1780, 2017.
- [46] John Finnigan. Turbulence in plant canopies. *Annual review of fluid mechanics*, 32(1):519–571, 2000.
- [47] PH Forchheimer. Wasserbewegung durch boden. *Zeitz. Ver. Duetch Ing.*, 45:1782–1788, 1901.

- [48] Maria Cristina Gambi, Arthur RM Nowell, and Peter A Jumars. Flume observations on flow dynamics in *zostera marina* (eelgrass) beds. *Marine ecology progress series*, pages 159–169, 1990.
- [49] Ricardo García-Mayoral and Javier Jiménez. Drag reduction by riblets. *Philosophical Transactions of the Royal Society of London A: Mathematical, Physical and Engineering Sciences*, 369(1940):1412–1427, 2011.
- [50] Ricardo García-Mayoral and Javier Jiménez. Hydrodynamic stability and breakdown of the viscous regime over riblets. *Journal of Fluid Mechanics*, 678:317–347, 2011.
- [51] M Ghisalberti and HM Nepf. The limited growth of vegetated shear layers. *Water Resources Research*, 40(7), 2004.
- [52] Marco Ghisalberti. Obstructed shear flows: similarities across systems and scales. *Journal of Fluid Mechanics*, 641:51–61, 2009.
- [53] Marco Ghisalberti and Heidi Nepf. Mass transport in vegetated shear flows. *Environmental fluid mechanics*, 5(6):527–551, 2005.
- [54] Marco Ghisalberti and Heidi M Nepf. Mixing layers and coherent structures in vegetated aquatic flows. *Journal of Geophysical Research: Oceans*, 107(C2), 2002.
- [55] Anthony A Giunta, Steven F Wojtkiewicz, and Michael S Eldred. Overview of modern design of experiments methods for computational simulations. In *Proceedings of the 41st AIAA aerospace sciences meeting and exhibit, AIAA-2003-0649*, 2003.
- [56] giuseppe ... sfera 3d porosa. *JFM*, 2017.
- [57] G. Gomez-de Segura, A. Sharma, and R. Garcia-Mayoral. Turbulent drag reduction by anisotropic permeable coatings. In *10th International Symposium on Turbulence and Shear Flow Phenomena*, 2017.
- [58] F Gosselin and Emmanuel De Langre. Destabilising effects of plant flexibility in air and aquatic vegetation canopy flows. *European Journal of Mechanics-B/Fluids*, 28(2):271–282, 2009.
- [59] Frédéric P Gosselin and Emmanuel De Langre. Drag reduction by reconfiguration of a poroelastic system. *Journal of Fluids and Structures*, 27(7):1111–1123, 2011.
- [60] William G Gray. A derivation of the equations for multi-phase transport. *Chemical Engineering Science*, 30(2):229–233, 1975.
- [61] Luca Grizzetti, Maurizio Quadrio, and Luca Cortelezzi. Studio sperimentale della scia di un corpo tozzo in presenza di inserti di materiale poroso. Master’s thesis, Politecnico di Milano: Dipartimento Ingegneria Aerospaziale, 2015.

- [62] Raymond E Grizzle, Frederick T Short, Carter R Newell, Heidi Hoven, and Linda Kindblom. Hydrodynamically induced synchronous waving of seagrasses:‘monami’and its possible effects on larval mussel settlement. *Journal of Experimental Marine Biology and Ecology*, 206(1-2):165–177, 1996.
- [63] AM Hamed, MJ Sadowski, HM Nepf, and LP Chamorro. Impact of height heterogeneity on canopy turbulence. *Journal of Fluid Mechanics*, 813:1176–1196, 2017.
- [64] AF Heenan and JF Morrison. Passive control of pressure fluctuations generated by separated flow. *AIAA journal*, 36(6):1014–1022, 1998.
- [65] M Yousuff Hussaini and Thomas A Zang. Spectral methods in fluid dynamics. *Annual review of fluid mechanics*, 19(1):339–367, 1987.
- [66] Jeanette Hussong, Wim-Paul Breugem, and Jerry Westerweel. A continuum model for flow induced by metachronal coordination between beating cilia. *Journal of Fluid Mechanics*, 684:137–162, 2011.
- [67] Syunsuke Ikeda and Minoru Kanazawa. Three-dimensional organized vortices above flexible water plants. *Journal of Hydraulic Engineering*, 122(11):634–640, 1996.
- [68] E Inoue. Studies of the phenomena of waving plants (“honami”) caused by wind. *Journal of Agricultural Meteorology*, 11(3):87–90, 1955.
- [69] Motoyuki Itoh, Shinji Tamano, Ryo Iguchi, Kazuhiko Yokota, Norio Akino, Ryutaro Hino, and Shinji Kubo. Turbulent drag reduction by the seal fur surface. *Physics of Fluids*, 18(6):065102, 2006.
- [70] Justin W Jaworski and N Peake. Aerodynamic noise from a poroelastic edge with implications for the silent flight of owls. *Journal of Fluid Mechanics*, 723:456–479, 2013.
- [71] Javier Jimenez, Markus Uhlmann, Alfredo Pinelli, and Genta Kawahara. Turbulent shear flow over active and passive porous surfaces. *Journal of Fluid Mechanics*, 442: 89–117, 2001.
- [72] Matthew P Juniper, Ardeshir Hanifi, and Vassilios Theofilis. Modal stability theorylecture notes from the flow-nordita summer school on advanced instability methods for complex flows, stockholm, sweden, 2013. *Applied Mechanics Reviews*, 66(2): 024804, 2014.
- [73] Katharina Klausmann and Bodo Ruck. Drag reduction of circular cylinders by porous coating on the leeward side. *Journal of Fluid Mechanics*, 813:382–411, 2017.

- [74] Jack P.C. Kleijnen. Regression and kriging metamodels with their experimental designs in simulation: A review. *European Journal of Operational Research*, 256(1): 1 – 16, 2017. ISSN 0377-2217. doi: <https://doi.org/10.1016/j.ejor.2016.06.041>.
- [75] J Kozeny. Über grundwasserbewegung. *Wasserbau und Wasserwirtschaft*, 22(5): 67–70, 1927.
- [76] Uģis Lācis, Giuseppe Antonio Zampogna, and Shervin Bagheri. A computational continuum model of poroelastic beds. In *Proc. R. Soc. A*, volume 473, page 20160932. The Royal Society, 2017.
- [77] Amy Lang, Michael T Bradshaw, Jonathon A Smith, Jennifer N Wheelus, Philip Motta, Maria Habegger, and Robert E Hueter. Movable shark scales act as a passive dynamic micro-roughness to control flow separation. *Bioinspiration & Biomimetics*, 9:036017, 07 2014.
- [78] Didier Lasseux, A. Arani Abbasian, and A. Ahmadi. On the stationary macroscopic inertial effects for one phase flow in ordered and disordered porous media. *Physics of Fluids (1994-present)*, 23(7):073103, 2011.
- [79] Michael Le Bars and M Grae Worster. Interfacial conditions between a pure fluid and a porous medium: implications for binary alloy solidification. *Journal of Fluid Mechanics*, 550:149–173, 2006.
- [80] Geoffrey M Lilley. A study of the silent flight of the owl. *AIAA paper*, 2340(1998): 1–6, 1998.
- [81] Paolo Luchini, Fernando Manzo, and Amilcare Pozzi. Resistance of a grooved surface to parallel flow and cross-flow. *Journal of fluid mechanics*, 228:87–109, 1991.
- [82] Nicola Luminari, Christophe Airiau, and Alessandro Bottaro. Drag-model sensitivity of kelvin-helmholtz waves in canopy flows. *Physics of Fluids*, 28(12):124103, 2016.
- [83] Timothy I Marjoribanks, Richard J Hardy, Stuart N Lane, and Daniel R Parsons. Does the canopy mixing layer model apply to highly flexible aquatic vegetation? insights from numerical modelling. *Environmental Fluid Mechanics*, 17(2):277–301, 2017.
- [84] Samuel Martin and Bharat Bhushan. Discovery of ripples in a bird beak (ryncrops) for low fluid drag. *Philosophical Transactions of the Royal Society of London A: Mathematical, Physical and Engineering Sciences*, 374(2073), 2016. ISSN 1364-503X. doi: 10.1098/rsta.2016.0134.
- [85] Maria Maza, Javier L Lara, and Inigo J Losada. A coupled model of submerged vegetation under oscillatory flow using navier–stokes equations. *Coastal Engineering*, 80:16–34, 2013.

- [86] Maria Maza, Javier L Lara, and Inigo J Losada. Tsunami wave interaction with mangrove forests: A 3-d numerical approach. *Coastal Engineering*, 98:33–54, 2015.
- [87] Doug McLean. *Understanding aerodynamics: arguing from the real physics*. John Wiley & Sons, 2012.
- [88] CC Mei and J-L Auriault. The effect of weak inertia on flow through a porous medium. *Journal of Fluid Mechanics*, 222:647–663, 1991.
- [89] Chiang C Mei and Bogdan Vernescu. *Homogenization methods for multiscale mechanics*. World scientific, 2010.
- [90] Andro Mikelic and Willi Jäger. On the interface boundary condition of beavers, joseph, and saffman. *SIAM Journal on Applied Mathematics*, 60(4):1111–1127, 2000.
- [91] Chloé Mimeau, Iraj Mortazavi, and G-H Cottet. Passive control of the flow around a hemisphere using porous media. *European Journal of Mechanics-B/Fluids*, 65: 213–226, 2017.
- [92] Philip Motta, Maria Habegger, Amy Lang, Robert Hueter, and Jessica Davis. Scale morphology and flexibility in the shortfin mako isurus oxyrinchus and the blacktip shark carcharhinus limbatus. *Journal of morphology*, 273, 10 2012.
- [93] Hiroshi Naito and Koji Fukagata. Numerical simulation of flow around a circular cylinder having porous surface. *Physics of Fluids*, 24(11):117102, 2012.
- [94] Heidi M Nepf. Flow and transport in regions with aquatic vegetation. *Annual Review of Fluid Mechanics*, 44:123–142, 2012.
- [95] J Alberto Ochoa-Tapia, Francisco José Valdés-Parada, Benoît Goyeau, and Didier Lasseux. Fluid motion in the fluid/porous medium inter-region. *Revista Mexicana de Ingeniería Química*, 16(3):923–938, 2017.
- [96] Johannes Oeffner and George V. Lauder. The hydrodynamic function of shark skin and two biomimetic applications. *Journal of Experimental Biology*, 215(5):785–795, 2012. ISSN 0022-0949. doi: 10.1242/jeb.063040.
- [97] S Patil and VP Singh. Characteristics of monami wave in submerged vegetated flow. *Journal of Hydrologic Engineering*, 15(3):171–181, 2010.
- [98] M. Pauthenet, Y. Davit, M. Quintard, and A Bottaro. Topological scaling for inertial transition in porous media. *submitted*, 2017.
- [99] Alfredo Pinelli, Mohammad Omidyeganeh, Christoph Brücker, Alistair Revell, Abhishek Sarkar, and Edoardo Alinovi. The pelskin project: part iv—control of bluff body wakes using hairy filaments. *Meccanica*, 52(7):1503–1514, 2017.

- [100] Charlotte Py, Emmanuel De Langre, and Bruno Moulia. The mixing layer instability of wind over a flexible crop canopy. *Comptes Rendus Mécanique*, 332(8):613–618, 2004.
- [101] Charlotte Py, Emmanuel De Langre, and Bruno Moulia. A frequency lock-in mechanism in the interaction between wind and crop canopies. *Journal of Fluid Mechanics*, 568:425–449, 2006.
- [102] KR Rajagopal. On a hierarchy of approximate models for flows of incompressible fluids through porous solids. *Mathematical Models and Methods in Applied Sciences*, 17(02):215–252, 2007.
- [103] M_R Raupach, JJ Finnigan, and Y Brunet. Coherent eddies and turbulence in vegetation canopies: the mixing-layer analogy. In *Boundary-Layer Meteorology 25th Anniversary Volume, 1970–1995*, pages 351–382. Springer, 1996.
- [104] Alistair Revell, Joseph O'Connor, Abhishek Sarkar, Cuicui Li, Julien Favier, Laura Kamps, and Christoph Brücker. The pelskin project: part ii—investigating the physical coupling between flexible filaments in an oscillating flow. *Meccanica*, 52(8):1781–1795, 2017.
- [105] P.J. Roache. *Verification and validation in computational science and engineering*. Hermosa Press, Albuquerque, NM., 1998.
- [106] Marco E Rosti, Laura Kamps, Christoph Bruecker, Mohammad Omidyeganeh, and Alfredo Pinelli. The pelskin project-part v: towards the control of the flow around aerofoils at high angle of attack using a self-activated deployable flap. *Meccanica*, 52(8):1811–1824, 2017.
- [107] Peter J Schmid and Dan S Henningson. *Stability and transition in shear flows*, volume 142. Springer Science & Business Media, 2012.
- [108] Antonio Segalini, Jens HM Fransson, and P Henrik Alfredsson. An experimental analysis of canopy flows. In *Journal of Physics: Conference Series*, volume 318, page 072018. IOP Publishing, 2011.
- [109] Antonio Segalini, Jens HM Fransson, and P Henrik Alfredsson. Scaling laws in canopy flows: a wind-tunnel analysis. *Boundary-layer meteorology*, 148(2):269–283, 2013.
- [110] Ravi Singh, MM Bandi, Amala Mahadevan, and Shreyas Mandre. Linear stability analysis for monami in a submerged seagrass bed. *Journal of Fluid Mechanics*, 786, 2016.
- [111] E Skjetne and JL Auriault. New insights on steady, non-linear flow in porous media. *European Journal of Mechanics-B/Fluids*, 18(1):131–145, 1999.

- [112] Nathan Slegers, Michael Heilman, Jacob Cranford, Amy Lang, John Yoder, and Maria Laura Habegger. Beneficial aerodynamic effect of wing scales on the climbing flight of butterflies. *Bioinspiration & biomimetics*, 12(1):016013, 2017.
- [113] Cyprien Soulaine and Michel Quintard. On the use of a Darcy–Forchheimer like model for a macro-scale description of turbulence in porous media and its application to structured packings. *International Journal of Heat and Mass Transfer*, 74:88–100, 2014.
- [114] RB Srygley and ALR Thomas. Unconventional lift-generating mechanisms in free-flying butterflies. *Nature*, 420(6916):660, 2002.
- [115] Emmanuel Stratakis, Vassilia Zorba, Marios Barberoglou, Emmanuel Spanakis, Sophia Rhizopoulou, Panagiotis Tzanetakis, Spiros Anastasiadis, and Costas Fotakis. Laser structuring of water-repellent biomimetic surfaces. *SPIE Newsroom*, 10(2.1200901):1441, 2009.
- [116] Nils Tilton and Luca Cortelezzi. Linear stability analysis of pressure-driven flows in channels with porous walls. *Journal of Fluid Mechanics*, 604:411–445, 2008.
- [117] Cameron Tropea and Horst Bleckmann. *Nature-Inspired Fluid Mechanics: Results of the DFG Priority Programme 1207 "Nature-inspired Fluid Mechanics" 2006-2012*, volume 119. Springer Science & Business Media, 2012.
- [118] Divya Venkataraman and Alessandro Bottaro. Numerical modeling of flow control on a symmetric aerofoil via a porous, compliant coating. *Physics of Fluids*, 24(9):093601, 2012.
- [119] H. G. Weller, G. Tabor, H. Jasak, and C. Fureby. A tensorial approach to computational continuum mechanics using object-oriented techniques. *Computers in Physics*, 12(6):620–631, 1998.
- [120] Stephen Whitaker. The transport equations for multi-phase systems. *Chemical Engineering Science*, 28(1):139–147, 1973.
- [121] Stephen Whitaker. Flow in porous media i: A theoretical derivation of darcy's law. *Transport in porous media*, 1(1):3–25, 1986.
- [122] Stephen Whitaker. Flow in porous media iii: deformable media. *Transport in Porous Media*, 1(2):127–154, 1986.
- [123] Stephen Whitaker. The Forchheimer equation: a theoretical development. *Transport in Porous Media*, 25(1):27–61, 1996.
- [124] Stephen Whitaker. *The Method of Volume Averaging*, volume 13. Springer Science & Business Media, 2013.

- [125] K Yazdchi, S Srivastava, and S Luding. Microstructural effects on the permeability of periodic fibrous porous media. *International Journal of Multiphase Flow*, 37(8):956–966, 2011.
- [126] G. A. Zampogna and A. Bottaro. Fluid flow over and through a regular bundle of rigid fibres. *Journal of Fluid Mechanics*, 792:5–35, 2016. doi: 10.1017/jfm.2016.66.
- [127] Giuseppe A Zampogna and Alessandro Bottaro. Fluid flow over and through a regular bundle of rigid fibres. *Journal of Fluid Mechanics*, 792:5–35, 2016.
- [128] Giuseppe A Zampogna and Alessandro Bottaro. private communication. *The values of \mathcal{K}_{11} and \mathcal{K}_{22} arise from the solution of a local, microscopic problem which accounts for inertia through the porous medium [127]. It is not unexpected that \mathcal{K}_{11} approaches \mathcal{K}_{22} as we leave the Stokes regime.*, 2016.
- [129] Giuseppe A Zampogna and Alessandro Bottaro. The pelskin project—part iii: a homogenized model of flows over and through dense poroelastic media. *Meccanica*, 52(8):1797–1808, 2017.
- [130] Giuseppe A Zampogna and Alessandro Bottaro. The pelskin project—part iii: a homogenized model of flows over and through dense poroelastic media. *Meccanica*, 52(8):1797–1808, 2017.
- [131] Giuseppe A Zampogna, Franck Pluvineage, Azeddine Kourta, and Alessandro Bottaro. Instability of canopy flows. *Water Resources Research*, 52(7):5421–5432, 2016.
- [132] Xueyan Zhang and Heidi M Nepf. Exchange flow between open water and floating vegetation. *Environmental fluid mechanics*, 11(5):531–546, 2011.